

Multi-Strange and Charmed Antihyperon- Hyperon Physics for PANDA

Erik Thomé



UPPSALA
UNIVERSITET

Dissertation presented at Uppsala University to be publicly examined in Högssalen, Ångström-laboratoriet, Lägerhyddsvägen 1, Uppsala, Friday, November 23, 2012 at 10:15 for the degree of Doctor of Philosophy. The examination will be conducted in English

Abstract

Thomé, E. 2012. Multi-Strange and Charmed Antihyperon-Hyperon Physics for PANDA. Acta Universitatis Upsaliensis. Uppsala Dissertations from the Faculty of Science and Technology 101. 151 pp. Uppsala. ISBN 978-91-554-8497-2.

The thesis concerns the prospects of studying multi-strange and charmed antihyperon-hyperon physics and CP violation in hyperon decays in the upcoming PANDA experiment.

The angular distribution dependence on polarisation parameters in the decay of the spin 3/2 Omega hyperon was calculated using the density matrix formalism. Expressions for the angular distributions in both the $\Omega \rightarrow \Lambda K$ and the subsequent $\Lambda \rightarrow p\pi$ were obtained.

Simulations were performed for the $\bar{p}p \rightarrow \bar{\Xi}^+\Xi^-$, $\bar{p}p \rightarrow \bar{\Omega}^+\Omega^-$ and $\bar{p}p \rightarrow \bar{\Lambda}_c^-\Lambda_c^+$. The beam momenta were 4, 12 and 12 GeV/c, respectively. Special attention was given to the reconstruction of spin variables. For the $\bar{p}p \rightarrow \bar{\Xi}^+\Xi^-$ reaction PANDA will give tens of events/s, which should be compared to the previously existing data of a handful of events for this reaction. For the other two reactions the event rates will be lower but still reasonably high, considering that this will be the first measurements of these reactions. It was also shown that spin variables can be reconstructed in all three reactions for all production angles of the hyperons.

Simulations concerning the possibility to measure CP violation parameters in hyperon decays were also performed for the reactions $\bar{p}p \rightarrow \bar{\Lambda}\Lambda$ and $\bar{p}p \rightarrow \bar{\Xi}^+\Xi^-$. It was found that false signals from detector asymmetries disappears if no particle identification criterium is used and the analysis is restricted to events where the hyperon decays occur close to the beam axis.

The effect of the magnetic field in the PANDA detector on the measurement of hyperon spin variables was investigated for the case of $\bar{p}p \rightarrow \bar{\Lambda}\Lambda$. The effect was observed to be small for polarisation and negligible for spin correlations.

Keywords: PANDA, FAIR, antiproton, hyperon, strangeness, charm, polarisation, spin correlation, CP violation

Erik Thomé, Uppsala University, Department of Physics and Astronomy, Nuclear Physics, Box 516, SE-751 20 Uppsala, Sweden.

©Erik Thomé 2012

ISSN 1104-2516

ISBN 978-91-554-8497-2

urn:nbn:se:uu:diva-182450 (<http://urn.kb.se/resolve?urn=urn:nbn:se:uu:diva-182450>)

Printed by Elanders Sverige AB, 2012

Till Alva och Lovisa

Contents

1	Introduction	11
1.1	Standard Model of Particle Physics	11
1.2	Quarks and Gluons	13
1.3	Hadrons	14
1.4	Hyperons	16
1.5	Hyperon Physics in Antiproton-Proton Collisions and the PANDA experiment	18
1.6	CP Violation	19
1.7	Thesis Disposition	20
2	PANDA	23
2.1	The FAIR Facility	23
2.2	The PANDA Detector	25
2.2.1	Target Spectrometer	26
2.2.2	Forward Spectrometer	32
2.3	PANDA Physics	34
3	The $\bar{p}p \rightarrow \bar{\Sigma}^0 \Sigma^0$ Reaction	37
3.1	Spin Variables	37
3.1.1	The Density Matrix	37
3.1.2	Hyperon Density Matrices	39
3.1.3	Angular Distributions for Hyperon Decays	44
3.1.4	Spin Variables in the $\bar{p}p \rightarrow \bar{\Sigma}^0 \Sigma^0$ Reaction	50
3.1.5	Hyperon Rest Systems and Symmetry Constraints on Spin Variables	53
3.1.6	Restrictions on Spin Variables from Theoretical Considerations	54
3.2	CP Violation Parameters	56
4	Existing Data and Theoretical Predictions	59
4.1	Prior Knowledge on the $\bar{p}p \rightarrow \bar{\Sigma}^0 \Sigma^0$ Reaction	60
4.2	Hyperon Channels for This Thesis	65
4.2.1	The $\bar{p}p \rightarrow \bar{\Xi}^+ \Xi^-$ Reaction	65
4.2.2	The $\bar{p}p \rightarrow \bar{\Omega}^+ \Omega^-$ Reaction	67
4.2.3	The $\bar{p}p \rightarrow \bar{\Lambda}_c^- \Lambda_c^+$ Reaction	69
4.3	CP Violation	69
5	Analysis Methods	71
5.1	Spin Variables for the Spin 1/2 Hyperons	71
5.2	Polarisation and Asymmetry Parameters of the Ω Hyperon	73

5.3	Methods to Compensate for Angular Dependence of Reconstruction Efficiency	76
5.3.1	Method Using Monte Carlo Based Acceptance Functions	76
5.3.2	Method Without the Use of Monte Carlo Based Acceptance functions	76
5.4	CP violation parameters	80
6	Simulations of Multi-Strange and Charmed $\bar{p}p \rightarrow \bar{Y}Y$ Reactions . . .	85
6.1	The Simulation Framework	85
6.1.1	Digitisation	86
6.1.2	Track Reconstruction	87
6.1.3	Charged Particle Identification	87
6.1.4	Analysis	90
6.1.5	Ongoing Software Development	90
6.2	The $\bar{p}p \rightarrow \bar{\Xi}^+ \Xi^-$ Reaction	92
6.2.1	Data Generation	92
6.2.2	Event Reconstruction	92
6.2.3	Reconstruction Efficiency and Background	93
6.2.4	Reconstruction Efficiency as a Function of the $\bar{\Xi}^+$ Production Angle	93
6.2.5	Reconstruction of Decay Vertices	94
6.2.6	Ξ^- Lifetime Reconstruction	94
6.2.7	Invariant Mass	95
6.2.8	Correction for the Bending of the $\bar{\Xi}^+$ and Ξ^- Trajectories in the Magnetic Field	96
6.2.9	Reconstruction Efficiency as a Function of the $\bar{\Lambda}$ Decay Angle in the $\bar{\Xi}^+$ rest frame	97
6.2.10	Comparison Between the Methods for Calculation of Spin Variables	98
6.3	The $\bar{p}p \rightarrow \bar{\Omega}^+ \Omega^-$ Reaction	104
6.3.1	Data Generation	104
6.3.2	Event Reconstruction	104
6.3.3	Reconstruction Efficiency and Background	105
6.3.4	Reconstruction Efficiency as a Function of the $\bar{\Omega}^+$ Production Angle	106
6.3.5	Reconstruction of Decay Vertices	106
6.3.6	Ω^- Lifetime Reconstruction	107
6.3.7	Invariant Mass	107
6.3.8	Reconstruction of Polarisation and Asymmetry Parameters	108
6.4	The $\bar{p}p \rightarrow \bar{\Lambda}_c^- \Lambda_c^+$ Reaction	111
6.4.1	Data Generation	111
6.4.2	Reconstruction	111
6.4.3	Reconstruction Efficiency and Background	111
6.4.4	Acceptance as a Function of the $\bar{\Lambda}_c^-$ Production Angle	112
6.4.5	Reconstruction of Decay Vertices	113

6.4.6	Invariant Mass	113
6.4.7	Reconstruction of Spin Variables	114
6.4.8	Other Charmed Hyperons	114
6.5	CP Violation in Hyperon Decay	116
6.5.1	General Experimental Considerations	116
6.5.2	Reconstruction of the CP Violation Parameter A for the $\bar{p}p \rightarrow \bar{\Lambda}\Lambda$ Reaction	116
6.5.3	Reconstruction of CP Violation Parameters for the $\bar{p}p \rightarrow$ $\Xi^+\Xi^-$ Reaction	119
7	Precession of the Hyperon Polarisation Vector in the Magnetic Field of the PANDA Detector	123
7.1	Precession of Polarisation Vectors in a Magnetic Field	123
7.2	Effect on the measurement of Λ Polarisation	125
7.3	Effect on the measurement of $\bar{\Lambda}\Lambda$ Spin Correlations	127
7.4	Other Hyperons	130
8	Conclusions and Outlook	133
8.1	Calculations of Decay Angular Distributions for the Spin 3/2 Ω Hyperon	133
8.2	Simulations of Multi-Strange and Charmed $\bar{p}p \rightarrow \bar{Y}Y$ Reactions	134
8.3	Effect of Magnetic Field on Measurement of Hyperon Spin Variables	135
8.4	Outlook	136
9	Svensk sammanfattning	137
10	Acknowledgements	143
11	Bibliography	145

1. Introduction

*Three quarks for Muster Mark!
Sure he hasn't got much of a bark
And sure any he has it's all beside the mark.*

James Joyce "Finnegans Wake"

The topic of this thesis is within the field of hadron physics. A hadron is a composite particle built up by quarks and held together by the strong interaction. The most important aim of hadron physics is to understand how the strong interaction binds the quarks into composite particles. This is the least understood part of the Standard Model of particle physics with many interesting challenges from both theoretical and experimental perspective. This chapter begins with a short overview of the Standard Model and continues by describing more in detail the particles and physics which will be of importance for the rest of the thesis.

1.1 Standard Model of Particle Physics

The question of what the fundamental building blocks of the universe are has a long history through humankind. The current understanding is described by the Standard Model. It was developed in the sixties [1, 2, 3] and completed in the early seventies with the discovery of quarks [4, 5, 6], which had been theoretically predicted for some time [7, 8]. It has since been extremely well tested experimentally. This theory includes all the elementary particles which have been found so far and their interactions via the electromagnetic, the weak and the strong force. Gravity, which is the fourth known force of nature, is not included, but is negligibly small, in principle, for all particle physics calculations. The three interactions of the theory are described as the exchange of spin 1 force mediating gauge bosons. These mediating bosons are the photon for electromagnetism, the W^+ , W^- and Z^0 for the weak force and the eight gluons for the strong force.

From a more theoretical point of view, the Standard Model is a renormalisable quantum field theory. Both the fermions which build up matter and

the bosons which mediate the interactions are described by fields, which, when quantised, gives rise to particles. The interactions between particles enter the theory by demanding that the Lagrangian is gauge invariant under an $U(1) \times SU(2) \times SU(3)$ symmetry. In order for this symmetry to hold, gauge fields corresponding to each of the subgroups have to be included in the Lagrangian. The $U(1) \times SU(2)$ part gives rise to the electroweak theory, where the photon and Z^0 fields are orthogonal combinations of the $U(1)$ and one of the three $SU(2)$ gauge fields and W^- and W^+ are combinations of the other two $SU(2)$ gauge fields. The gluon fields of the strong interaction come from the eight $SU(3)$ gauge fields.

The matter surrounding us is built up by fermions, particles with half-integer spin. The 12 fundamental fermions are divided into two groups: quarks and leptons¹. The difference between the two is that the quarks are strongly interacting particles, while the leptons are not. There are six flavours of quarks (up, down, strange, charm, top, bottom), divided into three electroweak $SU(2)$ doublets

$$\begin{pmatrix} u \\ d \end{pmatrix} \quad \begin{pmatrix} c \\ s \end{pmatrix} \quad \begin{pmatrix} t \\ b \end{pmatrix} \quad (1.1)$$

where the quarks in the upper and lower row have electric charge $+2/3e$ and $-1/3e$, respectively, with e being the charge of the electron. Flavour can only be changed through the weak interaction. Transitions within the same $SU(2)$ doublet are the most probable, even though transitions between the doublets can happen. The probabilities for transitions between different flavours are given by the CKM matrix [9, 10]. The leptons also form three electroweak $SU(2)$ doublets

$$\begin{pmatrix} e \\ \nu_e \end{pmatrix} \quad \begin{pmatrix} \mu \\ \nu_\mu \end{pmatrix} \quad \begin{pmatrix} \tau \\ \nu_\tau \end{pmatrix} \quad (1.2)$$

where the leptons (called electron, muon and tauon) in the upper row have electric charge $-e$ and their corresponding neutrinos in the lower row are uncharged. All 12 particles have been found experimentally, the latest being the discovery of the top quark in 1994 [11]. An $SU(2)$ doublet of quarks together with an $SU(2)$ doublet of leptons is called a generation and there are thus three generations of fundamental particles. The particles of the first generation are much lighter than the particles of the other two. Consequently, the particles of the second and third generation decays to the particles of the first generation, while the particles of the first generation have no lighter generation to decay to. This means that the particles of the first generation are the stable ones which build up the matter of the world around us.

¹For each particle there also exists an antiparticle with the same mass, but opposite charges.

As described until this point, all particles of the theory are massless, which is not the case in nature. The method to give these particles mass in the Standard Model is called the Higgs mechanism [12, 13, 14]. A scalar Higgs field is introduced, with a non-vanishing vacuum expectation value. A local symmetry is spontaneously broken, and some of the massless gauge fields become massive. In this way, the Higgs mechanism explains why the W^+ , W^- and Z^0 bosons are massive, whereas the photon is not. The interaction of particles with the Higgs field gives them their mass.

The particles of interest for this thesis are the strongly interacting quarks and the hadrons they are bound into. This will be discussed in the following sections.

1.2 Quarks and Gluons

Apart from the electromagnetic and weak force, the quarks also, in contrast to the leptons, interacts via the strong force. The charge of the strong interaction comes in three colours, which are called red, blue and green. This should not be confused with colour in everyday life, the name is given since the charges share the property of colour that a combination of them all gives a neutral (white) charge. Due to the naming of its charge after colour, the theory of the strong interaction is called Quantum Chromo Dynamics, abbreviated QCD. A quark carries one of these three colours and an antiquark carries one of the corresponding anticolours. As mentioned earlier, the mediating bosons of the strong interaction are the eight gluons. A major difference from the electromagnetic interaction is that the gluons themselves carry colour charge, whereas the photon, the mediating boson of the electromagnetic interaction, is electrically neutral. This self interaction of the gluons gives rise to a striking feature of the strong interaction called confinement. A qualitative understanding of why the phenomenon arises is outlined in the following. Instead of having field lines spreading in all directions as is the case for the electromagnetic force, the strong force at sufficiently large distances has flux tubes between colour charged particles. This means that the force between two such coloured particles does not decrease with distance. Suppose that you want to separate two colour charged particles which together build up a colour neutral combination. At a certain distance it becomes energetically favourable to create a shielding particle-antiparticle pair instead of moving the original pair further apart. Instead of ending up with a separated colour charged particle, you end up with more colour neutral combinations of them. This is an explanation of why one does not see individual quarks in experiments, instead they are always confined into colour neutral particles called hadrons.

As mentioned above, there are six flavours of quarks. The following relation holds between their masses

$$m_u < m_d \ll m_s \ll m_c < m_b \ll m_t \quad (1.3)$$

All quarks can be bound into hadrons except for the top quark, which is very heavy and therefore decays too quickly to have time to form a bound state.

1.3 Hadrons

The easiest ways to form a colour neutral composite particle of quarks, are either to combine three quarks (or antiquarks) or to combine one quark and one antiquark. In the former case the hadron is called a baryon and in the latter case a meson. All hadrons which have been experimentally confirmed are of these two types, even though a lot of experimental and theoretical activity is going on to find hadrons of a more complex structure. The most common baryons are the proton and the neutron. Their constituent quarks are of the two lightest flavours, uud for the proton and udd for the neutron. Together they build up the atomic nuclei. Consequently, the mass of the observable world around us is almost entirely made up from hadrons. Of this mass only about two percent comes from the mass of the individual quarks, *i.e.* the Higgs mechanism. The rest is generated by the strong interaction itself. It is consequently a very interesting question to study how the quarks are bound into hadrons. Unfortunately, the length scale where this takes place is in a regime where it is very difficult to make QCD calculations. The reason for this is connected to a feature of the strong interaction called asymptotic freedom, which will be discussed in the following.

The coupling constants of all the three interactions, which determine their strengths, depend on the energy scale at which they are measured. This can be understood through the concept of renormalisation. To calculate the cross section of a process in particle physics, a perturbative method using Feynman diagrams is used. In the Feynman diagrams different ways that the process can take place through the exchange of gauge bosons are drawn and rules are given how to calculate their contribution to the cross section (*e.g.* each vertex gives one factor of the coupling constant). The Feynman diagrams are then ordered according to the order of factors of the coupling constants they give rise to, and the largest contribution to the cross section is assumed to be given by the lowest order Feynman diagrams. Due to the fact that particle-antiparticle pairs can be created, higher order Feynman diagrams, with loops of particle-antiparticle pairs attached to the gauge boson lines, are introduced. Since the particles in the loops can take any value of momentum this leads to infinities in the calculations. Renormalisation is a way to remove these infinities by redefining coupling constants, so that they in fact are no longer constants, but dependent on energy scale. A qualitative way to describe this is that the

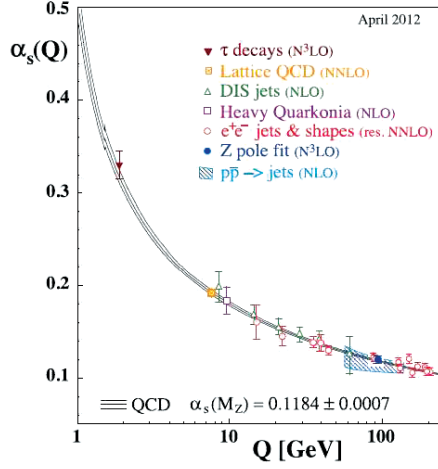


Figure 1.1: The strong coupling constant as a function of the energy scale, Q [15].

effective charge in an interaction is different from the bare charge of a particle. A problem that then arises is that the interaction strength would go to infinity when the distance between charged particles goes to zero. This is hindered by the fact that the charge is shielded by a cloud of particle-antiparticle pairs. The higher the energy scale, the deeper you go into this cloud and the larger effective charge you see. This is the case for the electromagnetic and weak interaction, where the coupling constant increases with energy. For the strong interaction, however, the self-interaction of the gluons gives rise to a new kind of loop consisting of gluons. The result of these loops is an antiscreening effect, causing the strong coupling constant instead to decrease with energy. Figure 1.1 shows experimental and theoretical values of the strong coupling constant at different energy scales. High energy scale can be related to a short length scale through Heisenberg's uncertainty principle.

The consequence of the decreasing coupling constant is that quarks asymptotically seem to behave as free particles at high energies, whereas at lower energy scales they are tightly bound into hadrons. At high energy scales the perturbative method ordered in powers of the strong coupling works, since the value of coupling constant then is relatively low. When the coupling constant becomes too large this is no longer possible and other approaches are needed. For low energy scales, one possibility is to describe the strong interaction by the exchange of mesons. In this way, two different pictures are needed to de-

scribe the strong interaction. For high energies the quarks and gluons are the relevant degrees of freedom, whereas hadronic degrees of freedom are suitable for the low energies. At medium energy scales it is not clear which of the pictures is the more adequate. A suitable process to explore this energy region is the creation of antihyperon hyperon pairs in antiproton-proton collisions.

1.4 Hyperons

Hyperons are baryons where at least one of constituent quarks is not an u or a d quark. For the observed hyperons, most often these quarks are instead s quarks, but they can also be c quarks in which case the hyperon is referred to as a charmed hyperon. In the following hyperons of arbitrary sort will be denoted with Y. Which ground state baryons built up by quarks of the three lightest flavours are allowed is defined by the symmetry of the baryon wavefunction. This wavefunction consists of four parts

$$\Psi = \psi(\text{space})\phi(\text{flavour})\chi(\text{spin})\xi(\text{colour}) \quad (1.4)$$

Remembering that baryons are fermions, we know that the total wave function must be antisymmetric. The colour part of the wave function is always antisymmetric under the exchange of two quarks. Furthermore, for the ground state baryons, the relative angular momentum of the quarks is zero, so that the space part of the wave function is symmetric. The remaining part $\phi(\text{flavour})\chi(\text{spin})$ must therefore be symmetric. Under the assumption that the three lightest quarks are massless, SU(3) flavour symmetry holds. The flavour part of the baryon wave function is then given by a decomposition of three SU(3) multiplets for the three quarks

$$\mathbf{3} \otimes \mathbf{3} \otimes \mathbf{3} = \mathbf{10}_S \oplus \mathbf{8}_{M_S} \oplus \mathbf{8}_{M_A} \oplus \mathbf{1}_A \quad (1.5)$$

which should be combined with the spin part from three SU(2) multiplets

$$\mathbf{2} \otimes \mathbf{2} \otimes \mathbf{2} = \mathbf{4}_S \oplus \mathbf{2}_{M_S} \oplus \mathbf{2}_{M_A} \quad (1.6)$$

The subscripts describe the symmetry properties of the wavefunctions; S/A means symmetric/antisymmetric with respect to the interchange of any two of the quarks, while M_S/M_A means mixed symmetry properties, so that the wave function is symmetric/antisymmetric with respect to the interchange of the first two quarks. There are only two combinations which give symmetric wavefunctions, $(\mathbf{10}, \mathbf{4})$ and $(\mathbf{8}, \mathbf{2})$. Thus, the baryons consisting of the three lightest quarks are predicted to be in a decuplet with $J^P = \frac{3}{2}^+$ and an octet with $J^P = \frac{1}{2}^+$. In figure 1.2, these multiplets are shown using strangeness, s,

and third component of isospin, I_3 , as coordinate axes. These hyperons have all been found in experiments.

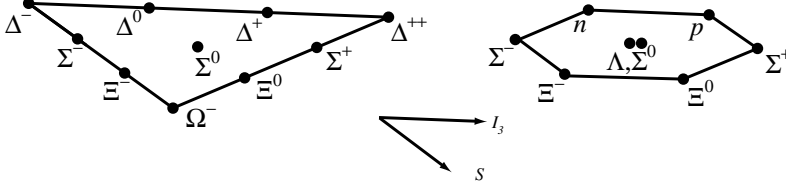


Figure 1.2: The $J^P = \frac{3}{2}^+$ decuplet and the $J^P = \frac{1}{2}^+$ octet of baryons built up by quarks of the three lightest flavours.

If we want to find out which charmed hyperons ought to exist, the reasoning above can be expanded to also include the fourth lightest c quark. The flavour symmetry is in this case described by $SU(4)$, even though it should be remembered that the assumption of massless quarks is not a very good one anymore. In spite of that, the reasoning seems to work quite well. The corresponding decomposition of $SU(4)$ multiplets is

$$4 \otimes 4 \otimes 4 = 20_S \oplus 20_{M_S} \oplus 20_{M_A} \oplus \bar{4}_A \quad (1.7)$$

In this case the symmetric combinations with spin are $(20,4)$ and $(20,2)$. If the 20-plets are decomposed into $SU(3)$ multiplets

$$\begin{aligned} 20_S &= 10 \oplus 6 \oplus 3 \oplus 1 \\ 20_M &= 8 \oplus 6 \oplus \bar{3} \oplus 3 \end{aligned} \quad (1.8)$$

we see that the decuplet and octet, containing baryons from the three lightest quarks, are included in these larger multiplets. In figure 1.3, the two 20-plets are shown with the new dimension of charm, c , as the vertical axis. In this picture the decuplet and octet form the bases of the two 20-plets. Charmed hyperons with one c quark of all sorts have been found experimentally, while no doubly charmed hyperon has been found yet.

The only possibility for hyperons to decay to lighter particles with fewer s and c quarks is through the flavour changing weak interaction. An interesting aspect of the weak interaction is that it does not conserve parity, which means that the daughter particles of the hyperon are not isotropically distributed in the decay. Instead, the daughter baryons are emitted more (or less²) preferably

²If the asymmetry parameter α , which will be introduced later in this thesis, is negative for the hyperon, the daughter baryon will be emitted more preferably in the opposite direction of the hyperon spin direction.

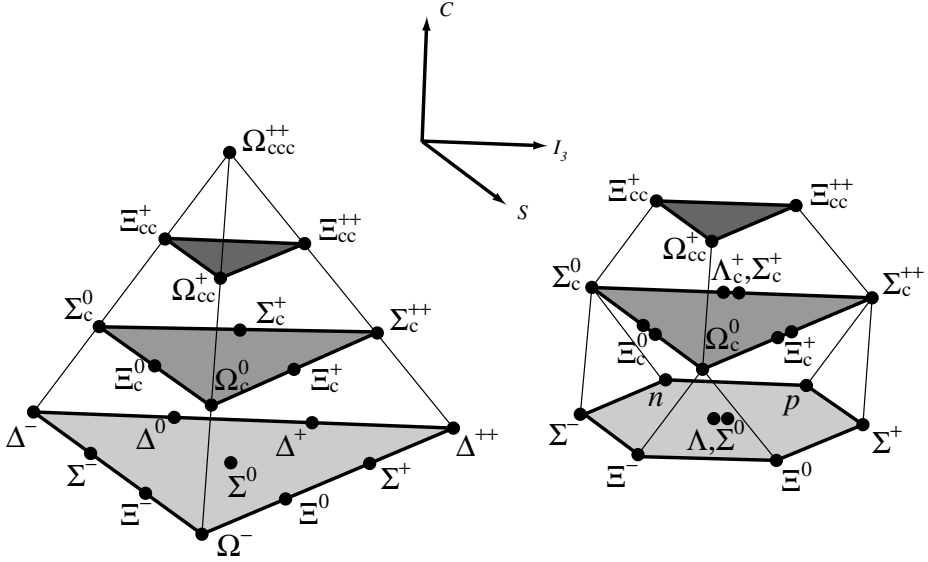


Figure 1.3: The $J^P = \frac{3}{2}^+$ and $J^P = \frac{1}{2}^+$ 20-plets of baryons built up by quarks of the four lightest flavours.

in the hyperon spin direction. By studying the angular distribution in hyperon decays it is therefore possible to extract the hyperon spin variables. While it is often difficult to get information about spin in particle physics experiments, hyperon decays open up a whole area of interesting spin physics.

1.5 Hyperon Physics in Antiproton-Proton Collisions and the PANDA experiment

If protons and antiproton are collided at sufficiently high energy, u or d quark antiquark pairs can be annihilated, while s or c quark antiquark pairs may be created. At the hadron scale, this means that a hyperon-antihyperon pair is created. In the most basic experimental setup where both the initial protons and the antiprotons are unpolarised, the spin variables which can be studied are the individual polarisations of the hyperon/antihyperon and certain correlations between their spins.

Experimental information on spin variables is useful in discriminating between theoretical models describing the $\bar{p}p \rightarrow \bar{Y}Y$ process. These models can be divided into two main groups; the quark gluon picture and the meson exchange picture. Although the models have to describe both the differential

cross sections and the spin variables of the existing data, no clear answer of which picture is the most relevant has been found. New experimental data are therefore needed, in particular on $\bar{p}p \rightarrow \bar{Y}Y$ processes, including heavier hyperons, for which no data exist so far.

The spin variables of the hyperons can often be related to the spin of the individual quarks. As an example, the Λ hyperon can be seen as a spin 0 ud diquark combined with an s quark, so that the spin of the hyperon is carried by the s quark. Consequently, studying spin variables in the $\bar{p}p \rightarrow \bar{\Lambda}\Lambda$ reaction probes the role of spin in the creation of strangeness. The same argument holds for creation of charm in the case of the Λ_c^+ hyperon. For other hyperons the relation of their spin to the spins of the individual quarks is more complicated.

The existing data for $\bar{p}p \rightarrow \bar{Y}Y$ processes are almost exclusively for single strangeness hyperons, with beam momenta from threshold up to a few GeV/c. In the upcoming PANDA experiment, antiprotons and protons will be collided at beam momentum up to 15 GeV/c, which is well above the threshold for all of the multistrange and the lightest charmed hyperons. This means that the multistrange and charmed sector of antihyperon hyperon physics will be available for detailed experimental studies for the first time. Also for the single strangeness processes, the amount of data from PANDA will exceed the existing ones by orders of magnitude. The large amount of statistics makes it promising to study the possible violation of CP symmetry in $\bar{p}p \rightarrow \bar{Y}Y$. The CP symmetry and its violation will be discussed in the next section.

1.6 CP Violation

In the understanding of particle physics, symmetry is a very important concept. A fundamental property of quantum field theory is the conservation of the symmetry CPT, where C stands for charge conjugation, P for parity transformation and T for time reversal. The parity transformation means the inversion of the axes of the reference system. It can be compared to a mirror, where left goes to right and the other way around³. The laws of physics were long thought to be symmetric under such a transformation, so that a mirror world would be the same as ours. This is indeed true for the electromagnetic and strong interaction, while it was found out in the fifties that the weak interaction does not conserve parity [16, 17].

It was then believed that if the parity transformation was combined with a charge conjugation, turning particles into antiparticles, this new CP symmetry would hold also for the weak interaction. This turned out not to be the case, since small CP violating effects were measured first in kaon systems [18, 19, 20] and later also in B-meson systems [21, 22]. Kaons are strange mesons and the B-mesons are charmed. Since CPT should be conserved, this

³A stricter description of the parity transformation is a reflection, followed by a 180° rotation.

means that also the time reversal symmetry must be broken, so that the laws of physics would not be the same if time would go backwards. T violation has also been directly measured in kaon systems [23].

One of the great puzzles of the universe is why it consists of matter and an absence of antimatter. In order for the matter to exist, somehow an asymmetry in the amount of matter compared to the amount of antimatter must have arisen, otherwise all matter would have annihilated with antimatter. In 1967 Sakharov set up three famous conditions which, if all fulfilled, could give rise to such an asymmetry [24]. One of the conditions is the violation of CP symmetry⁴. Investigating CP violation is consequently a part of trying to answer the question why anything exists at all.

The theoretical cause of CP violation of the weak interaction in the Standard Model is a complex phase in the CKM matrix. It can be shown that this way of generating CP violation is only possible if there are at least three generations of quarks. CP violation in the strong interaction could also be generated by an additional term (Θ -term [25]) in the QCD Lagrangian, but no indication of strong CP violation has been found in experiments. The reason for the non-existence of CP violation in strong interactions is an open question often referred to as the strong CP problem. The amount of CP violation within the Standard Model is far too low to account for the matter antimatter asymmetry of the universe. It is therefore important to search for sources of CP violation beyond the Standard Model.

A lot of effort has been put into finding CP violation in hyperon systems, both from the experimental and theoretical side. Various experiments have put limits on some of the hyperon CP violation parameters, but no indication of CP violation has been found so far. If it were to be found, it would be the first time CP violation is found in a baryon system. All previous measurements of CP violation are for meson systems. Furthermore, the Standard Model CP violation predictions for hyperons give very low values. Hyperon violation parameters are therefore sensitive to effects from physics beyond the Standard Model such as supersymmetry, left-right symmetric models and multicharged Higgs [26, 27, 28, 29, 30, 31].

1.7 Thesis Disposition

The thesis investigates the feasibility to study multistrange and charmed antihyperon hyperon physics at PANDA. The main focus is on spin variables, for which both calculations and simulations have been made. In addition, the possibility for setting limits on CP violation parameters in the $\bar{p}p \rightarrow \bar{Y}Y$ is explored. In studying hyperon spin, a problem can arise due to the strong magnetic field of the PANDA detector. The hyperons are relatively long-lived and

⁴The other two being violation of baryon number and that the interactions do not take place in thermal equilibrium

their spin direction can be affected by the magnetic field during their travel through the detector. The magnitude of this effect is investigated at the end of the thesis.

Chapters 2 and 4 summarise previous work, chapters 3 and 5 contain calculations performed by the author with some results which are present in the literature and some which are new, while chapters 6 and 7 present simulations performed by the author. A more detailed disposition of the thesis is as follows:

Chapter 2: PANDA

This chapter describes the FAIR facility, the planned geometry and subdetectors of the PANDA detector and the main physics topics which will be addressed with PANDA.

Chapter 3: The $\bar{p}p \rightarrow \bar{Y}Y$ Reaction

This chapter contains calculations of how hyperon spin variables are related to the angular distributions of their decay particles in the $\bar{p}p \rightarrow \bar{Y}Y$ process. The calculations are based on the density matrix formalism and are performed both for spin 1/2 and spin 3/2 hyperons. The new results for this thesis are for the spin 3/2 case. Furthermore, the CP violation parameters for the process are presented.

Chapter 4: Existing Data and Theoretical Predictions

Here, the existing data on $\bar{p}p \rightarrow \bar{Y}Y$ processes are summarised. First the present situation of how the theoretical models compare to the existing data is discussed. Then, the focus is on theoretical predictions and interesting questions for multistrange and charmed processes, for which there are little or no data and which are simulated in this work. Theoretical predictions and existing data for CP violation in $\bar{p}p \rightarrow \bar{Y}Y$ are also presented.

Chapter 5: Analysis Methods

Ways to reconstruct spin variables from data on angular distributions are deduced in this chapter. The new results are for the spin 3/2 case. Two different ways to compensate for detector acceptance are presented. In addition, CP violation parameters are related to up-down counting asymmetries, which are preferable as observables from the experimental point of view.

Chapter 6: Simulations of Multi-Strange and Charmed $\bar{p}p \rightarrow \bar{Y}Y$ Reactions

In this chapter, simulations of three different multistrange and charmed antihyperon-hyperon processes are presented: $\bar{p}p \rightarrow \bar{\Xi}^+\Xi^-$, $\bar{p}p \rightarrow \bar{\Omega}^+\Omega^-$ and $\bar{p}p \rightarrow \bar{\Lambda}_c^-\Lambda_c^+$. For the CP violation parameters, simulations of $\bar{p}p \rightarrow \bar{\Lambda}\Lambda$ and $\bar{p}p \rightarrow \bar{\Xi}^+\Xi^-$ are also presented.

Chapter 7: Precession of the Hyperon Polarisation Vector in the Magnetic Field of the PANDA Detector

This chapter presents an investigation of how the magnetic field in the PANDA detector affects the spin of the hyperons as they travel through it. The influence on the polarisation vector by the magnetic field is described and a Monte Carlo simulation of the effect for $\bar{p}p \rightarrow \bar{\Lambda}\Lambda$ is presented.

Chapter 8: Conclusions and Outlook

The conclusions from the calculations and simulations of the thesis are given in this chapter. In addition an outlook with suggestions for future studies is given.

Chapter 9: Summary in Swedish - Svensk Sammanfattning

A short popularised summary of the contents of the thesis in swedish.

2. PANDA

PANDA is an international collaboration, currently consisting of more than 500 scientists from over 50 institutions in 17 different countries. The aim of the collaborations is to build a detector for studying hadron physics in collisions of antiprotons and protons. The experiment will be located at the upcoming FAIR facility outside of Darmstadt [32], which explains the acronym: PANDA anti-Proton ANnihilation at DArmstadt. The expected startup time for the first data collection is in 2018. This chapter introduces the FAIR facility, the different parts of the PANDA detector and the different areas of hadron physics which will be studied in the PANDA experiment.

2.1 The FAIR Facility

A new international accelerator facility is under construction at the existing GSI site outside of Darmstadt in Germany. FAIR stands for Facility for Antiproton and Ion Research, and it is the largest European research infrastructure that will be built in the coming years. Figure 2.1 shows the existing GSI site together with the future FAIR facility. The existing accelerators of GSI are the UNiversal Linear ACcelerator (UNILAC), the Experimental Storage-cooler Ring (ESR) and the heavy ion synchrotron (SIS18). They will be used as injectors for the two main accelerators of FAIR, called SIS100 and SIS300 [33]. SIS100 and SIS300 are built in the same tunnel, 17 m under ground, with a circumference of 1100 m.

For the antiproton research, protons accelerated in SIS100 will be used. The beam from SIS100 will have a pulse structure, with about $5 \cdot 10^{13}$ protons per pulse. These protons, with an energy of 29 GeV, will create antiprotons in inelastic collisions with nuclei in a target made from either nickel, iridium or copper. One proton pulse will strike the target every ten seconds with a duration of 50 ns [34]. The produced antiprotons are precooled in the collector ring (CR) and then collected and decelerated in the accumulator ring (RESR)¹. They are then injected into the high-energy storage ring (HESR), where the PANDA detector will be placed. The momentum range in the HESR is from 1.5 GeV/c up to 15 GeV/c. Up to 8.9 GeV/c the antiprotons will be cooled using electron cooling, while at higher momenta stochastic cooling will be

¹The FAIR facility will be built in several consecutive steps. The RESR is not included in the startup version of FAIR, but is planned to be built in a following step.

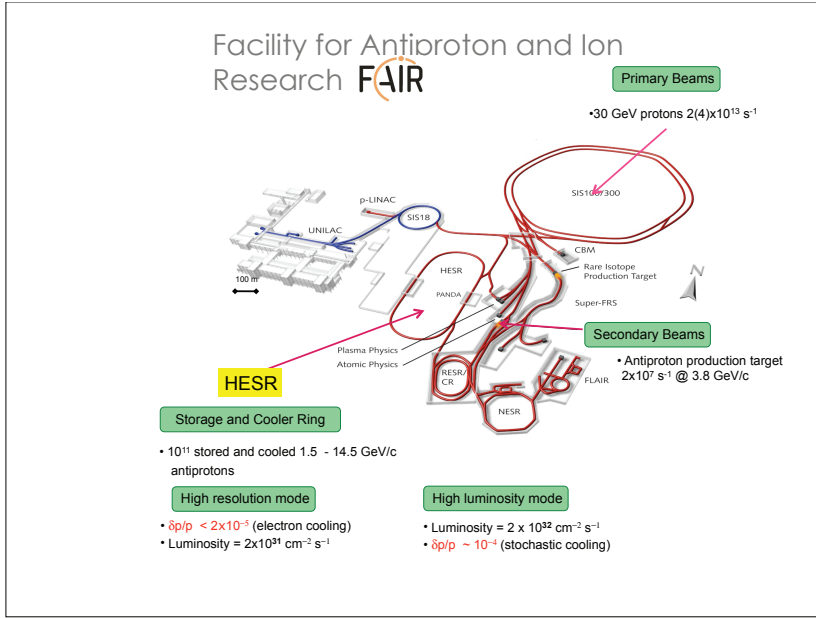


Figure 2.1: The existing GSI site together with future FAIR facility shown in red [37].

used [35]. Two different modes are planned for the experiment: high resolution mode, with a momentum resolution of $\delta p/p < 4 \cdot 10^{-5}$ and a luminosity of $2 \cdot 10^{31} \text{ cm}^{-2} \text{ s}^{-1}$, and a high luminosity mode, with a momentum resolution of $\delta p/p \approx 10^{-4}$ and a luminosity of $2 \cdot 10^{32} \text{ cm}^{-2} \text{ s}^{-1}$ [36].

Apart from PANDA, several other collaborations are planning experiments, where antiprotons or heavy ions will be used. The FLAIR experiment will study antiprotonic atoms using antiprotons cooled in the new experimental storage ring (NESR)². A lot of research is planned in the area of nucleur structure, with the use of rare radioactive isotope beams. The NUSTAR collaboration develops the Super-FRS, which is a superconducting fragment separator followed by different experimental branches. Experiments which will use the Super-FRS are R³B (reactions with relativistic radioactive beams to study reactions with exotic nuclei far from stability), HISPEC/DESPEC (studies of the classical shell gaps and magic numers, where the radioactive beams are directed onto neutron- and protonrich nuclei) and ELISE (scattering of electrons off exotic nuclei). CBM will study nuclear matter under extreme conditions, with a temperature and density that could enable quark gluon plasma to be created. The SIS300 accelerator ring will be used for CBM. The SPARC collaboration will study atomic shells under extreme conditions with highly

²The NESR and the FLAIR experiment are not included in the startup version of FAIR, but are planned for following steps.

charged very heavy ions. Plasma physics will also be studied using heavy ion beams or laser beams.

2.2 The PANDA Detector

The PANDA detector is a detector designed for hadron physics in $\bar{p}p$ collisions. The physics program is very broad and the detector is therefore rather complex with a geometrical acceptance of almost 4π . The detector is split into two main parts: the target spectrometer, which is built around the target covering tracks with large opening angles, and the forward spectrometer, for the region where most tracks are going due to the forward boost from the fixed target geometry.

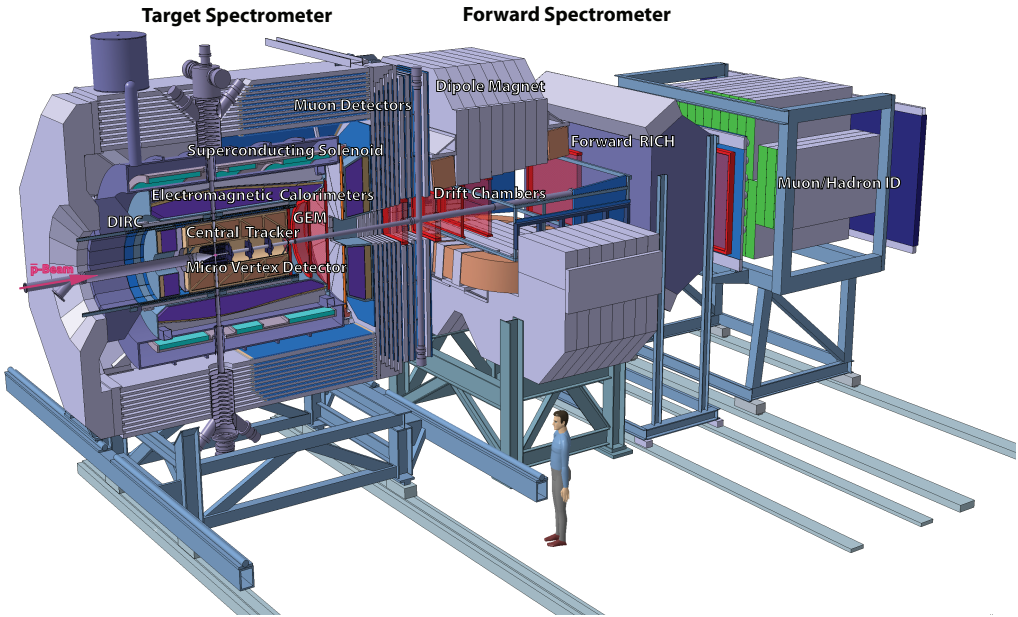


Figure 2.2: The PANDA detector [37].

The presentation in this section follows the geometry used in the simulations of this thesis, which is also the one used for the PANDA physics performance report [37]. A more detailed description of the detector layout, can be found in this report.

2.2.1 Target Spectrometer

The target spectrometer is of a cylindrical shape with a radius of about 2 m and a length of about 6 m. It consists of a barrel part for emittance angles between 22° and 140° and a forward endcap for angles down to 5° in the vertical and 10° in the horizontal direction. The geometry of the barrel part reminds of an onion, where different subdetectors are placed in layers around the beam axis. Closest to the interaction point is a micro vertex detector (MVD), followed by a central tracker. The electromagnetic calorimeter (EMC), which detects photons and electrons, will be located outside the tracker. Outside of the detectors there will be a superconducting magnet providing a 2 T solenoid field for momentum determination of charged particles [38]. The homogeneity of the field will be better than 2% in the tracking region. As an outermost part of the target spectrometer, muon detectors will be placed. The beam pipe for injection of the target material has to go through all the subdetectors in the vertical direction perpendicular to the beam axis.

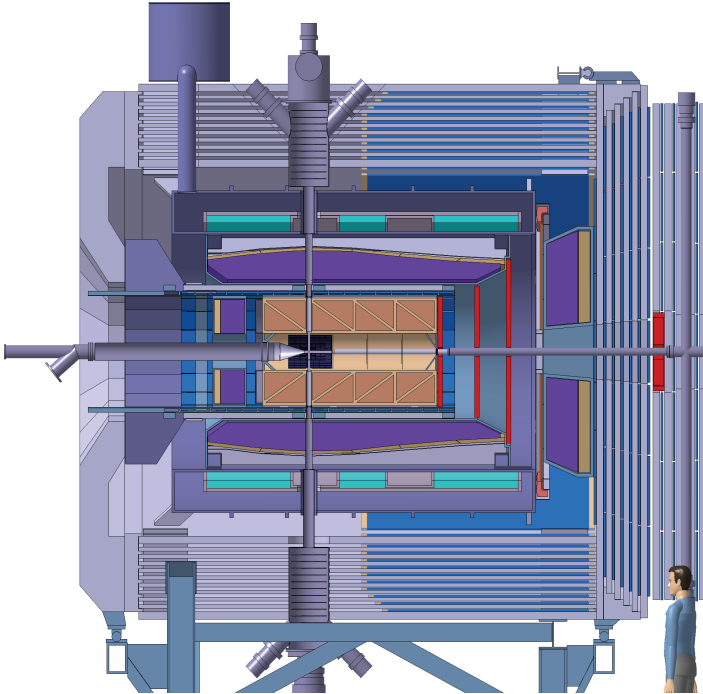


Figure 2.3: The target spectrometer [37].

2.2.1.1 Target

The PANDA experiment is designed for a luminosity of $2 \cdot 10^{32} \text{ cm}^{-2}\text{s}^{-1}$. With 10^{11} stored antiprotons in the HESR, this requires a target thickness of $4 \cdot 10^{15}$ hydrogen atoms per cm^2 . Since the place for installment in the detector is very limited, the construction of the target poses a great challenge. Two options are available which fulfils the requirements: a pellet target and a cluster jet target. Both options are planned to be used.

The pellet target generates frozen hydrogen droplets that are sent perpendicularly into the beam in the vertical direction. To create the pellets, hydrogen gas is liquified, cooled down and put into helium of low pressure, where it forms a jet, which then breaks up into a stream of droplets. This kind of target was first developed at The Svedberg Laboratory in Uppsala. It has then been used succesfully in the WASA experiment [39] both at the CELSIUS [40] and COSY [41] storage rings. The main advantage of the pellet target is a more well defined interaction point, with a beamsiz in the order of 1 mm and a pellet size of 25-40 μm . The challenge is to get a sufficiently homogenius luminosity and much of the present work is focused on making sure that the interaction rate does not instantaneously exceed the acceptance of the detector. Fuurthermore, an optical pellet tracking system [42] is being developed which could determine the interaction point to about 50 μm . Apart from hydrogen pellets, also pellets of deuterium have already been used as targets. Pellets of other gases such as N_2 , Ar and Xe are also possible [43]. The pellet target option is used for the simulations.

For the cluster jet target pressurised hydrogen gas is injected through a nozzle into vacuum where it condensates and forms a narrow jet of hydrogen clusters. This gives a lower but more homogenous density profile. A disadvantage is that the interaction point is less well determined. The width of the cluster jet should be smaller than 10 mm, so that the spread in interaction point position transversely to the beam is not too large. Cluster jet widths of this order have been obtained [44]. The position in the beam direction is not known within this extension and has to be reconstructed from data.

For hypernuclear studies different targets are needed. The whole forward endcap and part of the inner target spectrometer must then be reconfigured.

2.2.1.2 Micro Vertex Detector

Closest to the interaction point is the micro vertex detector (MVD). It is designed to detect secondary decay vertices from D mesons and hyperons. The transverse momentum resolution will also be very much improved with the help of the MVD. The MVD consists of radiation hard silicon pixel detectors with fast individual pixel readout and silicon strip detectors. The MVD geometry is shown in figure 2.4. The barrel part of the MVD, with an inner radius of 2.5 cm and an outer radius of 13 cm, consists of four layers, placed at distances 2, 4, 6 and 8 cm from the interaction point. The two closest to the interaction point are made of pixel detectors, while the following two consist

of double-sided silicon strip detectors. Outside the barrel part, for particles going in the forward direction, six detector wheels are placed perpendicular to the beam axis at distances between 15 and 22 cm. The first four are made entirely from pixel detectors and the last two have strip detectors on the outer radius and pixel detectors closest to the beam pipe.

Two silicon disk detectors are planned outside of the central MVD, at distances 40 and 60 cm. They are important for increasing the acceptance for long-lived hyperons. In the detector geometry used for the simulations they are included. More information about the MVD can be found in [45].

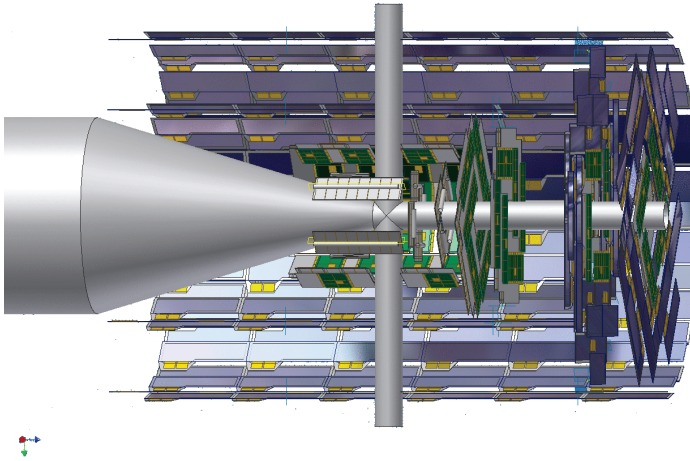


Figure 2.4: The micro vertex detector [37].

2.2.1.3 Tracking

Apart from the MVD, the tracking in the target spectrometer is divided into a central tracker, which lies outside of the MVD and covers large angles and three layers of GEM trackers for the forward angles. The tracking is designed to have a good efficiency in reconstructing decay vertices outside of the MVD and a momentum resolution $\delta p/p$ which does not exceed a few per cent.

For a long time there have been two options for the central tracker: straw tube tracker (STT) and time projection chamber (TPC). Recently the decision has fallen on the STT, which is shown in figure 2.5. The STT is also what is used for the simulations. The straws of the STT are thin aluminised mylar tubes filled with a gas mixture of Ar and CO₂, with a stretched wire in the middle. Charged particles which enter the straws will ionize the gas. An electric field is applied, causing the electrons and positive ions to drift in opposite directions. With a sufficiently thin wire and high voltage, the gas will further ionize close to it, which amplifies the signal for readout.

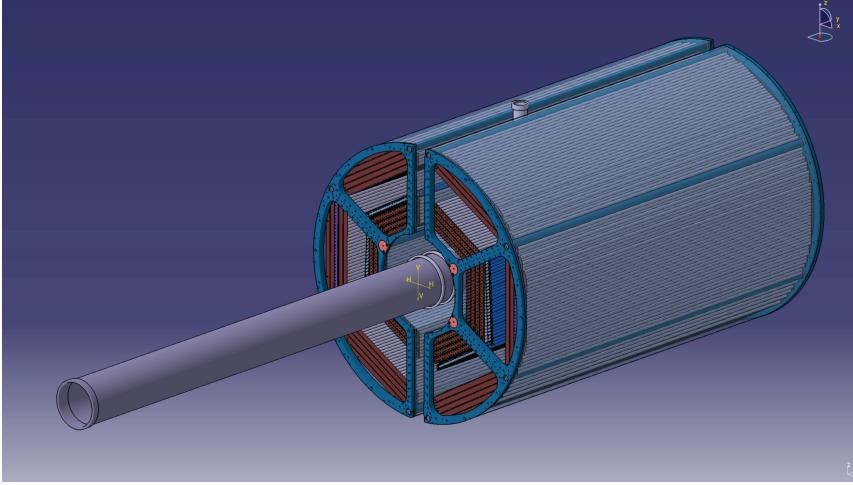


Figure 2.5: The straw tube tracker [37].

The STT will have 4200 straws, which are placed in 24 layers with radial distance from the beam between 15 and 42 cm. The straws will have a diameter of 10 mm and a length of 150 cm. The inner 8 layers will be skewed, so that the position of the hit in the direction parallel to the beam can be given with an expected resolution of about 3 mm. The straws are made from 30 μm mylar foil, with the wire being 20 μm gold plated tungsten. The mixture of gas will not have a higher gain than 10^5 , to allow for the detector to operate for a long time. The resolution in the directions perpendicular to the beam is expected to be 150 μm . More information about the STT can be found in [46].

For angles below 22° , where the tracking is not completely covered by the STT, three sets of gas electron multiplier (GEM) trackers are installed. They are placed 1.1, 1.4 and 1.9 m down the beam direction. Due to the forward boost of the reactions there will be many tracks in this region, so the requirement on count rate capacity is very tough. Therefore, instead of drift chambers, GEM trackers with three orders of magnitude higher rate capabilities are used. The GEM trackers are gaseous micropattern detectors based on amplification stages using GEM foils. The GEM foils are metal-coated polymer which are pierced with many holes. If a high voltage is applied over the detector the field in the holes can become sufficiently strong, causing the primary electrons which are collected in them to give rise to an avalanche of secondary electrons. There will be three double planes with two projections per plane. A readout plane has strips in two orthogonal projections and is divided into an

inner ring with shorter strips and an outer ring with longer strips. A strong correlation between orthogonal strips can be found from the charge sharing between the strips, which gives almost 2D information instead of just two projections.

Tracks in the target spectrometer are reconstructed by combining hits in the MVD, STT and GEM detectors. The momenta of particles are given by their bending radius in the strong 2 T magnetic solenoid field. Particles with small polar angles will exit the solenoid field too quickly for a proper measurement in the target spectrometer. Many of these particles will be covered by the dipole magnet and tracking of the forward spectrometer.

2.2.1.4 Particle Identification

A good particle identification is necessary for a large momentum range from 200 MeV/c to 10 GeV/c, in order to study the wide range of hadron physics topics foreseen. The PANDA detector will be able to identify five different particle types: e , μ , π , K and p.

For particles with momenta above 1 GeV/c the particle identification is performed by Cherenkov detectors³. There will be two DIRC detectors⁴, one in the barrel part for polar angles from 22° to 140° and one in the forward endcap for polar angles from 5° and 22° . The barrel DIRC consists of 1.7 cm thick quartz slabs located at a radial distance 45 to 54 cm from the beam pipe. The Cherenkov light is focused onto micro channel plate photomultiplier tubes, which have the advantage that they are insensitive to magnetic fields. The same material is used for the forward endcap DIRC, but the radiator will in this case be in the form of a 2 cm thick disc with a radius of 110 cm, placed directly behind the forward endcap calorimeter. Focusing will be done at the rim around the disc, using quartz elements, which reflects onto micro channel plate photomultiplier tubes. The light will be measured at the rim around the disc by focusing elements. A similar detector was used in the BaBar detector [47].

For particles with lower momenta, the particles will be identified using the fact that their energy loss, dE/dx , in materials depend on the particle type. Information about dE/dx will be given from the MVD and the STT.

Slow particles with large polar angles will be identified with the use of a time of flight (TOF) detector, located just outside the STT at radial distance 42 to 45 cm, covering angles between 22° and 140° . A very good time resolution of 50-100 ps will be needed, due to the short flight path. There will be no start detector, since that would introduce too much material close to the interaction point. Instead, relative timing between different particles will be used. In choosing a suitable detector, the consideration was a balance between time resolution and material budget. The choice fell on a detector based on

³Detectors based on the principle that particles travelling at speeds above the speed of light in the specific material emits light at a certain angle determined by the velocity.

⁴Detection of Internally Reflected Cherenkov light

scintillating tiles, with less than 2% of a radiation length and the ability to achieve a time resolution better than 100 ps. The TOF detector is not included in the simulations.

2.2.1.5 Electromagnetic Calorimeter

The electromagnetic calorimeter (EMC) is the most expensive subdetector of PANDA, consisting of approximately 15500 scintillating crystals divided into three parts: a barrel part around the beam, a forward and a backward endcap. The barrel and forward endcap part is shown in figure 2.6.

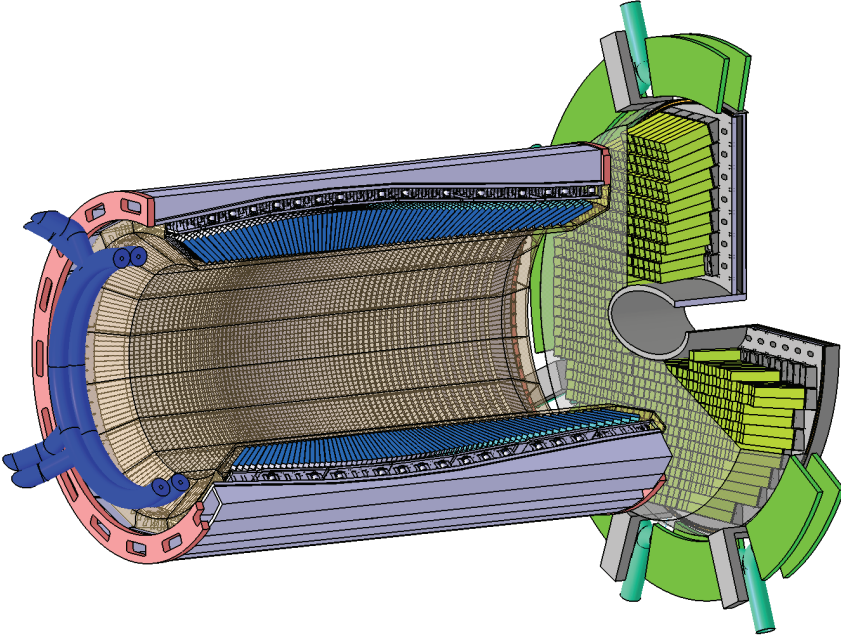


Figure 2.6: The electromagnetic calorimeter [37].

The EMC must be able to handle high count rates and be reasonably compact. Also, the energy range of the photons that will be detected is very wide, ranging from a few MeV up to some GeV. It has therefore been decided to use lead tungstate crystals (PbWO_4) for the EMC. This is a material with many attractive features, which is also used by the high energy physics experiments CMS and ALICE at CERN [48, 49]. This material is dense, radiation hard, has a short radiation length and Moliere radius, and a fast decay time of the scintillation process. The disadvantage is that the light yield is relatively low. One way to increase the light yield is to cool the crystals. For that reason the EMC will be operated at -25°C , which will increase the light yield with a factor of four, as compared to room temperature.

The barrel part will be 2.5 m long, consisting of 11360 crystals. The crystals are placed in rings with an inner radius of 60 cm. The crystals are not

directed directly to the interaction region, but are tilted about 4° . The reason for this is to avoid photons escaping detection by going along the gap between two crystals. The forward endcap, with 3600 crystals, is placed 2.1 m from the target and has a diameter 2 m. The smaller backward endcap, with 592 crystals, is placed 1 m from the target and has a diameter 0.8 m. All crystals will be 200 mm long, which corresponds to about 22 radiation lengths. With crystals of this length an energy resolution below 2% at 1 GeV is obtained [50, 51, 52]. The shape of the crystals depend on where they will be placed in the detector. In the backward endcap the crystals are rectangular, whereas in the other parts they are tapered in various degrees. In total eleven different shapes will be used. More information about the EMC can be found in [53].

2.2.2 Forward Spectrometer

Particles emitted with angles smaller than 5° in the vertical and 10° in the horizontal direction can not be detected with the target spectrometer. They will enter into the forward spectrometer. This spectrometer is an essential part of the detector, since many tracks go in the very forward direction in fixed target experiments. It has similar subdetectors as the target spectrometer: a tracking system with a dipole magnet, an electromagnetic calorimeter, particle identification and muon detectors. A magnet with a gap opening of $1 \times 3 \text{ m}^2$ will supply a 2 T dipole field for the forward tracking. Further down the beam pipe a luminosity monitor will be placed, for determination of the total integrated luminosity during cross section measurements.

2.2.2.1 Forward Tracking

To allow for tracking of particles with both high and low momenta two wire chambers will be put in front of the dipole magnet, two within and two behind. The wire chambers will be made from double layer straw tubes. To be able to reconstruct tracks in each chamber separately, they will each have three detection layers, one with vertical wires and two with wires inclined $\pm 5^\circ$. A momentum resolution of $\delta p/p = 2 \cdot 10^{-3}$ for 3 GeV/c protons is expected.

2.2.2.2 Forward Particle Identification

Two detectors are planned for particle identification in the forward spectrometer, a RICH detector⁵ and a Time-of-Flight Wall.

The RICH detector will supply particle identification for high momentum particles, providing $\pi/K/p$ separation in a momentum range between 200 MeV/c and 15 GeV/c. It will use components from the RICH detector of the HERMES experiment at DESY [54]. The separation of $\pi/K/p$ is obtained by using two different radiators, silica aerogel and C_4F_{10} gas.

⁵Ring-Imaging CHerenkov detector

The Time-of-Flight wall will be placed 7 m from the target and consist of slabs made of plastic scintillators. Additional detectors of the same type will be put inside the dipole magnet opening, for low momentum particles which do not leave the dipole magnet. Relative timing between any two of all the charged tracks reaching the detectors will be measured. With the expected time resolution of 50 ps, a 3σ separation of π/K and K/p will be possible up to 2.8 GeV/c and 4.7 GeV/c, respectively.

Neither of the particle identification detectors of the forward spectrometer are included in the simulations.

2.2.2.3 Forward Electromagnetic Calorimeter

The forward electromagnetic calorimeter will be of Shahlyk type. This means that several scintillator layers are separated by lead layers which works as absorbers and photon converters. Similar detectors have been used in various other experiments and the resolution is expected to be about the same as for the E865 experiment at BNL [55], which was 4%. The forward calorimeter will be placed 7.5 m from the target.

2.3 PANDA Physics

Using data from the PANDA experiment, many different questions in the field of hadron physics can be addressed. Apart from the antihyperon-hyperon physics described in this thesis, some of the major topics which are focused on are:

- QCD bound states

An important aspect in studies of QCD is to understand the spectra of bound states. There are several approaches to calculate these spectra: non-relativistic potential models, effective field theories and lattice QCD. Precise measurements are needed to discriminate between different models. The focus of PANDA will be on the charmonium spectrum. The low lying charmonium states are similar to the positronium spectrum, and the understanding of charmonium from the strong interaction is analogue to the understanding of positronium in the electroweak theory. Since the mass of the c quarks are comparable to the mass of the states, non-relativistic models are applicable. The states of charmonium are narrow below the open charm threshold, which is an advantage in the search for new exotic states. Above the open charm threshold very little is known experimentally, but interesting new physics is expected. By scanning over the states using different beam momenta of the HESR, the measured width will not be determined by the detector resolution but only limited by the spread in beam momentum. In this way PANDA will be able to measure the states with very good resolution.

- Search for gluonic hadrons and multiquark states

As already mentioned in the introduction no hadron of more complex structure than that of the ordinary mesons and baryons has been experimentally confirmed. There is in principle no theoretical reason why such exotic hadrons should not exist. One way to compose more complex hadrons is to include gluonic degrees of freedom. Two sorts of gluonic hadrons are thought to exist: glueballs, which are pure gluonic states, and hybrids, which consist of a quarks and constituent gluons. Gluonic hadrons may have quantum numbers which can not be formed from ordinary hadron states. Such states are said to have exotic quantum numbers. An important advantage of $\bar{p}p$ colliders compared to e^+e^- colliders, is that states with any non-exotic quantum number can be observed already in formation⁶ mode, while the quantum number is restricted to that of the intermediate photon $J^{PC} = 1^{--}$ in e^+e^- collisions. Possible states

⁶A resonance is formed which then decays to several particles.

with exotic quantum numbers can be formed in production⁷ mode. The observation of a state in production mode but not in formation mode is therefore a clear indication of exotic quantum numbers. Calculations from lattice QCD predict about 15 different glueballs, some of them with exotic quantum numbers, with masses that make them accessible to PANDA. Exotic charmonium hybrids are expected to exist in the 3-5 GeV/c² mass region, where they can be resolved and unambiguously identified with PANDA. Other complex compositions of hadrons are multiquark states, which are colourless combinations of more quarks than the three quark or quark antiquark structure of baryons and mesons.

- Studies of nucleon form factors

Studies of the nucleon structure are also planned for PANDA. Electromagnetic processes such as deeply virtual Compton scattering and $\bar{p}p \rightarrow e^+e^-$, will be used to determine the electromagnetic form factors of the proton in the timelike region. A lot of focus is given to generalized parton distributions (GPDs), which has been succesful in treating hard exclusive processes in lepton scattering, under conditions where it is possible to factorize short and long distance contributions to the reaction mechanism. GPDs are related to non-diagonal matrix elements, so that they do not only represent probabilities, but also include interference between amplitudes. It is interesting to test wether the method is universal and can be used in $\bar{p}p$ annihilation processes.

- Studies of hadrons in nuclear medium

The masses of hadrons change when they are embedded in a finite nuclear density. The reason for this is believed to be a modification of chiral symmetry breaking of QCD, which is thought to be partially restored in the nuclear medium. Studies of these modifications can give insight into the QCD vacuum and the origin of the hadron masses. Also the width of the hadrons change, in general by an increase, since more decay modes become available for the bound hadrons. Measuring the change in width can give insight into the inelastic interactions of unstable hadrons, which is hard to get in other ways. The PANDA experiment will allow to extend such studies of hadrons in nuclear medium into the charmed sector by using antiproton-nucleus collisions.

⁷The state is formed directly together with other particles.

- Studies of hypernuclei

A hypernucleus is a nucleus where one or more of the nucleons are replaced by a hyperon. In this way a third dimension of the nuclear chart is introduced. The purpose of hypernuclei studies is to get a better insight into both nuclear structure and properties of hyperons. Level schemes in nuclei are created by applying the Pauli principle to protons and neutrons separately. Being of a different particle type, a hyperon in a nucleus will not be affected by the protons and neutrons, with respect to the Pauli principle. This means that deeply bound states of hypernuclei are accessible to experiment. Such deeply bound states are difficult to study in ordinary nuclei due to the Pauli blocking, so that hypernuclei can give valuable information to the field of nuclear structure. While it is hard to get information about nucleon-hyperon interactions from scattering experiments, studying hyperons bound in hypernuclei may be a good way to extract this information. In the PANDA experiment, it is also planned to study double hypernuclei, which in a similar way can give information about the hyperon-hyperon interaction. So far only a few events with double hypernuclei have been detected. Hypernuclei also have a connection to astrophysics, since hyperons may be present in neutron stars, affecting their properties.

More detailed information about these and other topics can be found in [37].

3. The $\bar{p}p \rightarrow \bar{Y}Y$ Reaction

The parity violating weak decay of hyperons means that information about their spin degrees of freedom is accessible by studying the angular distribution of their decay particles. In the $\bar{p}p \rightarrow \bar{Y}Y$ reaction, many spin variables are open for study. For the PANDA experiment, where both the beam and target are unpolarised, the non-zero spin variables are the polarisation of the individual hyperon/antihyperon and certain correlations of their spins. In this chapter the angular distributions of the hyperon decays, and their dependence on spin variables, are deduced. Both the spin 1/2 case and the more complex spin 3/2 case are considered. Another interesting aspect of the $\bar{p}p \rightarrow \bar{Y}Y$ reaction is that both the initial and final state are CP eigenstates, which makes it suitable for studies of possible CP violation. This is addressed in the last part of this chapter.

3.1 Spin Variables

To derive the dependence of the angular distributions on spin variables, it is very convenient to use the density matrix formalism. Therefore this section starts with a short introduction to the density matrix.

3.1.1 The Density Matrix

The density matrix formalism, developed in 1927 by von Neumann, is a way to describe ensembles in quantum mechanics [56]. In a pure ensemble every member is described by the same ket $|\Psi\rangle$, while for a mixed state different fractions, populated by the amount a_i , are described by different kets $|\Psi_i\rangle$. For a pure state the expectation value of an observable E is given by

$$\langle E \rangle = \langle \Psi | E | \Psi \rangle \quad . \quad (3.1)$$

In an orthonormal basis $\{|\alpha_k\rangle\}$ the expectation value can be rewritten as

$$\begin{aligned}
\langle E \rangle &= \langle \Psi | \left(\sum_k |\alpha_k\rangle \langle \alpha_k| \right) E | \Psi \rangle = \sum_k \langle \Psi | \alpha_k \rangle \langle \alpha_k | E | \Psi \rangle = \\
&= \sum_k \langle \alpha_k | E | \Psi \rangle \langle \Psi | \alpha_k \rangle = \text{Tr}(E | \Psi \rangle \langle \Psi |) \quad .
\end{aligned} \tag{3.2}$$

If we define the density matrix as $\rho \equiv |\Psi\rangle \langle \Psi|$, we have

$$\langle E \rangle = \text{Tr}(E\rho) \quad . \tag{3.3}$$

All physics information about the ensemble is contained in the density matrix. With a slight modification it is also possible to define the density matrix for a mixed state, for which eq.(3.2) becomes

$$\begin{aligned}
\langle E \rangle &= \sum_i a_i \langle \Psi_i | E | \Psi_i \rangle = \sum_i a_i \langle \Psi_i | \left(\sum_k |\alpha_k\rangle \langle \alpha_k| \right) E | \Psi_i \rangle = \\
&= \sum_k \langle \alpha_k | \left(E \sum_i a_i |\Psi_i\rangle \langle \Psi_i| \right) | \alpha_k \rangle = \text{Tr} \left(E \sum_i a_i |\Psi_i\rangle \langle \Psi_i| \right) \quad .
\end{aligned} \tag{3.4}$$

The expression for the expectation value in eq.(3.3) is again achieved if the density matrix is now defined as $\rho \equiv \sum_i a_i |\Psi_i\rangle \langle \Psi_i|$. For a pure state $\text{Tr}(\rho) = 1$, which also holds for a mixed state if $\sum_i a_i = 1$. The density matrix is also hermitian since

$$\rho^\dagger = (|\Psi\rangle \langle \Psi|)^\dagger = \langle \Psi |^\dagger | \Psi \rangle^\dagger = |\Psi\rangle \langle \Psi| = \rho \quad . \tag{3.5}$$

What also is needed to know about the density matrix is its transformation properties. Let T be a transformation of $|\Psi_i\rangle$, with its physical meaning being a transition from the initial to the final state of a reaction, so that $T|\Psi_i\rangle = t_i|\Psi'_i\rangle$. The eigenvalues are then given by $t_i = \sqrt{\langle \Psi_i | T^\dagger T | \Psi_i \rangle}$, which ensures normalisation of $|\Psi'_i\rangle$, since

$$\langle \Psi'_i | \Psi'_i \rangle = \frac{1}{|t_i|^2} \langle \Psi_i | T^\dagger T | \Psi_i \rangle = 1 \quad . \tag{3.6}$$

Then, the density matrix transforms as

$$\rho_{\text{final}} = T \rho_{\text{initial}} T^\dagger \quad . \tag{3.7}$$

Writing this out explicitly, we have

$$T\rho_{\text{initial}}T^\dagger = T\left(\sum_i a_i|\Psi_i\rangle\langle\Psi_i|\right)T^\dagger = \sum_i a_i T|\Psi_i\rangle\langle\Psi_i|T^\dagger = \sum_i a_i t_i^2 |\Psi'_i\rangle\langle\Psi'_i| \quad (3.8)$$

which gives back eq.(3.7) if $a'_i = a_i t_i^2$ and $\rho_{\text{final}} = \sum_i a'_i |\Psi'_i\rangle\langle\Psi'_i|$.

Combining eq.(3.3) and eq.(3.7), the angular distribution of the daughter particles of a decay is given by [57]

$$I = \text{Tr}(T\rho_{\text{initial}}T^\dagger) \quad (3.9)$$

where T describes the decay.

3.1.2 Hyperon Density Matrices

To get the density matrix for a particle of arbitrary spin j , one may use an expansion in hermitian matrices Q_M^L [58, 59]

$$\rho = \frac{1}{2j+1} \mathcal{I} + \sum_{L=1}^{2j} \rho^L \quad (3.10)$$

with

$$\rho^L = \frac{2j}{2j+1} \sum_{M=-L}^L Q_M^L r_M^L \quad (3.11)$$

and where \mathcal{I} is the identity matrix. Using this normalisation the particle's degree of polarisation is given by

$$d(\rho) = \sqrt{\sum_{L=1}^{2j} \sum_{M=-L}^L (r_M^L)^2} \quad (3.12)$$

The Q_M^L matrices are related to the multipoles T_M^L through

$$\begin{aligned} Q_0^L &= \sqrt{\frac{2L+1}{2j}} T_0^L \\ Q_M^L &= (-1)^M \sqrt{\frac{2L+1}{j}} \frac{1}{2} (T_M^L + T_M^{L\dagger}) \\ Q_{-M}^L &= (-1)^M \sqrt{\frac{2L+1}{j}} \frac{1}{2i} (T_M^L - T_M^{L\dagger}) \quad \text{where } M > 0 \end{aligned} \quad (3.13)$$

To get an explicit expression for the density matrix, the components of T_M^L can be calculated using Wigner's $3j$ symbol

$$(T_M^L)_n^m = \sqrt{2j+1} \begin{pmatrix} m & L & j \\ j & M & n \end{pmatrix} = \langle jnLM | jm \rangle \quad . \quad (3.14)$$

3.1.2.1 The Spin 1/2 Hyperons

Most low mass hyperons are spin 1/2 particles. For spin 1/2 the density matrix takes a very simple form. The Q_M^1 matrices become the Pauli matrices and the corresponding r_M^1 can be interpreted as the vector polarisation

$$\rho(1/2) = \begin{bmatrix} \rho_{11} & \rho_{1-1} \\ \rho_{-11} & \rho_{-1-1} \end{bmatrix} = \frac{1}{2}(\mathcal{I} + \vec{P} \cdot \vec{\sigma}) = \frac{1}{2} \begin{bmatrix} 1 + P_z & P_x + iP_y \\ P_x - iP_y & 1 - P_z \end{bmatrix} \quad . \quad (3.15)$$

In the case of hyperons created by strong interaction in the $\bar{p}p \rightarrow \bar{Y}Y$ process, the conservation of parity can be used to impose symmetries of the density matrix. With the hyperon rest system constructed in such a way that the x - and z -axes form the production plane, the symmetries from parity conservation are [57]

$$\rho(1/2) = \begin{bmatrix} \rho_{11} & \rho_{1-1} \\ -\rho_{1-1} & \rho_{11} \end{bmatrix} \quad . \quad (3.16)$$

Comparing with eq.(3.15) this means $P_x = P_z = 0$, i.e. the hyperon is only polarised perpendicular to the production plane, so that

$$\rho(1/2) = \frac{1}{2} \begin{bmatrix} 1 & iP_y \\ -iP_y & 1 \end{bmatrix} \quad . \quad (3.17)$$

3.1.2.2 The Spin 3/2 Ω Hyperon

The Ω hyperon has spin 3/2, which makes the density matrix much more complicated. The L number in eq.(3.10) now takes on the values 1, 2 and 3. As before the Q_M^1 matrices are the three spin matrices (with a normalisation factor $\frac{2}{\sqrt{15}}$)

$$\begin{aligned}
Q_0^1 &= \frac{2}{\sqrt{15}} \begin{bmatrix} \frac{3}{2} & 0 & 0 & 0 \\ 0 & \frac{1}{2} & 0 & 0 \\ 0 & 0 & -\frac{1}{2} & 0 \\ 0 & 0 & 0 & -\frac{3}{2} \end{bmatrix}, \quad Q_1^1 = \frac{2}{\sqrt{15}} \begin{bmatrix} 0 & -\frac{\sqrt{3}}{2} & 0 & 0 \\ -\frac{\sqrt{3}}{2} & 0 & -1 & 0 \\ 0 & -1 & 0 & -\frac{\sqrt{3}}{2} \\ 0 & 0 & -\frac{\sqrt{3}}{2} & 0 \end{bmatrix}, \\
Q_{-1}^1 &= \frac{2}{\sqrt{15}} \begin{bmatrix} 0 & \frac{\sqrt{3}}{2}i & 0 & 0 \\ -\frac{\sqrt{3}}{2}i & 0 & i & 0 \\ 0 & -i & 0 & \frac{\sqrt{3}}{2}i \\ 0 & 0 & -\frac{\sqrt{3}}{2}i & 0 \end{bmatrix}.
\end{aligned} \tag{3.18}$$

There are five Q_M^2 matrices, which corresponds to products of two spin matrices. The explicit expressions are

$$\begin{aligned}
Q_0^2 &= \frac{1}{\sqrt{3}} \begin{bmatrix} 1 & 0 & 0 & 0 \\ 0 & -1 & 0 & 0 \\ 0 & 0 & -1 & 0 \\ 0 & 0 & 0 & 1 \end{bmatrix}, \quad Q_1^2 = \frac{1}{\sqrt{3}} \begin{bmatrix} 0 & -1 & 0 & 0 \\ -1 & 0 & 0 & 0 \\ 0 & 0 & 0 & 1 \\ 0 & 0 & 1 & 0 \end{bmatrix}, \\
Q_{-1}^2 &= \frac{1}{\sqrt{3}} \begin{bmatrix} 0 & i & 0 & 0 \\ -i & 0 & 0 & 0 \\ 0 & 0 & 0 & -i \\ 0 & 0 & i & 0 \end{bmatrix}, \quad Q_2^2 = \frac{1}{\sqrt{3}} \begin{bmatrix} 0 & 0 & 1 & 0 \\ 0 & 0 & 0 & 1 \\ 1 & 0 & 0 & 0 \\ 0 & 1 & 0 & 0 \end{bmatrix}, \\
Q_{-2}^2 &= \frac{1}{\sqrt{3}} \begin{bmatrix} 0 & 0 & -i & 0 \\ 0 & 0 & 0 & -i \\ i & 0 & 0 & 0 \\ 0 & i & 0 & 0 \end{bmatrix}.
\end{aligned} \tag{3.19}$$

Finally, there are seven Q_M^3 matrices, which corresponds to triple products of spin matrices

$$\begin{aligned}
Q_0^3 &= \frac{1}{\sqrt{15}} \begin{bmatrix} 1 & 0 & 0 & 0 \\ 0 & -3 & 0 & 0 \\ 0 & 0 & 3 & 0 \\ 0 & 0 & 0 & -1 \end{bmatrix}, \quad Q_1^3 = \frac{1}{\sqrt{15}} \begin{bmatrix} 0 & \sqrt{2} & 0 & 0 \\ \sqrt{2} & 0 & -\sqrt{6} & 0 \\ 0 & -\sqrt{6} & 0 & \sqrt{2} \\ 0 & 0 & \sqrt{2} & 0 \end{bmatrix}, \\
Q_{-1}^3 &= \frac{1}{\sqrt{15}} \begin{bmatrix} 0 & -\sqrt{2}i & 0 & 0 \\ \sqrt{2}i & 0 & \sqrt{6}i & 0 \\ 0 & -\sqrt{6}i & 0 & -\sqrt{2}i \\ 0 & 0 & \sqrt{2}i & 0 \end{bmatrix}, \quad Q_2^3 = \frac{1}{\sqrt{15}} \begin{bmatrix} 0 & 0 & \sqrt{5} & 0 \\ 0 & 0 & 0 & -\sqrt{5} \\ \sqrt{5} & 0 & 0 & 0 \\ 0 & -\sqrt{5} & 0 & 0 \end{bmatrix}, \\
Q_{-2}^3 &= \frac{1}{\sqrt{15}} \begin{bmatrix} 0 & 0 & -\sqrt{5}i & 0 \\ 0 & 0 & 0 & \sqrt{5}i \\ \sqrt{5}i & 0 & 0 & 0 \\ 0 & -\sqrt{5}i & 0 & 0 \end{bmatrix}, \quad Q_3^3 = \frac{1}{\sqrt{15}} \begin{bmatrix} 0 & 0 & 0 & \sqrt{10} \\ 0 & 0 & 0 & 0 \\ 0 & 0 & 0 & 0 \\ \sqrt{10} & 0 & 0 & 0 \end{bmatrix}, \\
Q_{-3}^3 &= \frac{1}{\sqrt{15}} \begin{bmatrix} 0 & 0 & 0 & -\sqrt{10}i \\ 0 & 0 & 0 & 0 \\ 0 & 0 & 0 & 0 \\ \sqrt{10}i & 0 & 0 & 0 \end{bmatrix}.
\end{aligned}
\tag{3.20}$$

Inserting all the Q_M^L matrices into eq.(3.10) gives the following density matrix

$$\begin{aligned}
\rho(3/2) = & \\
= \frac{1}{4} & \left[\begin{array}{cccc}
1 + 3\sqrt{\frac{3}{5}}r_0^1 + & -\frac{3}{\sqrt{5}}r_1^1 + i\frac{3}{\sqrt{5}}r_{-1}^1 - & \sqrt{3}r_2^2 - i\sqrt{3}r_{-2}^2 + & \sqrt{6}r_3^3 - i\sqrt{6}r_{-3}^3 \\
+ \sqrt{3}r_0^2 + \sqrt{\frac{3}{5}}r_0^3 & -\sqrt{3}r_1^2 + i\sqrt{3}r_{-1}^2 + & + \sqrt{3}r_2^3 - i\sqrt{3}r_{-2}^3 & \\
& + \sqrt{\frac{6}{5}}r_1^3 - i\sqrt{\frac{6}{5}}r_{-1}^3 & & \\
-\frac{3}{\sqrt{5}}r_1^1 - i\frac{3}{\sqrt{5}}r_{-1}^1 - & 1 + \sqrt{\frac{3}{5}}r_0^1 - & -2\sqrt{\frac{3}{5}}r_1^1 + i2\sqrt{\frac{3}{5}}r_{-1}^1 - & \sqrt{3}r_2^2 - i\sqrt{3}r_{-2}^2 - \\
-\sqrt{3}r_1^2 - i\sqrt{3}r_{-1}^2 & -\sqrt{3}r_0^2 - 3\sqrt{\frac{3}{5}}r_0^3 & -3\sqrt{\frac{2}{5}}r_1^3 + i3\sqrt{\frac{2}{5}}r_{-1}^3 & -\sqrt{3}r_2^3 + i\sqrt{3}r_{-2}^3 \\
+ \sqrt{\frac{6}{5}}r_1^3 + i\sqrt{\frac{6}{5}}r_{-1}^3 & & & \\
\sqrt{3}r_2^2 + i\sqrt{3}r_{-2}^2 + & -2\sqrt{\frac{3}{5}}r_1^1 - i2\sqrt{\frac{3}{5}}r_{-1}^1 - & 1 - \sqrt{\frac{3}{5}}r_0^1 - & -\frac{3}{\sqrt{5}}r_1^1 + i\frac{3}{\sqrt{5}}r_{-1}^1 + \\
+ \sqrt{3}r_2^3 + i\sqrt{3}r_{-2}^3 & -3\sqrt{\frac{2}{5}}r_1^3 - i3\sqrt{\frac{2}{5}}r_{-1}^3 & -\sqrt{3}r_0^2 + 3\sqrt{\frac{3}{5}}r_0^3 & + \sqrt{3}r_2^1 - i\sqrt{3}r_{-2}^1 + \\
& & & + \sqrt{\frac{6}{5}}r_1^3 - i\sqrt{\frac{6}{5}}r_{-1}^3 \\
\sqrt{6}r_3^3 + i\sqrt{6}r_{-3}^3 & \sqrt{3}r_2^2 + i\sqrt{3}r_{-2}^2 - & -\frac{3}{\sqrt{5}}r_1^1 - i\frac{3}{\sqrt{5}}r_{-1}^1 + & 1 - 3\sqrt{\frac{3}{5}}r_0^1 + \\
& -\sqrt{3}r_2^3 - i\sqrt{3}r_{-2}^3 & + \sqrt{3}r_1^2 + i\sqrt{3}r_{-1}^2 + & + \sqrt{3}r_0^2 - \sqrt{\frac{3}{5}}r_0^3 \\
& & + \sqrt{\frac{6}{5}}r_1^3 + i\sqrt{\frac{6}{5}}r_{-1}^3 &
\end{array} \right] \quad (3.21)
\end{aligned}$$

As in the spin 1/2 case, parity conservation in the creation mechanism of the particle impose symmetries on the density matrix [57]

$$\rho(3/2) = \begin{bmatrix} \rho_{33} & \rho_{31} & \rho_{3-1} & \rho_{3-3} \\ \rho_{31}^* & \rho_{11} & \rho_{1-1} & \rho_{3-1}^* \\ \rho_{3-1}^* & -\rho_{1-1} & \rho_{11} & -\rho_{31}^* \\ -\rho_{3-3} & \rho_{3-1} & -\rho_{31} & \rho_{33} \end{bmatrix}. \quad (3.22)$$

Using these symmetries eight of the fifteen r coefficients can be set to zero and eq.(3.21) reduces to

$$\begin{aligned}
\rho(3/2) &= \\
&= \frac{1}{4} \begin{bmatrix}
1 + \sqrt{3}r_0^2 & i\frac{3}{\sqrt{5}}r_{-1}^1 - \sqrt{3}r_1^2 & \sqrt{3}r_2^2 - i\sqrt{3}r_{-2}^3 & -i\sqrt{6}r_{-3}^3 \\
-i\frac{3}{\sqrt{5}}r_{-1}^1 - \sqrt{3}r_1^2 & 1 - \sqrt{3}r_0^2 & i2\sqrt{\frac{3}{5}}r_{-1}^1 + i3\sqrt{\frac{2}{5}}r_{-1}^3 & \sqrt{3}r_2^2 + i\sqrt{3}r_{-2}^3 \\
\sqrt{3}r_2^2 + i\sqrt{3}r_{-2}^3 & -i2\sqrt{\frac{3}{5}}r_{-1}^1 - i3\sqrt{\frac{2}{5}}r_{-1}^3 & 1 - \sqrt{3}r_0^2 & i\frac{3}{\sqrt{5}}r_{-1}^1 + \sqrt{3}r_1^2 \\
i\sqrt{6}r_{-3}^3 & \sqrt{3}r_2^2 - i\sqrt{3}r_{-2}^3 & -i\frac{3}{\sqrt{5}}r_{-1}^1 + \sqrt{3}r_1^2 & 1 + \sqrt{3}r_0^2
\end{bmatrix}.
\end{aligned} \tag{3.23}$$

Compared to the spin 1/2 particle, where the total polarisation of the particle is in one component of the vector polarisation, the situation is here more complicated. To get the polarisation, the seven remaining r coefficients, r_{-3}^3 , r_{-2}^3 , r_{-1}^3 , r_2^2 , r_1^2 , r_0^2 and r_{-1}^1 , need to be measured.

3.1.3 Angular Distributions for Hyperon Decays

The elements of the hyperon density matrix can be determined by studying the angular distribution of the hyperons decay particles. As shown in section 3.1.1 this angular distribution is given by

$$I = \text{Tr}(T\rho_{\text{initial}}T^\dagger) \tag{3.24}$$

where T is the decay matrix. In this section decay matrices for hyperons with different spins will be given and the angular distributions will be derived first for one single decay and then for two successive decays.

3.1.3.1 spin 1/2 \rightarrow spin 1/2 spin 0

For a spin 1/2 hyperon decaying to a spin 1/2 baryon and pseudoscalar spin 0 meson, conservation of total spin implies that the final state can have angular momentum 0 or 1. The parity of the final state is given by $(-1)^{L+1}$, but since the decay is weak both the parity conserving P state and the parity violating S state are allowed. The elements of the decay matrix, denoted $T(1/2 \rightarrow 1/2 0)_{2m_{\text{bar}}2m_{\text{hyp}}}$, are built up by the S and P amplitudes and the corresponding Clebsch-Gordan coefficients and spherical harmonics

$$\begin{aligned}
T(1/2 \rightarrow 1/2 \ 0)_{11} &= T_s Y_0^0 + \frac{1}{\sqrt{3}} T_p Y_1^0 \\
T(1/2 \rightarrow 1/2 \ 0)_{-11} &= -\sqrt{\frac{2}{3}} T_p Y_1^1 \\
T(1/2 \rightarrow 1/2 \ 0)_{1-1} &= \sqrt{\frac{2}{3}} T_p Y_1^{-1} \\
T(1/2 \rightarrow 1/2 \ 0)_{-1-1} &= T_s Y_0^0 - \frac{1}{\sqrt{3}} T_p Y_1^0
\end{aligned} \tag{3.25}$$

or in matrix form with the explicit expressions for the spherical harmonics inserted

$$T(1/2 \rightarrow 1/2 \ 0) = \frac{1}{\sqrt{4\pi}} \begin{bmatrix} T_s + T_p \cos \Theta & T_p \sin \Theta e^{-i\phi} \\ T_p \sin \Theta e^{i\phi} & T_s - T_p \cos \Theta \end{bmatrix} . \tag{3.26}$$

However since $\text{Tr}(T\rho T^\dagger) = \text{Tr}(\rho T^\dagger T)$, the calculation of the angular distribution is simplified if the matrix $A = T^\dagger T$ is calculated as a first step

$$A(1/2 \rightarrow 1/2 \ 0) = \frac{1}{4\pi} \begin{bmatrix} 1 + \alpha \cos \Theta & \alpha \sin \Theta e^{-i\phi} \\ \alpha \sin \Theta e^{i\phi} & 1 - \alpha \cos \Theta \end{bmatrix} \tag{3.27}$$

where the asymmetry parameter α has been introduced. The asymmetry parameters are the following combinations of the S and P amplitudes

$$\begin{aligned}
\alpha &= 2\text{Re}(T_s^* T_p) \\
\beta &= 2\text{Im}(T_s^* T_p) \\
\gamma &= |T_s|^2 - |T_p|^2 .
\end{aligned} \tag{3.28}$$

They are numbers between -1 and 1, which has to be measured for each specific decay. By construction they fulfill $\alpha^2 + \beta^2 + \gamma^2 = |T_s|^2 + |T_p|^2 = 1$.

Finally, using the A matrix the angular distribution becomes

$$I(\Theta, \phi) = \text{Tr}(\rho(1/2)A(1/2 \rightarrow 1/2 \ 0)) = \frac{1}{4\pi} (1 + \alpha P_y \sin \Theta \sin \phi) \tag{3.29}$$

or expressed in Cartesian instead of spherical coordinates

$$I(\hat{k}) = \frac{1}{4\pi} (1 + \alpha P_y k_y) \tag{3.30}$$

where k is a unit vector pointing in the direction of the daughter baryon momentum, as defined in the previously introduced coordinate system, where the x - and z -axes form the production plane.

3.1.3.2 spin 3/2 \rightarrow spin 1/2 spin 0

For the spin 3/2 Ω hyperon decaying to a spin 1/2 Λ hyperon and a spin 0 kaon, conservation of total spin in this case implies that the final state can have angular momentum 1 or 2. The parity violating S state in the previous spin 1/2 case is here replaced by a D state. The same strategy as in eq.(3.25) can be used to write out the elements of the decay matrix

$$\begin{aligned}
T(3/2 \rightarrow 1/2 0)_{13} &= T_p Y_1^1 + \frac{1}{\sqrt{5}} T_d Y_2^1 \\
T(3/2 \rightarrow 1/2 0)_{-13} &= -\frac{2}{\sqrt{5}} T_d Y_2^2 \\
T(3/2 \rightarrow 1/2 0)_{11} &= \sqrt{\frac{2}{3}} T_p Y_1^0 + \sqrt{\frac{2}{5}} T_d Y_2^0 \\
T(3/2 \rightarrow 1/2 0)_{-11} &= \frac{1}{\sqrt{3}} T_p Y_1^1 - \sqrt{\frac{3}{5}} T_d Y_2^1 \\
T(3/2 \rightarrow 1/2 0)_{1-1} &= \frac{1}{\sqrt{3}} T_p Y_1^{-1} + \sqrt{\frac{3}{5}} T_d Y_2^{-1} \\
T(3/2 \rightarrow 1/2 0)_{-1-1} &= \sqrt{\frac{2}{3}} T_p Y_1^0 - \sqrt{\frac{2}{5}} T_d Y_2^0 \\
T(3/2 \rightarrow 1/2 0)_{1-3} &= \frac{2}{\sqrt{5}} T_d Y_2^{-2} \\
T(3/2 \rightarrow 1/2 0)_{-1-3} &= T_p Y_1^{-1} - \frac{1}{\sqrt{5}} T_d Y_2^{-1}
\end{aligned} \tag{3.31}$$

or in matrix form with the explicit expressions for the spherical harmonics inserted

$$\sqrt{8\pi} T(3/2 \rightarrow 1/2 0) = \begin{bmatrix} -\sqrt{3} \sin \Theta e^{i\phi} & 2T_p \cos \Theta + & \sin \Theta e^{-i\phi} & \sqrt{3} T_d \sin^2 \Theta e^{-2i\phi} \\ \times (T_p + T_d \cos \Theta) & +3T_d \cos^2 \Theta - T_d & \times (T_p + 3T_d \cos \Theta) & \\ \\ -\sqrt{3} T_d \sin^2 \Theta e^{2i\phi} & \sin \Theta e^{i\phi} & 2T_p \cos \Theta - & \sqrt{3} \sin \Theta e^{-i\phi} \\ & \times (-T_p + 3T_d \cos \Theta) & -3T_d \cos^2 \Theta + T_d & \times (T_p - T_d \cos \Theta) \end{bmatrix} . \tag{3.32}$$

For the Ω hyperon the asymmetry parameters can be defined in the same way as for the spin 1/2 hyperons by replacing the S amplitude with the D amplitude. It is an experimental fact that the α parameter is almost zero ($\alpha = 0.0175$ [95]) for the Ω hyperon. If α is put to zero the A matrix is very much simplified

$$A(3/2 \rightarrow 1/2 0) = \frac{1}{8\pi} \begin{bmatrix} 3 \sin^2 \Theta & -\sqrt{3} e^{i\phi} \sin 2\Theta & -\sqrt{3} e^{2i\phi} \sin^2 \Theta & 0 \\ -\sqrt{3} e^{-i\phi} \sin 2\Theta & 1 + 3 \cos^2 \Theta & 0 & -\sqrt{3} e^{2i\phi} \sin^2 \Theta \\ -\sqrt{3} e^{-2i\phi} \sin^2 \Theta & 0 & 1 + 3 \cos^2 \Theta & \sqrt{3} e^{i\phi} \sin 2\Theta \\ 0 & -\sqrt{3} e^{-2i\phi} \sin^2 \Theta & \sqrt{3} e^{-i\phi} \sin 2\Theta & 3 \sin^2 \Theta \end{bmatrix} \quad (3.33)$$

giving the angular distribution

$$\begin{aligned} I(\Theta, \phi) &= \text{Tr}(\rho(3/2)A(3/2 \rightarrow 1/2 0)) = \\ &= \frac{3}{4\pi}(\rho_{33}(1 - \cos^2 \Theta) + \rho_{11}(\frac{1}{3} + \cos^2 \Theta) - \frac{2}{\sqrt{3}}\text{Re}\rho_{3-1} \sin^2 \Theta \cos 2\phi \\ &\quad - \frac{2}{\sqrt{3}}\text{Re}\rho_{31} \sin 2\Theta \cos \phi) \quad . \end{aligned} \quad (3.34)$$

With the the explicit expressions for the density matrix elements inserted this becomes

$$\begin{aligned} I(\Theta, \phi) &= \frac{1}{4\pi} \left(1 + \frac{\sqrt{3}}{2} (1 - 3 \cos^2 \Theta) r_0^2 \right. \\ &\quad \left. - \frac{3}{2} \sin^2 \Theta \cos 2\phi r_2^2 + \frac{3}{2} \sin 2\Theta \cos \phi r_1^2 \right) \end{aligned} \quad (3.35)$$

or

$$I(\hat{k}) = \frac{1}{4\pi} \left(1 + \frac{\sqrt{3}}{2} (1 - 3k_z^2) r_0^2 - \frac{3}{2} (1 - k_z^2 - 2k_y^2) r_2^2 + 3k_x k_z r_1^2 \right) \quad (3.36)$$

where again the spherical coordinates are replaced by the \hat{k} vector. Thus, only three, r_2^2 , r_1^2 and r_0^2 , out of the seven non-zero coefficients are accessible,

the parameters r_n^3 and r_{-1}^1 are not. A similar expression is presented in [57], but without the explicit density matrix components inserted.

3.1.3.3 spin 1/2 \rightarrow spin 1/2 spin 0 \rightarrow spin 1/2 spin 0 spin 0

Some hyperons decay to states which also includes hyperons, *e.g.* Ξ^- decays to $\Lambda\pi^-$. In this case additional information can be obtained by also studying the angular distribution in the decay of the daughter hyperon. This angular distribution can, in principle, be calculated from the decay matrices of the two decays

$$I = \text{Tr}(T_2 T_1 \rho T_1^\dagger T_2^\dagger) = \text{Tr}(\rho T_1^\dagger A_2 T_1) \quad (3.37)$$

with the indices denoting the first and second decay. However, a rotation matrix R must be introduced to make the spins in the two decays defined with respect to the same axis. This is, of course, related to the angles, Θ_1 and ϕ_1 , of the first decay. The system should be rotated by an angle ϕ_1 around the z axis and then a rotation of $-\Theta_1$ around the y axis will make the spins defined with respect to the same axis;

$$R = e^{-i\frac{1}{2}\phi_1\sigma_z} e^{i\frac{1}{2}\Theta_1\sigma_y} e^{i\frac{1}{2}\phi_1\sigma_z} = \begin{bmatrix} \cos\frac{\Theta_1}{2} & \sin\frac{\Theta_1}{2}e^{-i\phi_1} \\ -\sin\frac{\Theta_1}{2}e^{i\phi_1} & \cos\frac{\Theta_1}{2} \end{bmatrix} . \quad (3.38)$$

To simplify the calculation, it is convenient to define a reference system where the spin of the initial hyperon defines the z -axis and the momentum of the daughter hyperon is in the xz plane, with $p_y = 0$ and $p_x > 0$. This means that $\phi_1 = 0$ and that the density matrix of the initial hyperon takes the form

$$\rho = \frac{1}{2} \begin{bmatrix} 1+P & 0 \\ 0 & 1-P \end{bmatrix} . \quad (3.39)$$

The angular distribution then takes the simple form

$$\begin{aligned} I(\Theta_1, \Theta_2, \phi_2) &= \text{Tr}(\rho T_1^\dagger R^\dagger A_2 R T_1) = \\ &= \frac{1}{16\pi^2} (1 + \alpha_1 P \cos \Theta_1 + \alpha_2 P \cos \Theta_1 \cos \Theta_2 + \alpha_1 \alpha_2 \cos \Theta_2 + \\ &+ \alpha_2 P \sin \Theta_1 \sin \Theta_2 (\beta_1 \sin \phi_2 - \gamma_1 \cos \phi_2)) . \end{aligned} \quad (3.40)$$

By integrating over the angles of the first decay one gets the angular distribution of the second decay according to

$$\begin{aligned}
I(\Theta_2, \phi_2) &= \int I(\Theta_1, \Theta_2, \phi_2) d\Omega_1 = \\
&= \frac{1}{4\pi} \left(1 + \alpha_1 \alpha_2 \cos \Theta_2 + \frac{\pi}{4} \alpha_2 P \sin \Theta_2 (\beta_1 \sin \phi_2 - \gamma_1 \cos \phi_2) \right)
\end{aligned} \tag{3.41}$$

or by introducing the vector \hat{k} (see section 3.1.3.1)

$$I(\hat{k}) = \frac{1}{4\pi} \left(1 + \alpha_1 \alpha_2 k_z + \frac{\pi}{4} \alpha_2 \beta_1 P k_y - \frac{\pi}{4} \alpha_2 \gamma_1 P k_x \right) . \tag{3.42}$$

This expression is the same as the one given in [60]. What is noticeable is that the asymmetry parameters β and γ which do not show up in the angular distribution of the first decay, appear in the expression for the angular distribution of the succeeding decay. The β parameter is important for CP-violation measurements, as presented in section 3.2.

3.1.3.4 spin 3/2 \rightarrow spin 1/2 spin 0 \rightarrow spin 1/2 spin 0 spin 0

Also the spin 3/2 Ω hyperon has a Λ daughter particle in its dominant decay, $\Omega \rightarrow \Lambda K$. The angular distribution of the Λ decay is calculated in the same way as eq.(3.40), by instead using the density matrix describing the spin 3/2 hyperon and the T matrices describing the spin 3/2 \rightarrow spin 1/2 spin 0 decay. It is in this case not possible to get such a simple density matrix as in eq.(3.39), by choosing the z axis in the direction of the spin of the Ω . The multiplication of all the matrices in eq.(3.40) will in this case give a very complicated result. However, if the simplification to put α for the Ω decay to zero, *i.e.* $\alpha_1 = 0$, is used and the angles of the first decay are integrated out, the result becomes

$$\begin{aligned}
I(\Theta_2, \phi_2) &= \\
&= \frac{1}{4\pi} (1 + \beta_1 \alpha_2 \left(\sqrt{\frac{3}{5}} r_{-1}^1 + \frac{3}{2\sqrt{10}} r_{-1}^3 \right) \sin \Theta_2 \cos \phi_2 + \\
&+ \gamma_1 \alpha_2 \left(\sqrt{\frac{3}{5}} r_{-1}^1 + \frac{3}{2\sqrt{10}} r_{-1}^3 \right) \sin \Theta_2 \sin \phi_2)
\end{aligned} \tag{3.43}$$

or as a function of \hat{k}

$$I(\hat{k}) = \frac{1}{4\pi} \left(1 + \left(\sqrt{\frac{3}{5}} r_{-1}^1 + \frac{3}{2\sqrt{10}} r_{-1}^3 \right) (\beta_1 \alpha_2 k_x + \gamma_1 \alpha_2 k_y) \right) . \tag{3.44}$$

It is now possible to identify what can be measured by studying this secondary decay. A linear combination of r_{-1}^1 and r_{-1}^3 shows up. Neither of those

can be measured from the first decay. The combination $\sqrt{\frac{3}{5}}r_{-1}^1 + \frac{3}{2\sqrt{10}}r_{-1}^3$ will consequently give additional input. Also the asymmetry parameters β and γ for the Ω hyperon are not known. If α is assumed to be zero, the sum of their squares must be one, which means that they can be written as $\beta = \sin \phi$ and $\gamma = \cos \phi$. The angle ϕ can in principle be determined from this angular distribution. It can also be noted that if α for the Ω hyperon is not put to zero, its only contribution to this angular distribution of the Λ decay is a term $\alpha_\Omega \alpha_\Lambda k_z$. This means that α_Ω can be measured in the z direction, which is not present in eq.(3.44).

A previous calculation of the $\Omega \rightarrow \Lambda K \rightarrow p\pi K$ decay chain exists [61], where a different strategy is used. According to this calculation one parameter of the vector polarisation can be extracted from a measurement of the decay angles in the $\Lambda \rightarrow p\pi$ decay in a certain direction. The angles of the $\Omega \rightarrow \Lambda K$ decay are not used to get additional information. In the method described in this thesis the angular distributions of both decays are used and also polarisation parameters which are not part of the vector polarisation can be extracted.

3.1.4 Spin Variables in the $\bar{p}p \rightarrow \bar{Y}Y$ Reaction

In the $\bar{p}p \rightarrow \bar{Y}Y$ reaction, not only the polarisations of the individual hyperons, but also the correlations of their spins, are accessible. The total angular distribution for both the hyperon decays is needed to measure these correlations. This section is a deduction of this angular distribution for spin 1/2 hyperons, which follows in large the one given in [62].

3.1.4.1 The Density Matrix for the Two Hyperons

The spins of the proton and the antiproton are uncorrelated in the initial state in the $\bar{p}p \rightarrow \bar{Y}Y$ process. Therefore, the density matrix for the initial state is just the outer product of their individual density matrices, with a normalisation factor of 4π for the solid angle,

$$\begin{aligned} \rho^{\bar{p}p} &= \frac{1}{4\pi} \frac{1}{4} (\mathcal{J} + \bar{P}^{\bar{p}} \cdot \bar{\sigma}^{\bar{p}}) \otimes (\mathcal{J} + \bar{P}^p \cdot \bar{\sigma}^p) = \\ &= \frac{1}{16\pi} \left(\mathcal{J} + \sum_{i=1}^3 P_i^{\bar{p}} \sigma_i^{\bar{p}} + \sum_{j=1}^3 P_j^p \sigma_j^p + \sum_{i,j=1}^3 P_i^{\bar{p}} P_j^p \sigma_i^{\bar{p}} \sigma_j^p \right) \end{aligned} \quad (3.45)$$

which can be compactified to

$$\rho^{\bar{p}p} = \frac{1}{16\pi} \sum_{i,j=0}^3 P_i^{\bar{p}} P_j^p \sigma_i^{\bar{p}} \sigma_j^p \quad (3.46)$$

if the convention to define $P_0 = 1$ and $\sigma_0 = \mathcal{I}$ is used. It is possible that the spins of the hyperons in the final state are correlated due to effects in their production mechanism. Consequently, it is not possible to write the density matrix as an outer product of the two separate density matrices. Instead, the density matrix of the initial state can be transformed into the density matrix of the final state. Let M be the operator that does this transformation. Then we have according to section 3.1.1

$$\rho^{\bar{Y}Y} = M\rho^{\bar{p}p}M^\dagger = \frac{1}{16\pi} \sum_{i,j=0}^3 P_i^{\bar{p}} P_j^p M \sigma_i^1 \sigma_j^2 M^\dagger \quad (3.47)$$

where the antiparticles are represented by σ^1 and the particles by σ^2 . To write the density matrix in a form which displays the spin variables more explicitly it is convenient to do an expansion using Pauli matrices. Since it is a 4×4 matrix, a base of 16 linearly independent matrices is needed. This is given by the outer product $\sigma_\mu^1 \sigma_\nu^2$, where the zeroth component is taken as the identity matrix as usual

$$\rho^{\bar{Y}Y} = \sum_{\mu,\nu=0}^3 x_{\mu\nu} \sigma_\mu^1 \sigma_\nu^2 \quad (3.48)$$

Using the properties of the Pauli matrices, $\sigma_i \sigma_j = \delta_{ij} + i\epsilon_{ijk} \sigma_k$ and $\text{Tr}(\sigma_i) = 0$, the coefficients in the expansion can be extracted by multiplying with the corresponding Pauli matrices and taking the trace

$$x_{\mu\nu} = \frac{1}{4} \text{Tr}(\sigma_\mu^1 \sigma_\nu^2 \rho^{\bar{Y}Y}) = \frac{1}{16\pi} \sum_{i,j=0}^3 P_i^{\bar{p}} P_j^p \frac{1}{4} \text{Tr}(\sigma_\mu^1 \sigma_\nu^2 M \sigma_i^1 \sigma_j^2 M^\dagger) \quad (3.49)$$

where the expression from eq.(3.47) has been inserted. The coefficients can in turn be inserted into eq.(3.48) to give

$$\rho^{\bar{Y}Y} = \frac{1}{16\pi} \sum_{\mu,\nu=0}^3 \sum_{i,j=0}^3 P_i^{\bar{p}} P_j^p \frac{1}{4} \text{Tr}(\sigma_\mu^1 \sigma_\nu^2 M \sigma_i^1 \sigma_j^2 M^\dagger) \sigma_\mu^1 \sigma_\nu^2 \quad (3.50)$$

By defining the spin variables, $\chi_{ij\mu\nu}$, and the differential cross section, $I_0^{\bar{Y}Y}$, as

$$\begin{aligned} \chi_{ij\mu\nu} &= \frac{\text{Tr}(\sigma_\mu^1 \sigma_\nu^2 M \sigma_i^1 \sigma_j^2 M^\dagger)}{\text{Tr}(MM^\dagger)} \\ I_0^{\bar{Y}Y} &= \frac{1}{4} \text{Tr}(MM^\dagger) \end{aligned} \quad (3.51)$$

the final form of the density matrix becomes

$$\rho^{\bar{Y}Y} = \frac{I_0^{\bar{Y}Y}}{16\pi} \sum_{\mu, \nu=0}^3 \sum_{i,j=0}^3 P_i^{\bar{P}} P_j^P \chi_{ij\mu\nu} \sigma_\mu^1 \sigma_\nu^2 \quad . \quad (3.52)$$

The indices i, j, μ, ν represents the antiproton beam, proton target, antihyperon and hyperon respectively.

3.1.4.2 Spin Variables in the Angular Distribution of the Decay Baryons

As shown in previous sections it is possible to deduce the polarisation, P , of hyperons from the angular distribution of their daughter baryons. In a similar way spin variables in the $\bar{p}p \rightarrow \bar{Y}Y$ process can be deduced from the angular distribution of both the decay baryon and antibaryon. Using the T matrices from section 3.1.3.1, the density matrix for the hyperons in eq.(3.52) can be transformed to the density matrix of the daughter baryons

$$\rho^{\bar{B}B} = T_{\bar{Y}} T_Y \rho^{\bar{Y}Y} T_{\bar{Y}}^\dagger T_Y^\dagger = \frac{I_0^{\bar{Y}Y}}{16\pi} \sum_{\mu, \nu=0}^3 \sum_{i,j=0}^3 P_i^{\bar{P}} P_j^P \chi_{ij\mu\nu} T_{\bar{Y}} T_Y \sigma_\mu^1 \sigma_\nu^2 T_{\bar{Y}}^\dagger T_Y^\dagger \quad (3.53)$$

and the angular distribution is achieved by taking the trace of this density matrix

$$I_0^{\bar{B}B} = \text{Tr}(\rho^{\bar{B}B}) = \frac{I_0^{\bar{Y}Y}}{16\pi} \sum_{\mu, \nu=0}^3 \sum_{i,j=0}^3 P_i^{\bar{P}} P_j^P \chi_{ij\mu\nu} \text{Tr}(T_{\bar{Y}} T_Y \sigma_\mu^1 \sigma_\nu^2 T_{\bar{Y}}^\dagger T_Y^\dagger) \quad . \quad (3.54)$$

Using the A matrix from eq.(3.27) it is straightforward to show that

$$\begin{aligned} \text{Tr}(T_Y \sigma_i T_Y^\dagger) &= \text{Tr}(\sigma_i A_Y) \\ &= \frac{2\alpha k_i}{4\pi} \end{aligned} \quad (3.55)$$

with $k_0 = \frac{1}{\alpha}$, which turns eq.(3.54) into

$$I_0^{\bar{B}B} = \frac{I_0^{\bar{Y}Y}}{64\pi^3} \sum_{\mu, \nu=0}^3 \sum_{i,j=0}^3 \bar{\alpha} \alpha P_i^{\bar{P}} P_j^P \chi_{ij\mu\nu} \bar{k}_\mu k_\nu \quad (3.56)$$

where the bar over α and k denotes the antiparticle. The 256 spin variables $\chi_{ij\mu\nu}$ are given in table 3.1, where I denotes differential cross section, A asymmetry, P polarisation, D depolarisation, K polarisation transfer, C spin correlation and M, N spin correlation tensor elements.

Polarised Particle	None	Beam	Target	Both
None	I_{0000}	A_{i000}	A_{0j00}	A_{ij00}
Scattered	$P_{00\mu 0}$	$D_{i0\mu 0}$	$K_{0j\mu 0}$	$M_{ij\mu 0}$
Recoil	$P_{000\nu}$	$K_{i00\nu}$	$D_{0j0\nu}$	$N_{ij0\nu}$
Both	$C_{00\mu\nu}$	$C_{i0\mu\nu}$	$C_{0j\mu\nu}$	$C_{ij\mu\nu}$

Table 3.1: Names of the 256 spin variables $\chi_{ij\mu\nu}$. The first row tells which of the initial particles are polarised and the first column which of the final particles are.

For PANDA both the beam and the target are unpolarised. This means that $i = j = 0$ and out of the original 256 spin variables only the 16 variables, the cross section, the polarisation $P_{\bar{Y},l} = \chi_{00l0}$, $P_{Y,l} = \chi_{000l}$ and the spin correlations $C_{lm} = \chi_{00lm}$ are accessible.

3.1.5 Hyperon Rest Systems and Symmetry Constraints on Spin Variables

By defining the two rest systems, shown in figure 3.1, with the y-axis as a pseudovector perpendicular to the production plane

$$\begin{aligned}
\hat{x} &= \hat{y} \times \hat{z} \\
\hat{y} &= \frac{\vec{p}_{\text{beam}} \times \vec{p}_{\bar{Y}}}{|\vec{p}_{\text{beam}} \times \vec{p}_{\bar{Y}}|} \\
\hat{z} &= \hat{p}_{\bar{Y}/Y}
\end{aligned} \tag{3.57}$$

maximum use of C and P invariance is obtained. As already seen in section 3.1.2.1, the parity invariance of the strong interaction means that $P_{\bar{Y},x} = P_{Y,x} = P_{\bar{Y},z} = P_{Y,z} = 0$. With this definition of the rest system, it is clear that \hat{y} is unaffected by a parity transformation, whereas \hat{x} and \hat{z} change sign. All spin variables with odd number of x and z must therefore be zero, so apart from the polarisations also $C_{xy} = C_{yx} = C_{yz} = C_{zy} = 0$. For PANDA, eq.(3.56) then reduces to

$$I_{BB}(\Theta_{\bar{Y}}, \hat{k}, \hat{k}) = \frac{I_0}{64\pi^3} \begin{pmatrix} 1 \\ +P_{\bar{Y},y}\bar{\alpha}\bar{k}_y + P_{Y,y}\alpha k_y \\ +C_{xx}\bar{\alpha}\alpha\bar{k}_x k_x \\ +C_{yy}\bar{\alpha}\alpha\bar{k}_y k_y \\ +C_{zz}\bar{\alpha}\alpha\bar{k}_z k_z \\ +C_{xz}\bar{\alpha}\alpha\bar{k}_x k_z \\ +C_{zx}\bar{\alpha}\alpha\bar{k}_z k_x \end{pmatrix} \tag{3.58}$$

Due to the rotational invariance of the $\bar{p}p \rightarrow \bar{Y}Y$ reaction, the relations $\chi_{ij\mu\nu} = \chi_{jiv\mu}$ hold. For the spin variables accessible for PANDA this means $P_{\bar{Y},y} = P_{Y,y}$ and $C_{xz} = C_{zx}$. Thus we are left with five measurable spin variables.

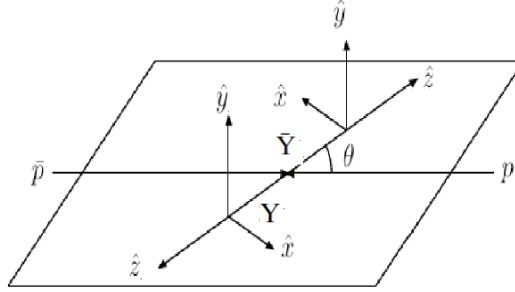


Figure 3.1: Definitions of the rest systems for \bar{Y} and Y in the $\bar{p}p \rightarrow \bar{Y}Y$ reaction.

For reactions where also the daughter particle is a weakly decaying hyperon, additional spin information can be obtained from the second decay, as shown previously. In this case the rest system for the daughter hyperon is defined through

$$\begin{aligned}\hat{x}_2 &= \hat{y}_2 \times \hat{z}_2 \\ \hat{y}_2 &= \frac{\hat{y} \times \bar{p}_{\bar{Y}_2}}{|\hat{y} \times \bar{p}_{\bar{Y}_2}|} \\ \hat{z}_2 &= \hat{p}_{\bar{Y}_2/Y_2}\end{aligned}\tag{3.59}$$

where \hat{y} is the pseudovector transverse to the production plane for the original hyperons.

3.1.6 Restrictions on Spin Variables from Theoretical Considerations

It should be noted that already before measurement some combinations of values of the spin variables can be excluded based on theoretical considerations. A thorough review of how the spin variables depend on each other is given in [63]. After the symmetry considerations, the non-zero spin variables can be

described by six independent complex amplitudes [64, 65, 66]. An empirical way to investigate how the spin variables depend on each other is to randomly generate the aforementioned amplitudes and then plot different spin variables against each other, to see which part of the plane the values populate. This has been done in [67, 68]. The result for the spin variables of interest for this thesis is summarised in table 3.2. Here, fs means that values covering the whole plane are allowed, for \bigcirc the values can only be within a circle of radius 1 centered at (0,0), while ∇ and \triangleleft denotes the triangles $|2 \cdot \text{SpinVariable}_1| \leq \text{SpinVariable}_2 + 1$ and $|2 \cdot \text{SpinVariable}_2| \leq \text{SpinVariable}_1 + 1$ respectively. In addition studies involving three spin variables have been made in the same way [69, 70], resulting in allowed volumes in the cube. As an example (P_y , C_{xz} , C_{yy}) are only allowed inside a cone and (C_{yy} , C_{zz} , C_{xx}) inside a tetrahedron. All these relations can of course be hard to keep track on, but a lot can be gained in doing so. For instance, the spin variable D_{yy} , which was important for discriminating between different theoretical models (see section 4.1), can only be measured using a polarised target. With a polarised target it was measured at LEAR to be close to zero, but this result could have been deduced from already existing data on other spin variables.

C_{xx}	C_{yy}	C_{zz}	C_{xz}	
\bigcirc	\triangleleft	\bigcirc	\bigcirc	P_y
	fs	fs	\bigcirc	C_{xx}
		fs	∇	C_{yy}
			\bigcirc	C_{zz}

Table 3.2: Domain of square which is allowed for pairs of spin variables.

Also for the polarisation variables of the Ω hyperon, theoretical restrictions can be deduced from constraints that the density matrix has to fulfill. In particular the relation $\rho_{ii}\rho_{jj} \geq |\rho_{jj}|^2$ [71] gives rise to the following inequalities

$$\begin{aligned}
(r_0^2)^2 + (r_2^2)^2 + (r_{-2}^3)^2 &\leq \frac{1}{3} \\
(r_0^2)^2 + (r_1^2)^2 + \frac{5}{3}(r_{-1}^1)^2 &\leq \frac{1}{3} \\
6(r_{-3}^3)^2 &\leq (1 + \sqrt{3}r_0^2)^2 \\
\frac{12}{5}(r_{-1}^1)^2 + \frac{18}{5}(r_{-1}^3)^2 &\leq (1 - \sqrt{3}r_0^2)^2
\end{aligned} \tag{3.60}$$

where for instance the first two can be used to put a limit on r_{-2}^3 and r_{-1}^1 , if r_0^2 , r_1^2 and r_2^2 are measured from the angular distribution of the decay Λ hyperon. In fact, using the inequalities and measured values, limits can be put on all seven of the non-zero polarisation parameters.

3.2 CP Violation Parameters

CP violation can be studied in a very clean way in the $\bar{p}p \rightarrow \bar{Y}Y$ process. Since the initial state is a CP eigenstate, the antihyperon hyperon pair of the final state has the same symmetry and therefore no hadronic final state interactions can give rise to a false signal. Also, baryon number conservation guarantees that there is no mixing between the antihyperon and the hyperon. It is possible to define a few CP violation parameters for $\bar{p}p \rightarrow \bar{Y}Y$, for which a non-zero measurement would be a clear proof of CP violation [72]. As seen previously, the asymmetry parameter α quantifies the tendency of the decay baryon to be preferably emitted in the hyperon spin direction. Charge conjugation turns the hyperon into the corresponding antihyperon and a parity transformation rotates the emission direction by 180° . If CP is conserved, the relation $\alpha = -\bar{\alpha}$ therefore holds, so that the following parameter should be zero

$$A = \frac{\Gamma\alpha + \bar{\Gamma}\bar{\alpha}}{\Gamma\alpha - \bar{\Gamma}\bar{\alpha}} \simeq \frac{\alpha + \bar{\alpha}}{\alpha - \bar{\alpha}} \quad (3.61)$$

where Γ is the partial width for the decay. Some hyperons decay to new hyperons which in turn also decays weakly in a two-step process. In this case, also the parameter β is accessible from the second decay. Also for β CP conservation means $\beta = -\bar{\beta}$, so that the following CP violation parameters can be formed

$$\begin{aligned} B &= \frac{\Gamma\beta + \bar{\Gamma}\bar{\beta}}{\Gamma\beta - \bar{\Gamma}\bar{\beta}} \simeq \frac{\beta + \bar{\beta}}{\beta - \bar{\beta}} \\ B' &= \frac{\Gamma\beta + \bar{\Gamma}\bar{\beta}}{\Gamma\alpha - \bar{\Gamma}\bar{\alpha}} \simeq \frac{\beta + \bar{\beta}}{\alpha - \bar{\alpha}} \end{aligned} \quad (3.62)$$

CP violation can only occur when amplitudes with different phases mix. In the case of the CP violation parameters defined through asymmetry parameters, it is the S- and P-wave amplitudes of the decay which mix [28, 73, 29]. Another CP violation parameter is for partial widths, which should be the same for the CP conjugate decays $Y \rightarrow B\pi$ and $\bar{Y} \rightarrow \bar{B}\pi$ [74]. The amplitudes which mix are here instead between the different isospin transitions¹ $\Delta I = 1/2$ and $\Delta I = 3/2$. The parameter which should be zero can be defined through

$$D = \frac{\Gamma - \bar{\Gamma}}{\Gamma + \bar{\Gamma}} \quad (3.63)$$

¹ D is consequently only a CP violation parameter for hyperon decays where different isospin transitions are possible. As an example the decay $\Xi^- \rightarrow \Lambda\pi^-$ has only a $\Delta I = 1/2$ transition and D is not a CP violation parameter in this case.

From theoretical considerations [29], the order of magnitude of the different CP violation parameters can be ordered in the following way

$$0.1O(B) \approx O(B') \approx 10O(A) \approx 100O(D) \quad . \quad (3.64)$$

The parameter D is probably too small to be accessible. The A parameter has the advantage that it can be measured for all hyperons, while the more sensitive B and B' parameters can only be measured for hyperons which have new hyperons as daughter particles. Since a large amount of statistics is needed for CP violation measurements the interesting reactions are mainly $\bar{p}p \rightarrow \bar{\Lambda}\Lambda$ for A and $\bar{p}p \rightarrow \bar{\Xi}^+\Xi^-$ for B and B' . Unfortunately Ξ^- has a very low β value of approximately -0.04, which means that it is difficult to measure B due to the $\beta - \bar{\beta}$ in the denominator. The somewhat less sensitive B' parameter is therefore the preferred choice to study.

4. Existing Data and Theoretical Predictions

Most of the high quality data for the $\bar{p}p \rightarrow \bar{Y}Y$ reaction comes from the PS185 experiment at LEAR, which was a fixed target experiment that took data up to 2 GeV/c beam momentum. The highest amount of statistics is 40k events for the $\bar{p}p \rightarrow \bar{\Lambda}\Lambda$ reaction at 1.64 GeV/c, where both the $\bar{\Lambda}$ and Λ hyperon were reconstructed [75]. There is a comparable amount of events at 6 GeV/c, but most often with just one of the hyperons reconstructed [76]. Otherwise, the experimental information in the region above 2 GeV/c comes mostly from bubble chamber experiments with low statistics (a handful of events at most). A compilation of these is given in [77]. The experimental situation for the cross section measurements is summarised in figure 4.1.

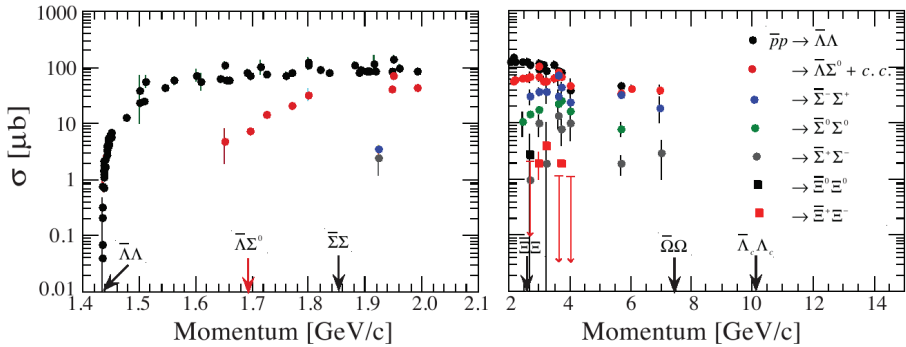


Figure 4.1: Experimental cross sections for the $\bar{p}p \rightarrow \bar{Y}Y$ reactions as a function of the beam momentum [78]. Thresholds for different processes are indicated on the beam momentum axis. The momentum region below 2.1 GeV/c is expanded in the left figure.

Almost all the data points in figure 4.1 are for the single strangeness hyperons Λ and Σ . The datapoints for the double strangeness Ξ hyperon production are from bubble chamber experiments where only total cross section (and sometimes only upper limits) were measured from a few events [79, 80]. The thresholds for different $\bar{p}p \rightarrow \bar{Y}Y$ channels are noted on the beam momentum axis. As seen, apart from the $\bar{p}p \rightarrow \bar{\Xi}^+\Xi^-$ also the triple strangeness $\bar{p}p \rightarrow \bar{\Omega}^+\Omega^-$ channel and the charmed $\bar{p}p \rightarrow \bar{\Lambda}_c^-\Lambda_c^+$ channel are well within reach for PANDA with a maximum beam momentum of 15 GeV/c. These are

the channels which this thesis is focused on. The first part of this chapter describes what is known about antihyperon hyperon physics from experimental and theoretical studies. The second part focuses on the $\bar{p}p \rightarrow \bar{Y}Y$ channels which will be studied for the first time with PANDA. The third part deals with theoretical predictions and existing experimental limits on hyperon CP violation parameters.

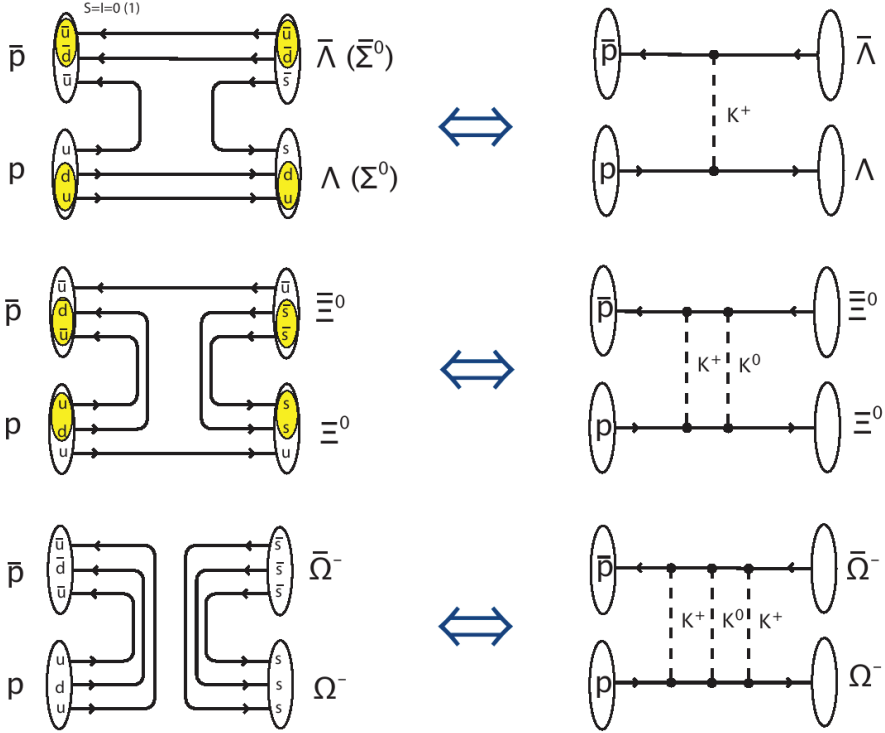


Figure 4.2: The $\bar{p}p \rightarrow \bar{Y}Y$ process for single, double and triple strangeness hyperons, seen in the quark line (left) and meson exchange (right) picture [78].

4.1 Prior Knowledge on the $\bar{p}p \rightarrow \bar{Y}Y$ Reaction

The creation of antihyperon hyperon pairs in antiproton proton collisions takes place at momentum transfers where the relevant degrees of freedom to describe the process can be discussed. The low energy nuclear physics approach is to use the exchange of mesons. This was the method that was first used historically. Calculations for nucleon nucleon scattering could be adjusted to the hyperon sector by introducing the exchange of kaons with strangeness instead of non-strange mesons [81, 82, 83, 84, 85]. Different calculations include dif-

ferent combinations of K , K^* and K^{**} mesons. Later also calculations using an approach with constituent quarks and gluons as degrees of freedom were made [82, 86, 87, 88, 89]. Here the process is seen as annihilation of light $q\bar{q}$ pairs and creation of $s\bar{s}$ pairs. The remaining light quarks are treated as spectators. Here, the transition from $q\bar{q}$ to $s\bar{s}$ is mediated by gluon exchange with quantum numbers 3S_1 or 3P_0 . The former corresponds to a single gluon exchange, whereas the latter to a two gluon exchange. The production of single, double and triple strangeness hyperons are sketched in figure 4.2, seen in the meson exchange picture and as quark line diagrams.

In the calculations for $\bar{p}p \rightarrow \bar{Y}Y$ reactions it is very important to include initial and final state interactions. The same strategy to do this is used for both pictures. The initial state $\bar{p}p$ interaction is described by a one-boson-exchange potential combined with a short range potential for the annihilation which is adjusted to fit antinucleon-nucleon, $\bar{N}N$, data. The unknown $\bar{Y}Y$ final state interaction is also described using a one-boson-exchange potential, in this case combined with a short range potential which is parametrized to fit hyperon production data. The calculations differ in the mesons included and coupling constants in the one-boson-exchange potentials and the strengths, ranges and number of terms in the short range potentials. The parameters for the initial state interactions can be fixed using $\bar{N}N$ data. The parameters of the final state interactions, on the other hand, are free parameters used to fit the data.

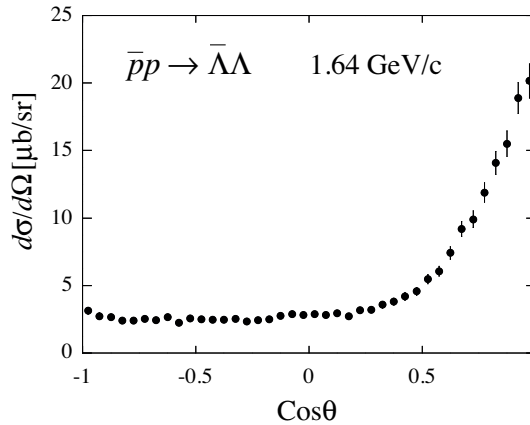


Figure 4.3: Differential cross section for $\bar{p}p \rightarrow \bar{\Lambda}\Lambda$ at 1.64 GeV/c beam momentum, measured by the PS185 experiment [75].

The high statistics of the PS185 experiment allowed for measurements of differential cross sections and the spin variables described in chapter 3 [75]. The differential cross section and polarisation for $\bar{p}p \rightarrow \bar{\Lambda}\Lambda$ at 1.64 GeV/c

is shown in figure 4.3 and figure 4.4, respectively. A lot of data were now available to test the calculations made from meson exchange and quark-gluon models. Two surprising experimental observations stood out. The first one was the appearance of a forward peaking of the differential cross section already very close to threshold, which indicates that the contribution of P-waves was important already at this low beam momentum. An explanation for this is a suppression of the S-wave from final-state interactions [82].

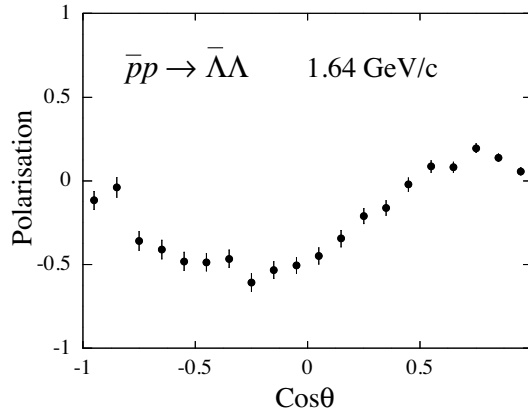


Figure 4.4: Polarisation as a function of $\bar{\Lambda}$ production angle for $\bar{p}p \rightarrow \bar{\Lambda}\Lambda$ at 1.64 GeV/c beam momentum, measured by the PS185 experiment [75].

The other result which stood out has to do with spins of the $\bar{\Lambda}\Lambda$ pair. The non-zero spin correlations were reconstructed from the data, shown in figure 4.1. From these spin correlations it is possible to calculate the singlet fraction

$$SF = \frac{1}{4}(1 + C_{xx} - C_{yy} + C_{zz}) \quad . \quad (4.1)$$

If this quantity is measured to be 1, the conclusion would be that the $\bar{\Lambda}\Lambda$ pair were produced in a singlet state. Correspondingly, a measurement of 0 would mean that the $\bar{\Lambda}\Lambda$ pair were always produced in a triplet state. If the spins are completely uncorrelated the measurement would give 0.25. As seen in figure 4.6 the data from PS185 showed that the $\bar{\Lambda}\Lambda$ pair are in a triplet state for all beam momenta up to 2 GeV/c. Since the Λ hyperon can be viewed as a spin 0 ud diquark together with an s quark, this observation can be related directly to the spins of the $s\bar{s}$ pair, which are then also produced in a triplet state.

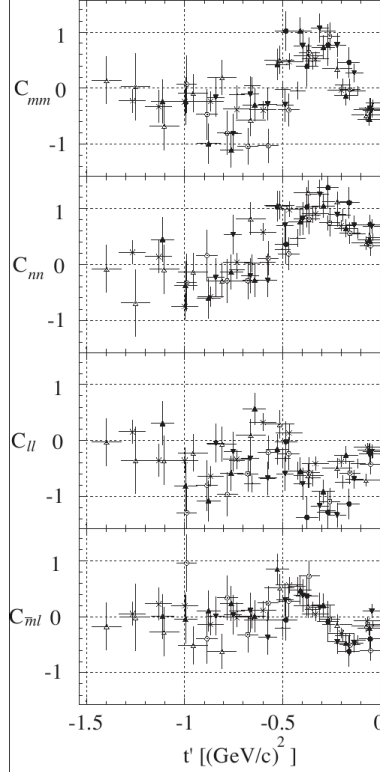


Figure 4.5: Spin correlations as a function of the reduced four-momentum transfers measured by the PS185 experiment [78].

It could be argued that neither meson exchange nor quark gluon models are appropriate to describe $\bar{p}p \rightarrow \bar{Y}Y$. The meson exchange models have problems with processes involving large momentum transfers, while hadronic effects may mean that the use of quarks and gluons is too simplified. However, calculations made in both meson exchange and quark gluon models seem to describe the PS185 data reasonably well. An example of a comparison of different theoretical predictions to data is shown in figure 4.7. A review of the situation from both theoretical and experimental side is given in [90]. Although they differ greatly in the way to describe the process no clear conclusion can be drawn from the data which approach is the better.

Model-independent analyses of the PS185 data have been performed. A partial-wave amplitude analyses of the data near threshold, using only partial waves with $L < 2$ and 3D_1 , was presented in [91]. The data was reasonably well described very near threshold. From these studies the conclusion was drawn that the dominance of the P-wave contribution over the S-wave contribution near threshold was to some extent just due to the endothermic nature of the $\bar{p}p \rightarrow \bar{Y}Y$ reaction. This means that the demand for the meson exchange

and quark-gluon pictures to find an explanation for the S-wave suppression is somewhat relaxed.

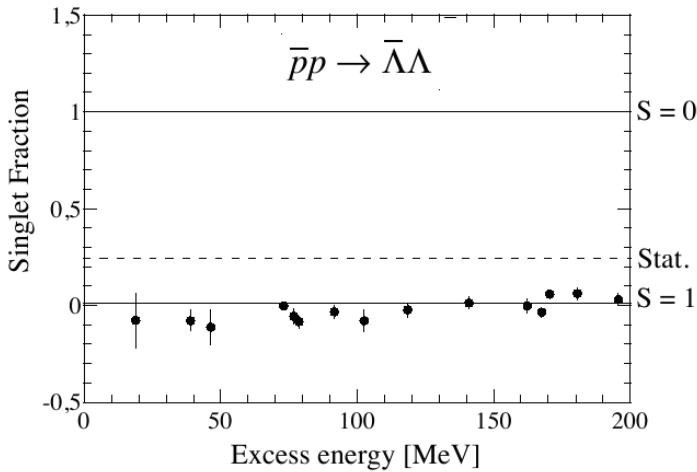


Figure 4.6: Singlet fractions for different excess energies measured by the PS185 experiment [78]. 200 MeV/ excess energy corresponds to a beam momentum of 2 GeV/c.

A main difference between the two pictures is how they explain why the $\bar{\Lambda}\Lambda$ pairs are always produced in a triplet state. In the meson exchange picture, this is caused by a strong tensor force and consequently a spin flip between the initial $\bar{p}p$ state and the final $\bar{\Lambda}\Lambda$ state. In the quark gluon picture the quantum numbers of the exchange allows only for a triplet state of $\bar{\Lambda}\Lambda$, and no tensor force (and hence no spin flip) is needed¹. It was therefore hoped that a measurement of the spin transfer observables D (depolarisation) and K (polarisation transfer), defined in section 3.1.4.2, using a polarised target would help to discriminate between the two pictures. The existence of a large spin flip would give negative values of D and K , while no spin flip would give positive values. The measurement was made and the values of D and K were found to be non-conclusive for the discrimination between the two pictures [93]. The question of how to describe the $\bar{p}p \rightarrow \bar{Y}Y$ reaction remains essentially open, and the upcoming data from PANDA will be very useful to make progress.

¹It has also been suggested that the $\bar{p}p \rightarrow \bar{Y}Y$ reaction can occur via an annihilation of the $\bar{u}u$ quarks and a "shake-out" of a polarised $\bar{s}s$ pair from the proton [92]. The proton has a non-zero strange quark contribution which is polarised opposite to the spin of the proton. This model can account for the dominance of the triplet state of the $\bar{\Lambda}\Lambda$ pairs and also predicts negative values for the spin transfer observables.

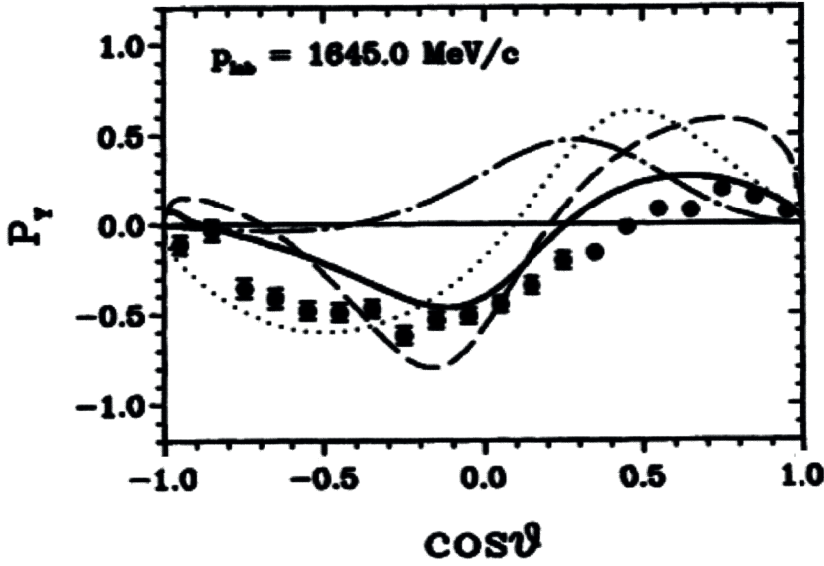


Figure 4.7: Theoretical predictions compared to data for polarisation of the Λ hyperon in the $\bar{p}p \rightarrow \bar{\Lambda}\Lambda$ reaction at 1.645 GeV/c beam momentum. The solid and dashed lines are obtained from the meson exchange picture, whereas the dashed-dotted and dotted lines are from quark-gluon models [90].

4.2 Hyperon Channels for This Thesis

The properties of the hyperons accessible to PANDA are summarised in table 4.1. The purpose of the simulations in this thesis is to investigate how well multistrange and charmed $\bar{p}p \rightarrow \bar{Y}Y$ channels can be measured with PANDA. In many cases this will constitute the first measurement. For simulations of the single strangeness channels at different beam momenta was covered in a previous thesis [94].

4.2.1 The $\bar{p}p \rightarrow \bar{\Xi}^+\Xi^-$ Reaction

The reaction $\bar{p}p \rightarrow \bar{\Xi}^+\Xi^-$ involves the creation of two $\bar{s}s$ pairs in the quark gluon picture or the exchange of two kaons in the hadronic picture. Ξ^- decays almost exclusively to $\Lambda\pi^-$ and the dominant decay mode for Λ is to $p\pi^-$, with a branching ratio of 0.64. A drawing of such a reaction is given in figure 4.8. The existing data for this reaction consists of bubble chamber measurements of the total cross section with a handful of events in total [79, 80]. PANDA is capable of increasing the statistics dramatically and give access to differential cross sections and spin variables. Due to the lack of experimental data there are not as many theoretical calculations of the $\bar{p}p \rightarrow \bar{\Xi}^+\Xi^-$ reac-

Hyperon	Quarks	Mass [MeV c^2]	$c\tau$ [cm]	Main decay	B [%]	α_γ
Λ	uds	1116	8.0	$p\pi^-$	64	+0.64
Σ^+	uus	1189	2.4	$p\pi^0$	52	-0.98
Σ^0	uds	1193	$2.2 \cdot 10^{-9}$	$\Lambda\gamma$	100	-
Σ^-	dds	1197	2.4	$n\pi^-$	100	-0.07
Ξ^0	uss	1315	8.7	$\Lambda\pi^0$	99	-0.41
Ξ^-	dss	1321	4.9	$\Lambda\pi^-$	100	-0.46
Ω^-	sss	1672	2.5	ΛK^-	68	-0.03
Λ_c^+	udc	2286	$6.0 \cdot 10^{-3}$	$\Lambda\pi^+$	1	-0.91(15)
Σ_c^{++}	uuc	2454		$\Lambda_c^+\pi^+$	100	
Σ_c^+	udc	2453		$\Lambda_c^+\pi^0$	100	
Σ_c^0	ddc	2454		$\Lambda_c^+\pi^-$	100	
Ξ_c^+	usc	2468	$1.2 \cdot 10^{-2}$	$\Xi^- \pi^+ \pi^+$	seen	
Ξ_c^0	dsc	2471	$2.9 \cdot 10^{-3}$	$\Xi^- \pi^+$	seen	-0.6(4)
Ω_c^0	ssc	2697	$1.9 \cdot 10^{-3}$	$\Omega^- \pi^+$	seen	

Table 4.1: *Properties of hyperons energetically accessible for PANDA [95].*

tion, as compared to $\bar{p}p \rightarrow \bar{\Lambda}\Lambda$. There are, however, some calculations, both in the meson exchange picture [96] and in the quark gluon picture [97, 98, 99]. The change in strangeness by two units instead of one means that the interaction process takes place at a shorter distance, which makes the process more suitable to study the relevance of quark and gluon degrees of freedom. It will therefore be very interesting to compare this process to $\bar{p}p \rightarrow \bar{\Lambda}\Lambda$.

The differential cross section is expected to be flatter than for $\bar{p}p \rightarrow \bar{\Lambda}\Lambda$, since in this case two of the quarks are annihilated and only one then could acts as a spectator. In fact, one theoretical calculation in the meson exchange picture [96] predicts the differential cross section for $\bar{p}p \rightarrow \bar{\Xi}^+\Xi^-$ to be almost isotropic.

Concerning spin variables, it will be interesting to see how the $\bar{p}p \rightarrow \bar{\Xi}^+\Xi^-$ data compares to the $\bar{p}p \rightarrow \bar{\Lambda}\Lambda$ data, with respect to the fact that the $\bar{\Lambda}\Lambda$ pairs are practically always produced in a triplet state. In a quark-diquark picture, the triplet state of the $\bar{\Lambda}\Lambda$ pairs can be interpreted in such a way that the $\bar{s}s$ pairs are produced in a triplet state. The $\bar{p}p \rightarrow \bar{\Xi}^0\Xi^0$ channel corresponds to annihilation of the spin zero diquarks and would therefore be very interesting to compare with. This channel is however hard to reconstruct due to the π^0 in the final state. In the more easily reconstructable double strangeness channel $\bar{p}p \rightarrow \bar{\Xi}^+\Xi^-$ instead the two d quarks are annihilated.

Another interesting comparison will be of the cross section, which relates to the OZI-rule and its possible violations. The OZI rule [100, 101, 102] describes the suppression of cross section for processes with disconnected quark

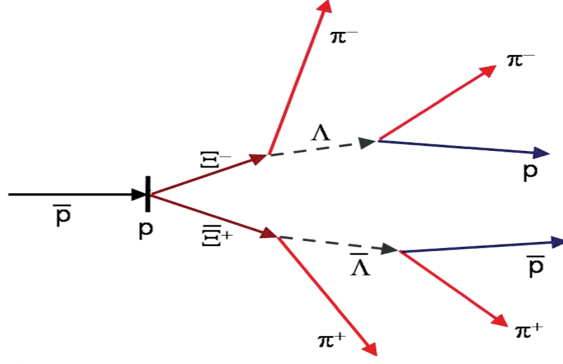


Figure 4.8: Schematic view of the reaction $\bar{p}p \rightarrow \bar{\Xi}^+\Xi^- \rightarrow \bar{\Lambda}\pi^+\Lambda\pi^- \rightarrow \bar{p}\pi^+\pi^+\pi^-\pi^-$.

lines. It has mostly been used for processes involving mesons, but can also be applied to hyperons [103]. The process $\bar{p}p \rightarrow \bar{\Xi}^+\Xi^-$ has one more disconnected quark line compared to $\bar{p}p \rightarrow \bar{\Lambda}\Lambda$, and one less than $\bar{p}p \rightarrow \bar{\Omega}^+\Omega^-$. Precise measurements of the cross sections of the three processes would give insight into the OZI rule for hyperons.

As an additional feature Ξ^- decays to $\Lambda\pi^-$, where Λ also decays weakly. In section 3.1.3.3 describing the subsequent decays of particles with spin $(\frac{1}{2}) \rightarrow (\frac{1}{2})(0) \rightarrow (\frac{1}{2})(0)(0)$, we saw that the decay parameters β and γ then shows up in the decay distribution of the daughter Λ . As described in section 3.2 it is possible to form a more sensitive CP violation parameter from β , than the one formed from α . For this reason $\bar{p}p \rightarrow \bar{\Xi}^+\Xi^-$ is very interesting for CP violation studies.

4.2.2 The $\bar{p}p \rightarrow \bar{\Omega}^+\Omega^-$ Reaction

No data exists for the $\bar{p}p \rightarrow \bar{\Omega}^+\Omega^-$ reaction. The only existing theoretical calculation predicts the maximum cross section to be about 2 nb [104]. It should be noted that this prediction is very low. The cross section for $\bar{p}p \rightarrow \bar{\Xi}^+\Xi^-$ is about 1/30 of the cross section for $\bar{p}p \rightarrow \bar{\Lambda}\Lambda$. If the same relation holds between the cross sections for $\bar{p}p \rightarrow \bar{\Xi}^+\Xi^-$ and $\bar{p}p \rightarrow \bar{\Omega}^+\Omega^-$, the cross section for $\bar{p}p \rightarrow \bar{\Omega}^+\Omega^-$ would instead be about 60 nb. The two main decays of Ω^- is to ΛK^- , with a branching ratio of 0.68 and to $\Xi^0\pi^-$, with a branching ratio of 0.24 [95]. Again, Ξ^0 is hard to reconstruct due to the π^0 in the final state, so

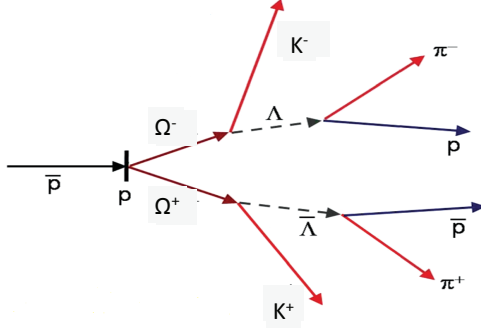


Figure 4.9: Schematic view of the reaction $\bar{p}p \rightarrow \bar{\Omega}^+\Omega^- \rightarrow \bar{\Lambda}K^+\Lambda K^- \rightarrow \bar{p}\pi^+K^+p\pi^-K^-$.

the decay studied is the one to ΛK^- . With this decay the full interaction chain is sketched in figure 4.9.

In the $\bar{p}p \rightarrow \bar{\Omega}^+\Omega^-$ reactions all of the quarks of the initial $\bar{q}q$ pairs of the initial $\bar{p}p$ system are annihilated, and three $\bar{s}s$ pairs are created. Since there are no spectator quarks that carry on the momentum of the initial antiprotons, it will be interesting to see if the differential cross section is completely isotropic or if there is some other mechanism for making it forward peaked.

The Ω^- hyperon has spin 3/2. The description of polarisation for spin 3/2 particles is much more complex as for spin 1/2 particles, with 15 polarisation parameters instead of the 3 from ordinary vector polarisation. Since the $\bar{\Omega}^+\Omega^-$ pair is created via the strong interaction, parity conservation can be used to show that 8 of these parameters are zero. As showed in section 3.1.3.2, three of the remaining polarisation parameters can be extracted from the angular distribution of the $\Omega^- \rightarrow \Lambda K^-$ decay. In the subsequent $\Lambda \rightarrow p\pi^-$ decay, a linear combination of two other shows up. Also appearing in this angular distribution are the two asymmetry parameters β and γ , which have never been measured for the Ω^- hyperon. In principle, all these parameters can be deduced by measuring the angular distributions of the two decays.

The $\bar{p}p \rightarrow \phi\phi\phi$ reaction is similar to the $\bar{p}p \rightarrow \bar{\Omega}^+\Omega^-$ reaction, in the sense that all quarks of the initial $\bar{p}p$ pair are annihilated and three $\bar{s}s$ pairs are created. In the $\bar{p}p \rightarrow \phi\phi\phi$ reaction, however, the $\bar{s}s$ pairs forms the ϕ mesons, whereas in the $\bar{p}p \rightarrow \bar{\Omega}^+\Omega^-$ reaction the three s quarks form the Ω^- hyperon and the three \bar{s} quarks form the $\bar{\Omega}^+$ hyperon. A comparison of the two reac-

tions can therefore give insight into the role of how the quarks are structured into hadrons.

4.2.3 The $\bar{p}p \rightarrow \bar{\Lambda}_c^- \Lambda_c^+$ Reaction

The $\bar{p}p \rightarrow \bar{\Lambda}_c^- \Lambda_c^+$ reaction is very similar to $\bar{p}p \rightarrow \bar{\Lambda} \Lambda$, with the difference that the s quarks are replaced by c quarks. A comparison between the production mechanisms of strangeness and charm can be made by comparing these two channels. The creation of $\bar{c}c$ pairs involves much higher momentum transfer and is therefore much less probable, so the cross section for $\bar{p}p \rightarrow \bar{\Lambda}_c^- \Lambda_c^+$ will be much lower. Also for this reaction there is no experimental data, but the theoretical estimates of the cross section that exist predict cross sections in the range from 10 to 100 nb [104, 105, 106, 107, 108]. A difficulty with the charmed channel is that the Λ_c^+ hyperon has very many decay modes, none of which has a branching ratio of more than a few per cent. The decay which is interesting for analysing spin variables is to $\Lambda\pi^+$, with a branching ratio of 1%. On the other hand, a promising feature of Λ_c^+ is the large value, -0.91, of the asymmetry parameter α , which means that the polarisation can be reconstructed from relatively few events.

4.3 CP Violation

The theoretical predictions within the Standard model for the values of CP violation parameters in hyperon decays, see section 3.2 for definitions, are typically of the order 10^{-5} to 10^{-4} . Early calculations from the eighties [29] give $A_\Lambda = -5 \cdot 10^{-5}$, $A_\Xi = -7 \cdot 10^{-5}$ and $B_\Xi = 8.4 \cdot 10^{-4}$. A more recent calculation using Chiral Perturbation Theory [109] gives $-3 \cdot 10^{-5} \leq A_\Lambda \leq 4 \cdot 10^{-5}$ and $-2 \cdot 10^{-5} \leq A_\Xi \leq 1 \cdot 10^{-5}$. As seen, the predicted values within the standard model are small. If physics beyond the standard model is introduced, larger values can be obtained. For example, predictions from calculations using supersymmetry give values in the order of 10^{-3} for A_Λ [26]. A measurement of a non-zero value of a hyperon CP violation variable would therefore not only be the first detection of CP violation in baryon systems, but possibly also give information on physics beyond the standard model. The observed CP violations in decays of neutral kaons [18, 19, 20] and B mesons [21, 22] are to a large extent consistent with the standard model, even though one measurement could be a hint of new physics [110].

The experimental search for CP violation in hyperon decays started in the middle of the nineties, but has only recently reached the precision necessary to test the predictions. The chronological progression of the measured values of CP violation parameters is shown in figure 4.10. The first measurement of a hyperon CP violation variable was from PS185, which found $A_\Lambda = -0.013 \pm 0.022$ [75, 111]. The limits on CP violation of Ξ decays comes

from experiments were the decays of are measured separately. The measured CP violation in these experiments is

$$A_{\Xi\Lambda} = \frac{\alpha_{\Xi}\alpha_{\Lambda} - \bar{\alpha}_{\Xi}\bar{\alpha}_{\Lambda}}{\alpha_{\Xi}\alpha_{\Lambda} + \bar{\alpha}_{\Xi}\bar{\alpha}_{\Lambda}} \approx A_{\Xi} + A_{\Lambda} . \quad (4.2)$$

In 2000, the E756 collaboration at Fermilab found $A_{\Xi\Lambda} = 0.012 \pm 0.014$ [112]. In 2004 the HyperCP collaboration, also at Fermilab, presented a 20 times more precise result, $A_{\Xi\Lambda} = [0.0 \pm 5.1(\text{stat}) \pm 4.4(\text{syst})] \cdot 10^{-4}$ [113]. This result, however, only used 17% of their data sample. In 2009 they presented the value obtained from their full dataset of over 10^9 events, resulting in the first measurement of CP violation parameter where zero is not within the error limits: $A_{\Xi\Lambda} = [-6.0 \pm 2.1(\text{stat}) \pm 2.0(\text{syst})] \cdot 10^{-4}$ [114]. No measurement exists for the B parameter.

Using data from PANDA, new measurements on A_{Λ} , A_{Ξ} and B_{Ξ} can be obtained. This will be discussed in section 6.5.

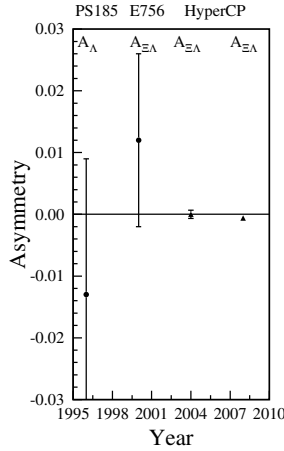


Figure 4.10: Chronological progression of measured values of hyperon CP violation parameters [114].

5. Analysis Methods

This chapter describes the methods used for reconstructing hyperon spin variables once the decay angles of the daughter baryons have been measured. With the angular distributions calculated in chapter 3 as starting points, expressions relating spin variables to expectation values of the angles are deduced for both spin 1/2 hyperons and the spin 3/2 Ω hyperon. Since the detector acceptance is different for different decay angles, the experimentally measured expectation values will not be the true ones. Two different ways to deal with this problem are presented. In the last part of the chapter the CP violation parameters are related to up down counting asymmetries which are more suitable as experimental observables.

5.1 Spin Variables for the Spin 1/2 Hyperons

It is straightforward to calculate the spin variables from the angles of the hyperon decay particles. To find expressions for the spin variables it is a good starting point to calculate the following expectation values

$$\begin{aligned}\langle \bar{k}_y \rangle &= \int_{-1}^1 \int_{-1}^1 \bar{k}_y I(\hat{k}, \hat{k}) d\bar{k}_y dk_y \\ \langle k_y \rangle &= \int_{-1}^1 \int_{-1}^1 k_y I(\hat{k}, \hat{k}) d\bar{k}_y dk_y \\ \langle \bar{k}_i k_j \rangle &= \int_{-1}^1 \int_{-1}^1 \bar{k}_i k_j I(\hat{k}, \hat{k}) d\bar{k}_i dk_j\end{aligned}\tag{5.1}$$

where $I(\bar{k}_i, k_j)$ is given by eq.(3.58), renormalised for the angles which are not integrated over explicitly in the expressions above. Since the integration interval is between -1 and 1, only terms with an even power of both \bar{k}_i and k_j are non-zero, which means

$$\begin{aligned}\langle \bar{k}_y \rangle &= \frac{1}{4} \int_{-1}^1 \int_{-1}^1 \bar{\alpha} \bar{P} \bar{k}_y^2 d\bar{k}_y dk_y = \frac{1}{3} \bar{\alpha} \bar{P} \\ \langle k_y \rangle &= \frac{1}{4} \int_{-1}^1 \int_{-1}^1 \alpha P k_y^2 d\bar{k}_y dk_y = \frac{1}{3} \alpha P \\ \langle \bar{k}_i k_j \rangle &= \frac{1}{4} \int_{-1}^1 \int_{-1}^1 \bar{\alpha} \alpha C_{ij} \bar{k}_i^2 k_j^2 d\bar{k}_i dk_j = \frac{1}{9} \bar{\alpha} \alpha C_{ij} \quad .\end{aligned}\tag{5.2}$$

Using the above relations, the spin variables are given from

$$\begin{aligned}
 \bar{P} &= \frac{3}{\bar{\alpha}} \langle \bar{k}_y \rangle = \frac{3}{\bar{\alpha}} \sum_{m=1}^N \frac{\bar{k}_{y,m}}{N} \\
 P &= \frac{3}{\alpha} \langle k_y \rangle = \frac{3}{\alpha} \sum_{m=1}^N \frac{k_{y,m}}{N} \\
 C_{ij} &= \frac{9}{\bar{\alpha}\alpha} \langle \bar{k}_i k_j \rangle = \frac{9}{\bar{\alpha}\alpha} \sum_{m=1}^N \frac{\bar{k}_{i,m} k_{j,m}}{N}
 \end{aligned} \tag{5.3}$$

with errors calculated through

$$\begin{aligned}
 \sigma_{\bar{P}} &= \frac{3}{|\bar{\alpha}|} \sqrt{\frac{1}{N-1} (\langle \bar{k}_y^2 \rangle - \langle \bar{k}_y \rangle^2)} \\
 \sigma_P &= \frac{3}{|\alpha|} \sqrt{\frac{1}{N-1} (\langle k_y^2 \rangle - \langle k_y \rangle^2)} \\
 \sigma_{C_{ij}} &= \frac{9}{|\bar{\alpha}\alpha|} \sqrt{\frac{1}{N-1} (\langle \bar{k}_i^2 k_j^2 \rangle - \langle \bar{k}_i k_j \rangle^2)} .
 \end{aligned} \tag{5.4}$$

Using the same method as above the expectation values become

$$\begin{aligned}
 \langle \bar{k}_y^2 \rangle &= \int_{-1}^1 \int_{-1}^1 \bar{k}_y^2 I(\hat{\bar{k}}, \hat{k}) d\bar{k}_y dk_y = \frac{1}{4} \int_{-1}^1 \int_{-1}^1 \bar{k}_y^2 d\bar{k}_y dk_y = \frac{1}{3} \\
 \langle k_y^2 \rangle &= \int_{-1}^1 \int_{-1}^1 k_y^2 I(\hat{\bar{k}}, \hat{k}) d\bar{k}_y dk_y = \frac{1}{4} \int_{-1}^1 \int_{-1}^1 k_y^2 d\bar{k}_y dk_y = \frac{1}{3} \\
 \langle \bar{k}_i^2 k_j^2 \rangle &= \int_{-1}^1 \int_{-1}^1 \bar{k}_i^2 k_j^2 I(\hat{\bar{k}}, \hat{k}) d\bar{k}_i dk_j = \frac{1}{4} \int_{-1}^1 \int_{-1}^1 \bar{k}_i^2 k_j^2 d\bar{k}_i dk_j = \frac{1}{9}
 \end{aligned} \tag{5.5}$$

which gives the following expressions for the errors

$$\begin{aligned}
 \sigma_{\bar{P}} &= \frac{1}{|\bar{\alpha}|} \sqrt{\frac{3 - (\bar{\alpha}\bar{P})^2}{N-1}} \\
 \sigma_P &= \frac{1}{|\alpha|} \sqrt{\frac{3 - (\alpha P)^2}{N-1}} \\
 \sigma_{C_{ij}} &= \frac{1}{|\bar{\alpha}\alpha|} \sqrt{\frac{9 - (\alpha\bar{\alpha}C_{ij})^2}{N-1}} .
 \end{aligned} \tag{5.6}$$

5.2 Polarisation and Asymmetry Parameters of the Ω Hyperon

The same method as described in section 5.1 can be used to get expressions for the r coefficients for the Ω hyperon. However, since the angular distribution in the $\Omega \rightarrow \Lambda K$ decay does not only depend on the angle in one direction, it is easier to do the integrations over the initial spherical coordinates Θ and ϕ , instead of over the components of the \hat{k} vector

$$\begin{aligned}\langle k_z^2 \rangle &= \langle \cos^2 \Theta \rangle = \int \cos^2 \Theta I(\Theta, \phi) d\Omega = \frac{1}{3} - \frac{2\sqrt{3}}{15} r_0^2 \\ \langle k_y^2 \rangle &= \langle \sin^2 \Theta \sin^2 \phi \rangle = \int \sin^2 \Theta \sin^2 \phi I(\Theta, \phi) d\Omega = \frac{1}{2} - \frac{1}{2} \langle k_z^2 \rangle - \frac{3}{16} r_2^2 \\ \langle k_x k_z \rangle &= \langle \cos \Theta \sin \Theta \cos \phi \rangle = \int \cos \Theta \sin \Theta \cos \phi I(\Theta, \phi) d\Omega = \frac{1}{5} r_1^2\end{aligned}\quad (5.7)$$

where $I(\Theta, \phi)$ is given by eq.(3.36). Consequently, the r coefficients are given by the following combinations of expectation values

$$\begin{aligned}r_0^2 &= \frac{15}{2\sqrt{3}} \left(\frac{1}{3} - \langle k_z^2 \rangle \right) \\ r_2^2 &= \frac{8}{3} (1 - \langle k_z^2 \rangle - 2\langle k_y^2 \rangle) \\ r_1^2 &= 5\langle k_x k_z \rangle \quad .\end{aligned}\quad (5.8)$$

In this case the errors are given by

$$\begin{aligned}\sigma_{r_0^2} &= \frac{15}{2\sqrt{3}} \sqrt{\frac{1}{N-1} (\langle k_z^4 \rangle - \langle k_z^2 \rangle^2)} \\ \sigma_{r_2^2} &= \frac{8}{3} \sqrt{\frac{1}{N-1} ((\langle k_z^4 \rangle - \langle k_z^2 \rangle^2) + 4(\langle k_y^4 \rangle - \langle k_y^2 \rangle^2) + 2(\langle k_z^2 k_y^2 \rangle - \langle k_z^2 \rangle \langle k_y^2 \rangle))} \\ \sigma_{r_1^2} &= 5 \sqrt{\frac{1}{N-1} (\langle k_x^2 k_z^2 \rangle - \langle k_x k_z \rangle^2)} \quad .\end{aligned}\quad (5.9)$$

Calculating the expectation values $\langle k_z^4 \rangle$, $\langle k_y^4 \rangle$, $\langle k_x^2 k_z^2 \rangle$ and $\langle k_z^2 k_y^2 \rangle$, the following expressions for the errors are obtained

$$\begin{aligned}
\sigma_{r_0^2} &\approx \frac{15}{2\sqrt{3}} \sqrt{\frac{1}{N-1} (0.089 - 0.121r_0^2)} \\
\sigma_{r_2^2} &\approx \frac{8}{3} \sqrt{\frac{1}{N-1} (0.845 + 0.030r_0^2 + 0.333r_2^2)} \\
\sigma_{r_1^2} &\approx 5 \sqrt{\frac{1}{N-1} (0.067 - 0.016r_0^2)}
\end{aligned} \tag{5.10}$$

where several fractional numbers have been approximated by one decimal number and higher order terms in polarisation parameters have been neglected.

The angular distribution of the subsequent $\Lambda \rightarrow p\pi$ decay is easier to analyse. In the same way as in eq.(5.2), the expectation values of $\langle k_x \rangle$ and $\langle k_y \rangle$ can be calculated by instead inserting the angular distribution of eq.(3.44)

$$\begin{aligned}
\langle k_x \rangle &= \frac{1}{3} L \beta_\Omega \alpha_\Lambda \\
\langle k_y \rangle &= \frac{1}{3} L \gamma_\Omega \alpha_\Lambda
\end{aligned} \tag{5.11}$$

where L denotes the linear combination of polarisation parameters $\sqrt{\frac{3}{5}r_{-1}^1 + \frac{3}{2\sqrt{10}}r_{-1}^3}$. Remembering that $\alpha_\Omega \approx 0$ so that $\beta_\Omega^2 + \gamma_\Omega^2 \approx 1$, the relation between them is given by

$$\tan \phi_\Omega = \frac{\beta_\Omega}{\gamma_\Omega} = \frac{\langle k_x \rangle}{\langle k_y \rangle} \tag{5.12}$$

and the square of the linear combination of the polarisation parameters by

$$L^2 = \frac{3}{|\alpha_\Lambda|} (\langle k_x \rangle^2 + \langle k_y \rangle^2) \quad . \tag{5.13}$$

As seen, L can only be measured up to a sign. The reason is that from the beginning there are three parameters to be determined, L , β_Ω and γ_Ω , but only two observables to be measured, $\langle k_x \rangle$ and $\langle k_y \rangle$. When $\beta_\Omega^2 + \gamma_\Omega^2 \approx 1$ is used to reduce the number of parameters to two, a sign ambiguity is introduced. In the best case scenario one of the two solutions is forbidden according to the inequalities in eq.(3.60).

The errors in the expectation values are as before

$$\begin{aligned}
\sigma_{\langle k_x \rangle} &= \sqrt{\frac{1}{N-1} (\langle k_x^2 \rangle - \langle k_x \rangle^2)} = \sqrt{\frac{1}{N-1} \left(\frac{1}{3} - \frac{1}{9} L^2 \beta_\Omega^2 \alpha_\Lambda^2 \right)} \\
\sigma_{\langle k_y \rangle} &= \sqrt{\frac{1}{N-1} (\langle k_y^2 \rangle - \langle k_y \rangle^2)} = \sqrt{\frac{1}{N-1} \left(\frac{1}{3} - \frac{1}{9} L^2 \gamma_\Omega^2 \alpha_\Lambda^2 \right)}
\end{aligned} \tag{5.14}$$

and consequently

$$\begin{aligned}
\sigma_{\tan \phi_\Omega} &= \sqrt{\frac{\sigma_{\langle k_x \rangle}^2}{\langle k_y \rangle^2} + \frac{\langle k_x \rangle^2 \sigma_{\langle k_y \rangle}^2}{\langle k_y \rangle^4} + \frac{\langle k_x \rangle \text{cov}(\langle k_x \rangle, \langle k_y \rangle)}{\langle k_y \rangle^3}} = \\
&= \frac{1}{|L \cos \phi_\Omega \alpha_\Lambda|} \sqrt{\frac{1}{N-1} \left(3 - \frac{2}{3} \tan^2 \phi_\Omega - \frac{10}{9} L^2 \sin^2 \phi_\Omega \alpha_\Lambda^2 \right)} \\
\sigma_{L^2} &= \frac{9}{\alpha_\Lambda^2} \sqrt{2 \langle k_x \rangle \sigma_{\langle k_x \rangle}^2 + 2 \langle k_y \rangle \sigma_{\langle k_y \rangle}^2 + 4 \langle k_x \rangle \langle k_y \rangle \text{cov}(\langle k_x \rangle, \langle k_y \rangle)} \approx \\
&\approx \sqrt{\frac{18|L|}{|\alpha_\Lambda|^3(N-1)} \left(\sin \phi_\Omega + \cos \phi_\Omega - \frac{L^2 \alpha_\Lambda^2}{3} (\sin^3 \phi_\Omega + \cos^3 \phi_\Omega) \right)} .
\end{aligned} \tag{5.15}$$

where the very small covariance term is neglected in the last line.

From T invariance, one can deduce that $\beta = 0$ if there are no final state interactions [57]. This also means $\gamma_\Omega = \pm 1$. If this is assumed, the reconstruction of L becomes simpler. The absolute value of L can then be reconstructed from

$$|L| = \frac{3}{\alpha_\Lambda} \langle k_y \rangle \tag{5.16}$$

with the error given by

$$\sigma_{|L|} = \frac{3}{|\bar{\alpha}|} \sqrt{\frac{1}{N-1} (\langle \bar{k}_y^2 \rangle - \langle \bar{k}_y \rangle^2)} . \tag{5.17}$$

Also in this case only the absolute value of L can be reconstructed, since the sign of γ_Ω is not known.

The calculations in this section have been done for particles only, but the same expressions holds, of course, also for antiparticles.

5.3 Methods to Compensate for Angular Dependence of Reconstruction Efficiency

Depending on their decay angles in the hyperon rest systems, the final particles will go into different parts of the detector. The reconstruction efficiency for the events will therefore depend on these decay angles. This must be compensated for in the reconstruction of spin variables. Two different ways to do this are presented in this section.

5.3.1 Method Using Monte Carlo Based Acceptance Functions

The most straightforward way to compensate for the difference in detector reconstruction efficiency is to use Monte Carlo based acceptance functions. To weight the sums in eq.(5.3), both one dimensional acceptance functions for the hyperon and antihyperon, $A_Y(k_y)$ and $A_{\bar{Y}}(\bar{k}_y)$, as well as two dimensional combined ones $A(\bar{k}_i, k_j)$ are needed

$$\begin{aligned}\bar{P} &= \frac{3}{\bar{\alpha}} \langle \bar{k}_y \rangle = \frac{3}{\bar{\alpha}} \frac{\sum_{m=1}^N \frac{\bar{k}_{y,m}}{A_{\bar{Y}}(\bar{k}_y)}}{\sum_{m=1}^N \frac{1}{A_{\bar{Y}}(\bar{k}_y)}} \\ P &= \frac{3}{\alpha} \langle k_y \rangle = \frac{3}{\alpha} \frac{\sum_{m=1}^N \frac{k_{y,m}}{A_Y(k_y)}}{\sum_{m=1}^N \frac{1}{A_Y(k_y)}} \\ C_{ij} &= \frac{9}{\bar{\alpha}\alpha} \langle \bar{k}_i k_j \rangle = \frac{9}{\bar{\alpha}\alpha} \frac{\sum_{m=1}^N \frac{\bar{k}_{i,m} k_{j,m}}{A(\bar{k}_i, k_j)}}{\sum_{m=1}^N \frac{1}{A(\bar{k}_i, k_j)}}.\end{aligned}\tag{5.18}$$

A very good knowledge of the acceptance for different parts of the detector is needed to use this method. It is also hard to include the errors of the acceptance functions in the error of the reconstructed spin variables. In the case of the parameters for Ω hyperon this is the only method available.

5.3.2 Method Without the Use of Monte Carlo Based Acceptance functions

There is a way of extracting the spin variables for spin 1/2 hyperons without the use of Monte Carlo based acceptance functions [116]. Using this method the problem with the errors of the acceptance functions is avoided. The drawback is, however, that it is only approximate and depends on a symmetry in the detector acceptance. The symmetry that the method takes advantage of is the following

$$\begin{aligned}
A_Y(k_y) &= A_Y(-k_y) \\
A_{\bar{Y}}(\bar{k}_y) &= A_{\bar{Y}}(-\bar{k}_y) \quad .
\end{aligned}
\tag{5.19}$$

To see the use of this symmetry it is convenient to formulate the calculation of the spin variables in matrix form. The spin variables and expectation values of the directional cosines are then put into the following matrices and vectors

$$\begin{aligned}
D &= \begin{bmatrix} 1 & \alpha P_{\Xi^-,x} & \alpha P_{\Xi^-,y} & \alpha P_{\Xi^-,z} \\ \bar{\alpha} P_{\Xi^+,x} & \bar{\alpha} \alpha C_{xx} & \bar{\alpha} \alpha C_{xy} & \bar{\alpha} \alpha C_{xz} \\ \bar{\alpha} P_{\Xi^+,y} & \bar{\alpha} \alpha C_{yx} & \bar{\alpha} \alpha C_{yy} & \bar{\alpha} \alpha C_{yz} \\ \bar{\alpha} P_{\Xi^+,z} & \bar{\alpha} \alpha C_{zx} & \bar{\alpha} \alpha C_{zy} & \bar{\alpha} \alpha C_{zz} \end{bmatrix} \\
E &= \begin{bmatrix} \langle 1 \rangle & \langle k_x \rangle & \langle k_y \rangle & \langle k_z \rangle \\ \langle \bar{k}_x \rangle & \langle \bar{k}_x k_x \rangle & \langle \bar{k}_x k_y \rangle & \langle \bar{k}_x k_z \rangle \\ \langle \bar{k}_y \rangle & \langle \bar{k}_y k_x \rangle & \langle \bar{k}_y k_y \rangle & \langle \bar{k}_y k_z \rangle \\ \langle \bar{k}_z \rangle & \langle \bar{k}_z k_x \rangle & \langle \bar{k}_z k_y \rangle & \langle \bar{k}_z k_z \rangle \end{bmatrix}
\end{aligned}
\tag{5.20}$$

$$\bar{F} = (1, \langle \bar{k}_x^2 \rangle, \langle \bar{k}_y^2 \rangle, \langle \bar{k}_z^2 \rangle)$$

$$F = (1, \langle k_x^2 \rangle, \langle k_y^2 \rangle, \langle k_z^2 \rangle) \quad .$$

The following relations between spin variables and expectation values hold

$$\begin{aligned}
E &= \frac{1}{16\pi^2} \mathcal{A} D \mathcal{A} \\
\bar{F} &= \frac{1}{16\pi^2} \bar{\mathcal{B}} D \mathcal{C} \\
F &= \frac{1}{16\pi^2} \mathcal{C} D \mathcal{B}
\end{aligned}
\tag{5.21}$$

if the acceptance matrices and vectors are defined through

$$\begin{aligned}
\bar{\mathcal{A}}_{\mu,v} &= \int \bar{k}_\mu \bar{k}_v A_{\text{antihyp}} d\bar{\Omega} \\
\mathcal{A}_{\mu,v} &= \int k_\mu k_v A_{\text{hyp}} d\Omega \\
\bar{\mathcal{B}}_{\mu,v} &= \int \bar{k}_\mu^2 \bar{k}_v A_{\text{antihyp}} d\bar{\Omega} \\
\mathcal{B}_{\mu,v} &= \int k_\mu k_v^2 A_{\text{hyp}} d\Omega \\
\bar{\mathcal{C}}_{\mu,v} &= \int \bar{k}_\mu A_{\text{antihyp}} d\bar{\Omega} = \bar{\mathcal{A}}_{0\mu} \\
\mathcal{C}_{\mu,v} &= \int k_\mu A_{\text{hyp}} d\Omega = \mathcal{A}_{\mu 0}
\end{aligned} \tag{5.22}$$

where the k vectors has been made into four vectors with the zero component equal to 1. Using the symmetry in eq.(5.19), components with an odd power of $\cos \bar{\Theta}_y$ or $\cos \Theta_y$ are zero, *i.e.*

$$\bar{\mathcal{A}} = \begin{bmatrix} \bar{\mathcal{A}}_{00} & \bar{\mathcal{A}}_{01} & 0 & \bar{\mathcal{A}}_{03} \\ \bar{\mathcal{A}}_{10} & \bar{\mathcal{A}}_{11} & 0 & \bar{\mathcal{A}}_{13} \\ 0 & 0 & \bar{\mathcal{A}}_{22} & 0 \\ \bar{\mathcal{A}}_{30} & \bar{\mathcal{A}}_{31} & 0 & \bar{\mathcal{A}}_{33} \end{bmatrix} \tag{5.23}$$

$$\bar{\mathcal{B}} = \begin{bmatrix} \bar{\mathcal{B}}_{00} & \bar{\mathcal{B}}_{01} & 0 & \bar{\mathcal{B}}_{03} \\ \bar{\mathcal{B}}_{10} & \bar{\mathcal{B}}_{11} & 0 & \bar{\mathcal{B}}_{13} \\ \bar{\mathcal{B}}_{20} & \bar{\mathcal{B}}_{21} & 0 & \bar{\mathcal{B}}_{23} \\ \bar{\mathcal{B}}_{30} & \bar{\mathcal{B}}_{31} & 0 & \bar{\mathcal{B}}_{33} \end{bmatrix}$$

and correspondingly for \mathcal{A} and \mathcal{B} . In section 3.1.5, it was shown that the only non-zero components of D are

$$D = \begin{bmatrix} 1 & 0 & D_{02} & 0 \\ 0 & D_{11} & 0 & D_{13} \\ D_{20} & 0 & D_{22} & 0 \\ 0 & D_{31} & 0 & D_{33} \end{bmatrix}. \tag{5.24}$$

Approximate expressions for E , F and \bar{F} can be calculated using eq.(5.21). Noticing that $\mathcal{B}_{0,\mu} = \mathcal{A}_{\mu,0}$ one obtains

$$\begin{aligned}
E &= \\
&= \begin{bmatrix} \bar{\mathcal{A}}_{00}\mathcal{A}_{00} + \cdots & \bar{\mathcal{A}}_{00}\mathcal{A}_{01} + \cdots & \bar{\mathcal{A}}_{00}D_{20}\mathcal{A}_{22} & \bar{\mathcal{A}}_{00}\mathcal{A}_{03} + \cdots \\ \bar{\mathcal{A}}_{01}\mathcal{A}_{00} + \cdots & \bar{\mathcal{A}}_{01}\mathcal{A}_{01} + \bar{\mathcal{A}}_{11}D_{11}\mathcal{A}_{11} + \cdots & \bar{\mathcal{A}}_{01}D_{20}\mathcal{A}_{22} & \bar{\mathcal{A}}_{01}\mathcal{A}_{03} + \bar{\mathcal{A}}_{11}D_{13}\mathcal{A}_{33} + \cdots \\ \bar{\mathcal{A}}_{22}D_{20}\mathcal{A}_{00} & \bar{\mathcal{A}}_{22}D_{20}\mathcal{A}_{01} & \bar{\mathcal{A}}_{22}D_{22}\mathcal{A}_{22} & \bar{\mathcal{A}}_{22}D_{02}\mathcal{A}_{03} \\ \bar{\mathcal{A}}_{03}\mathcal{A}_{00} + \cdots & \bar{\mathcal{A}}_{03}\mathcal{A}_{01} + \bar{\mathcal{A}}_{33}D_{31}\mathcal{A}_{11} + \cdots & \bar{\mathcal{A}}_{03}D_{20}\mathcal{A}_{22} & \bar{\mathcal{A}}_{03}\mathcal{A}_{03} + \bar{\mathcal{A}}_{33}D_{33}\mathcal{A}_{33} + \cdots \end{bmatrix}
\end{aligned}$$

$$\bar{F} = \left(\bar{\mathcal{A}}_{00}\mathcal{A}_{00} + \cdots, \bar{\mathcal{A}}_{11}\mathcal{A}_{00} + \cdots, \bar{\mathcal{A}}_{22}\mathcal{A}_{00} + \cdots, \bar{\mathcal{A}}_{33}\mathcal{A}_{00} + \cdots \right)$$

$$F = \left(\bar{\mathcal{A}}_{00}\mathcal{A}_{00} + \cdots, \bar{\mathcal{A}}_{00}\mathcal{A}_{11} + \cdots, \bar{\mathcal{A}}_{00}\mathcal{A}_{22} + \cdots, \bar{\mathcal{A}}_{00}\mathcal{A}_{33} + \cdots \right). \quad (5.25)$$

where higher order terms in acceptances have been neglected. The spin variables can be obtained by combining the components of E , F and \bar{F}

$$\begin{aligned}
\bar{P} &= \frac{1}{\alpha} \frac{\langle \bar{k}_y \rangle}{\langle \bar{k}_y^2 \rangle} \\
P &= \frac{1}{\alpha} \frac{\langle k_y \rangle}{\langle k_y^2 \rangle} \\
C_{xx} &= \frac{1}{\alpha \bar{\alpha}} \frac{\langle \bar{k}_x k_x \rangle - \langle \bar{k}_x \rangle \langle k_x \rangle}{\langle \bar{k}_x^2 \rangle \langle k_x^2 \rangle} \\
C_{yy} &= \frac{1}{\alpha \bar{\alpha}} \frac{\langle \bar{k}_y k_y \rangle}{\langle \bar{k}_y^2 \rangle \langle k_y^2 \rangle} \\
C_{zz} &= \frac{1}{\alpha \bar{\alpha}} \frac{\langle \bar{k}_z k_z \rangle - \langle \bar{k}_z \rangle \langle k_z \rangle}{\langle \bar{k}_z^2 \rangle \langle k_z^2 \rangle} \\
C_{xz} &= \frac{1}{\alpha \bar{\alpha}} \frac{\langle \bar{k}_x k_z \rangle - \langle \bar{k}_x \rangle \langle k_z \rangle}{\langle \bar{k}_x^2 \rangle \langle k_z^2 \rangle} \\
C_{zx} &= \frac{1}{\alpha \bar{\alpha}} \frac{\langle \bar{k}_z k_x \rangle - \langle \bar{k}_z \rangle \langle k_x \rangle}{\langle \bar{k}_z^2 \rangle \langle k_x^2 \rangle} .
\end{aligned} \tag{5.26}$$

These are however approximate expressions since terms have been neglected in eq.(5.25). In addition, they are only valid if the symmetry in eq.(5.19) is true. The covariance matrix of the expectation values in eq.(5.26) can be calculated using [115]

$$V_{ij} = \frac{1}{N(N-1)} \left(\sum_{n=1}^N f_i f_j - \frac{1}{N} \left(\sum_{n=1}^N f_i \right) \left(\sum_{n=1}^N f_j \right) \right) \tag{5.27}$$

where the functions f are the different combinations of cosines in eq.(5.26). The errors and covariances can then be propagated to give the errors in the spin correlations.

The two different ways to reconstruct spin variables described in this and the previous section will be compared for the case of $\bar{p}p \rightarrow \bar{\Xi}^+ \Xi^-$ in section 6.2.10

5.4 CP violation parameters

In the CP violation parameters described in section 3.2 asymmetry parameters of hyperons are compared to the asymmetry parameters of the corresponding antihyperons. From an experimental point of view, the problem is that the hyperons and antihyperons can decay in very different part of detector. It may therefore happen that different acceptance in different parts of the detector introduce systematical uncertainties, if the asymmetry parameters were mea-

sured separately and then compared. A better strategy is to relate the CP violation to up-down counting asymmetries [72], so that the detector acceptance only needs to be symmetric on the average with respect to the different sides of the antihyperon-hyperon production plane.

To see the relation of the difference in particles going up and down to α and $\bar{\alpha}$, consider the distribution of N events with respect to k_y and \bar{k}_y

$$\frac{d^2N}{dk_y d\bar{k}_y} = \frac{N}{4} (1 + \alpha P k_y + \bar{\alpha} P \bar{k}_y + \alpha \bar{\alpha} C_{yy} k_y \bar{k}_y) \quad . \quad (5.28)$$

If the numbers of events where decay baryons and antibaryons go in certain direction are denoted with two indices, + meaning up with respect to the antihyperon hyperon production plane and - meaning down, the expression above can be integrated to give

$$\begin{aligned} N^{++} &= \int_0^1 \int_0^1 \frac{d^2N}{dk_y d\bar{k}_y} dk_y d\bar{k}_y = \frac{N}{4} \left(1 + \frac{\alpha + \bar{\alpha}}{2} P + \frac{\alpha \bar{\alpha}}{4} C_{yy} \right) \\ N^{--} &= \int_{-1}^0 \int_{-1}^0 \frac{d^2N}{dk_y d\bar{k}_y} dk_y d\bar{k}_y = \frac{N}{4} \left(1 - \frac{\alpha + \bar{\alpha}}{2} P + \frac{\alpha \bar{\alpha}}{4} C_{yy} \right) \\ N^{+-} &= \int_0^1 \int_{-1}^0 \frac{d^2N}{dk_y d\bar{k}_y} dk_y d\bar{k}_y = \frac{N}{4} \left(1 + \frac{\alpha - \bar{\alpha}}{2} P - \frac{\alpha \bar{\alpha}}{4} C_{yy} \right) \\ N^{-+} &= \int_{-1}^0 \int_0^1 \frac{d^2N}{dk_y d\bar{k}_y} dk_y d\bar{k}_y = \frac{N}{4} \left(1 - \frac{\alpha - \bar{\alpha}}{2} P - \frac{\alpha \bar{\alpha}}{4} C_{yy} \right) \quad . \end{aligned} \quad (5.29)$$

To get the $(\alpha + \bar{\alpha})$ numerator in the CP violation parameter A , one uses events where the baryons and antibaryons go the same way, since

$$\frac{N^{++} - N^{--}}{N} = \frac{\alpha + \bar{\alpha}}{4} P \quad (5.30)$$

while

$$\frac{N^{+-} - N^{-+}}{N} = \frac{\alpha - \bar{\alpha}}{4} P \quad . \quad (5.31)$$

The first expression can consequently be used as an up-down counting asymmetry probing CP violation, while the second with events where the baryon and antibaryon go opposite ways is not important. The relation to the A parameter can be seen through

$$\tilde{A} = \frac{N^{++} - N^{--}}{N} = \frac{\alpha + \bar{\alpha}}{4} P = \frac{\alpha + \bar{\alpha}}{\alpha - \bar{\alpha}} (\alpha - \bar{\alpha}) \frac{P}{4} \approx A \frac{|\alpha|}{2} P \quad . \quad (5.32)$$

In a plane spanned by k_y and \bar{k}_y , the above expression corresponds to comparing the number of events in the upper right quadrant to the lower left. It is however possible to obtain better statistics by using the events in all four quadrants [72]. To see this, again consider the expression for how the events are distributed with respect to the y axes

$$\frac{d^2N}{dk_y d\bar{k}_y} = \frac{N}{4} (1 + \alpha P k_y + \bar{\alpha} P \bar{k}_y + \alpha \bar{\alpha} C_{yy} k_y \bar{k}_y) \quad . \quad (5.33)$$

If new variables $u = \frac{1}{2}(k_y + \bar{k}_y)$ and $v = \frac{1}{2}(k_y - \bar{k}_y)$ are introduced, the expression turns into

$$\frac{d^2N}{dudv} = \frac{N}{4} (1 + (\alpha + \bar{\alpha})Pu + (\alpha - \bar{\alpha})Pv + \alpha \bar{\alpha} C_{yy}(u^2 - v^2)) \quad . \quad (5.34)$$

If this expression, after v is integrated out, is evaluated at u or $-u$ only one term differ. The following subtraction becomes proportional to the previous CP violation parameter

$$\left. \frac{dN}{du} \right|_u - \left. \frac{dN}{du} \right|_{-u} = \frac{N}{4} (\alpha + \bar{\alpha})Pu = N\tilde{A}u \quad . \quad (5.35)$$

When integrated over events with positive and negative values of u respectively, the new CP violation parameter becomes

$$\tilde{A} = \frac{\int_0^1 \int_{-1}^1 \frac{d^2N}{dudv} dudv - \int_0^{-1} \int_{-1}^1 \frac{d^2N}{dudv} dudv}{\int_0^1 \int_{-1}^1 \frac{d^2N}{dudv} dudv + \int_0^{-1} \int_{-1}^1 \frac{d^2N}{dudv} dudv} \quad . \quad (5.36)$$

Consequently, the way to get as high statistics as possible is to compare the number of events with positive values of u to the number of events with negative values of u . The distributions of events in all four quadrants are used in this expression. The important thing for the detector acceptance is then that it is symmetric on both sides of the $u = 0$ diagonal in the k_y, \bar{k}_y plane.

In the corresponding expression for \hat{B} , positive and negative values of v should be compared. In this case the events are distributed with respect to the y axes according to

$$\frac{d^2N}{dudv} \propto 1 + \frac{\pi}{4} (\bar{\alpha}_2 \bar{\beta}_1 + \alpha_2 \beta_1) Pu + \frac{\pi}{4} (\bar{\alpha}_2 \bar{\beta}_1 - \alpha_2 \beta_1) Pv \quad (5.37)$$

where u and v now are built up by k_y and \bar{k}_y of the second decay. Because of the additional $\alpha/\bar{\alpha}$ factor from the second decay¹, it is the v term which has the factor $(\beta + \bar{\beta})$ that is needed for the B parameter. The same reasoning

¹ Since $\bar{\alpha} = -\alpha$ the v term can be rewritten as $-\frac{\pi}{4} (\bar{\beta}_1 + \beta_1) |\alpha_2| Pv$.

as for the \dot{A} holds this case, now integrating over u and comparing v to $-v$, resulting in

$$\dot{B} = \frac{\int_{-1}^1 \int_0^1 \frac{d^2 N}{dudv} dudv - \int_{-1}^1 \int_0^{-1} \frac{d^2 N}{dudv} dudv}{\int_{-1}^1 \int_0^1 \frac{d^2 N}{dudv} dudv + \int_{-1}^1 \int_0^{-1} \frac{d^2 N}{dudv} dudv} . \quad (5.38)$$

The parameter sensitive to CP violation is in this case the difference of the number of events on both sides of the $v = 0$ diagonal.

6. Simulations of Multi-Strange and Charmed $\bar{p}p \rightarrow \bar{Y}Y$ Reactions

Simulations of multi-strange and charmed $\bar{p}p \rightarrow \bar{Y}Y$ reactions for PANDA are presented in this chapter. Previous simulations have exclusively dealt with single-strangeness hyperons [94]. Going into the multi-strange and charmed sector of antihyperon-hyperon physics very little, if anything, is experimentally known. Simulations were made for the reactions $\bar{p}p \rightarrow \bar{\Xi}^+\Xi^-$, $\bar{p}p \rightarrow \bar{\Omega}^+\Omega^-$ and $\bar{p}p \rightarrow \bar{\Lambda}_c^-\Lambda_c^+$, to see what experimental information can be expected from PANDA. Special attention was given to the reconstruction of spin variables. Simulations to investigate the possibility to improve limits on CP violation parameters are presented in the last part of the chapter. Before the sections containing the results of the simulations, the used simulation framework is presented.

6.1 The Simulation Framework

The simulations presented in this thesis use the same simulation framework, which was used for the PANDA physics performance report [37]. This software has in large part been taken from other high energy experiments and been adjusted for PANDA and can therefore be considered as well tested. The approach is object oriented and most of the code is written in C++.

As event generator EvtGen [117], which was initially developed by the BaBar collaboration, is used. The generated particles are then followed through the detector using the GEANT4 [118, 119] transport code. The interactions and decays that may happen to the particles in the detector are considered in GEANT4. A collection of hits is given as output, consisting of the intersection points and energy losses of all particles in the individual subdetectors. This information is then used as input for the next step, which is the digitisation. The digitisation models the signals from the individual subdetectors and the processing of these in the front end electronics. The purpose is to produce a detector output as similar as possible to real experimental data, so that the same reconstruction code can be used for the simulations and future experimental data. For performance reasons, an effective smearing is used instead, for some subdetectors. This effective smearing has been derived from Monte Carlo calculations with full digitisation.

The detector setup used in the simulations was described in chapter 2. The pellet option is chosen as target, with a spread of the interaction point of $\sigma = 0.275$ mm in each direction. A detailed description of the simulation framework is given in [37].

6.1.1 Digitisation

For the MVD, the readout is different for the two types of detectors, silicon strip and pixel, and they are treated in different ways in the digitisation. The channel number in the detection is defined by the hit position on the surface of the sensor. The charge collected by electronics is given by the energy deposition. For the pixel detectors, the trajectory was projected to the surface and used to calculate all excited pixels which share the charge signal depending on their fraction of the track. The strips are treated in a similar way, but give information in only one dimension. The threshold for the electronics signal was set to the equivalent of 300 electrons.

The same method for digitisation is used for both the STT and the drift chambers. The local helix trajectory of a charged particle passing through the gas is derived from the GEANT4 intersection points. The shortest distance from this helix to the wire is used, to get the drift time of the ionisation electrons. This distance is smeared with a Gaussian distribution of $\sigma = 150$ μm for the STT and $\sigma = 200$ μm for the drift chambers, to take the resolution in drift time into account.

The GEMs have two detector planes separated by 1 cm. They are modeled to have two strips in each detector layer, oriented perpendicular to each other. No detailed simulation of the gas amplification process and response of the strip detectors is performed. Instead, the entry point of a charged track into the detector plane is used. This was taken directly from GEANT4 and then smeared with a Gaussian distribution of $\sigma = 70$ μm .

For the DIRC, one joint method is used to take the light propagation in the radiators, the signal processing in the front-end electronics and the reconstruction of the Cherenkov angle into account. The resolution of the reconstructed Cherenkov angle is taken to be the uncertainty of the single photon angle divided by the square root of the number of detected Cherenkov photons. A value of 10 mrad is used for the uncertainty of the single photon angle. The number of photons is calculated using the velocity of the charged particle, its path length in the radiator, a sensitive wavelength interval of [280 nm, 350 nm] and a total efficiency of 7.5% per photon. For 1 GeV/c pions, the average number of detected photons varies between 20 and 40 depending on the polar angle. In this way a resolution of the Cherenkov angle of $\sigma = 2.33$ mrad is obtained.

6.1.2 Track Reconstruction

The information of a charged particle's trajectory through the detector is kept in the track object, which contains hits from the different subdetectors used for tracking. The residual to a reference trajectory and the precision of the measurement are given for each hit. For the STT, the hit residual is the closest distance from the trajectory to the wire of the straw minus the actual drift distance. For the MVD and the GEMs, the residual is the distance between the sensor and the trajectory in the detector plane. Monte Carlo truth information is used to assign the reconstructed hits to the right track. The pattern recognition is, in this sense, an idealised version compared to real data. Tracks with less than 8 detector hits are rejected. A Kalman Filter algorithm is used to fit the tracks in the target spectrometer. This algorithm considers the hit measurements, their resolutions and the effect of interactions with detector material. The implementation of the algorithm is done in the same way as in the reconstruction software of the BaBar collaboration. A description of this implementation is given in [120]. The magnetic field is assumed to be constant and parallel to the beam axis.

For the forward spectrometer, a χ^2 is calculated from the hit residuals in the drift chambers. A Runge-Kutta integration method is used for the propagation of the track through the detector and the MINUIT [121] package is used to minimize χ^2 . This results in a five-parameter helix and its covariant matrix. These are then used as constraints in a Kalman filter fit when including also hits in the target spectrometer. Since multiple scattering and energy loss effects depend on particle type, the tracks are refitted for the five different particle hypotheses: e, μ , π , K and p.

To investigate the efficiency of this track reconstruction algorithm, a track is considered to be well reconstructed if the difference between the generated and reconstructed momentum is less than 3σ of its resolution. For pions generated at 60° polar angle, 90% of the tracks are well reconstructed for transverse momenta over 0.2 GeV/c, while the efficiency falls to 70% for a transverse momentum of 0.1 GeV/c. This efficiency is comparable to real data from the BaBar detector [122].

6.1.3 Charged Particle Identification

The software for charged particle identification uses two steps. The identification is first performed for each subdetector individually, resulting in probabilities for all five particle hypotheses: e, μ , π , K and p. Then, the global particle identification (PID) combines information from all subdetectors by using a likelihood method. The result is four different particle candidate lists for each particle, with increasingly strict demand on the global likelihood for the particle type in question. The lists are called VeryLoose, Loose, Tight and Very-Tight. For the particles of interest for this thesis (π , K, p), the lists correspond to selection criteria with the following minimal values for the global likeli-

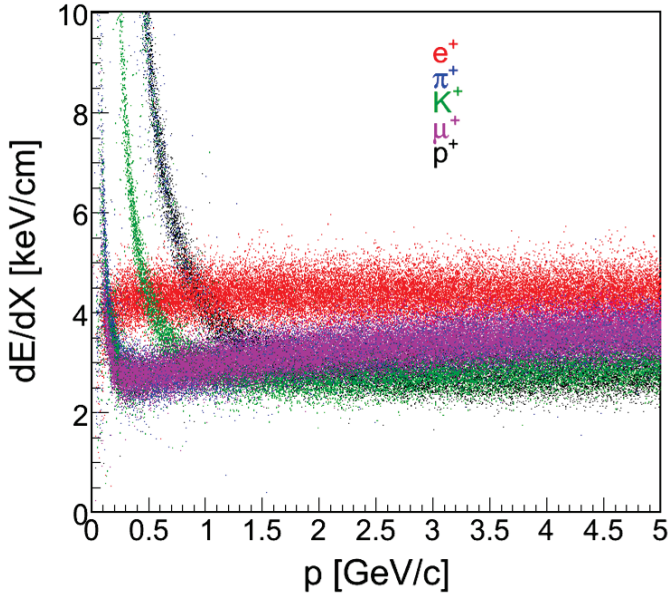


Figure 6.1: dE/dx plot from the STT as a function of momentum for five different particles [37].

hood: VeryLoose 20%, Loose 30%, Tight 55% and VeryTight 70%. There is also a list consisting of all charged tracks with no PID selection criterium, called ChargedTracks.

For the lower momenta, the information for particle identification is mainly supplied by energy loss, dE/dx , measurements in the MVD and the STT. The energy loss depends both on particle type and momentum. A plot of energy loss in the STT versus momentum is shown in figure 6.1. There are two drawbacks with this method. First, the energy loss distributions of the different particles overlap at certain momenta, as seen in figure 6.1. Second, the distributions have long tails, which obstructs the identification.

A track gives rise to at most 4 hits in the barrel part of the MVD and 5-6 hits in the forward part. This means that the PID information from the MVD is quite limited. Still this information can be used to separate protons and kaons from the other particle types, which are superpositioned in the same band in a dE/dx vs momentum plot. Instead of summing the individual dE/dx hit measurements, they are combined into the quantity

$$S = \frac{\sum dE_i}{\sum dx_i} n_e^{-1} \quad (6.1)$$

where n_e^{-1} is the electron density in silicon. This quantity gives a smaller spread of the energy loss distribution. The energy loss distributions are described by a Landau distribution, to which all uncertainties merged into a single Gaussian distributed error is added. The resulting distribution has three momentum dependent parameters. These parameters have been fitted with polynomials for each particle type by generating single particle events from 50 MeV/c to 1.5 GeV/c, which are then used for the calculation of particle hypothesis.

The energy loss of charged particles traversing individual straws of the STT will be measured. Since these measurements are performed in thin layers of only a few mm of gas there will be fluctuations which give rise to a long Landau tail in the energy loss distribution. The truncated arithmetic mean is used to deal with this problem. The choice of the truncation parameter is a compromise between the resolution of the Gaussian fit and how much of the tail that still remains after the truncation. The best value is found for a truncation parameter of 70, which means that 70% of the lowest energy loss values are kept. The parameters of the Gaussian have been generated for the five particle types in the angular range covered by the STT for momenta from 400 MeV/c up to the maximum momenta allowed for a beam momentum of 15 GeV/c. These parameters are then used to calculate probabilities for all five particle types, which can then be directly combined with information from other detectors in the global PID. A lower limit on the likelihood is set to 1% to take possible non-Gaussian tails into account. Using this method for electrons, the PID efficiency of the STT is over 98% for momenta between 0.2 and 5 GeV/c, while the contamination¹ from other particles varies from 1% to 16%. The contamination increases for forward angles due to the decrease of the number of hits in the STT.

The particle identification information for higher momenta comes mainly from the DIRC. If a charged track can give rise to Cherenkov light in the DIRC, the expected Cherenkov angle and its errors are calculated using the reconstructed momentum, the reconstructed path length and the particle hypothesis. This value is then compared with the measured Cherenkov angles to calculate the likelihood and significance level for each particle type. As an example, using the Loose criterion for kaons gives an efficiency of 80% for identification in the DIRC above the Cherenkov threshold of approximately 500 MeV/c. The fraction of pions misidentified as kaons is less than 0.1% below 3 GeV/c momentum and increases to 10% for 5 GeV/c momentum.

¹The probability for other particles to be identified as electrons.

The identification of protons, pions and kaons cover all the final states of the processes in the simulations of this thesis. For the identification of electrons and muons, information from the EMC and muon detectors is used in addition.

The information of all subdetectors are combined with a standard likelihood method in the global PID. The probability that a track is of a certain particle type, $p(k)$, is calculated from the likelihoods from each individual subdetector using the expression

$$p(k) = \frac{\prod_i p_i(k)}{\sum_j \prod_i p_i(j)} \quad (6.2)$$

where the index i runs over the subdetectors used for PID and the index j runs over the five particle types. These probabilities are used for the particle candidate lists.

6.1.4 Analysis

The data needed for physics analysis are saved at three levels of different detail:

- the TAG level, containing brief event summary data
- the Analysis Object Data (AOD), which consists of the particle candidate lists as well as Monte Carlo truth data
- the Event Summary Data (ESD), which includes data down to the level of detector hits

Most physics simulations, including those of this thesis, do not use the detailed ESD data.

The analysis is performed in three steps. First, a fast preselection using only the TAG data is done. For events which do not pass this preselection, only the TAG data is saved. This decreases the time needed for analysis jobs significantly. The second step is an event reconstruction and refined event selection using the AOD data. The events are reconstructed by building decay trees and applying geometrical and kinematic fits. Cuts on invariant masses, fit probabilities and kinematic properties can be applied in this step, using Beta, BetaTools and fitters [123], which has been taken from BaBar and then adapted for PANDA. In simulations for exclusive physics reactions, a kinematical fit of the reconstructed decay tree has been found to be especially important to improve the quality of the data and suppress background. The higher level analysis is performed using the ROOT [124] toolbox, in the last step.

6.1.5 Ongoing Software Development

A new simulation framework for PANDA, called PANDArroot, is under development. The FAIRroot framework [125] will provide the most important services for detector simulations and offline analysis. FAIRroot is based on

ROOT and the Virtual Monte Carlo (VMC) [126] interface. PANDAroot will, in contrast to the old framework, provide a complete reconstruction and pattern recognition chain. It will be possible to use different transport models for the simulations. So far GEANT3 [127], GEANT4 and Fluka [128] can be used. The possibility to switch transport model will increase the lifetime and validity of the framework significantly. The information from the transport model is digitised to simulate signals from individual subdetectors. After this the data is in the same format as real experimental data. The reconstruction takes only the digitised data as input, and no Monte Carlo information of the true origin of hits is used. Consequently, it will also be possible to study background from fake tracks and pileup effects. Algorithms based on conformal mapping [129] and extended Riemann techniques [130] will be used to find charged tracks and correlate them with information from the PID detectors. PANDAroot will also include a track follower based on the GEANE package [127] combined with a generic Kalman filter for momentum reconstruction for charged particles. The new framework will also include a fast-simulation package, based on a parametrisation of the subdetector responses, in order to be able to generate a large number of background events in a manageable time. The Rho package [131] will be used in PANDAroot, for higher level analysis. Vertex and kinematic fitting tools, based on the KFitter package from the Belle collaboration [132], will also be included.

6.2 The $\bar{p}p \rightarrow \bar{\Xi}^+ \Xi^-$ Reaction

6.2.1 Data Generation

Approximately $4 \cdot 10^6$ events, with the decays $\Xi^- \rightarrow \Lambda \pi^-$ and $\Lambda \rightarrow p \pi^-$, were generated at a beam momentum of 4 GeV/c. There is no experimental data for the differential cross section of $\bar{p}p \rightarrow \bar{\Xi}^+ \Xi^-$, but it is reasonable that the creation of two $s\bar{s}$ pair instead of one should make the angular distribution more isotropic compared to $\bar{p}p \rightarrow \bar{\Lambda} \Lambda$. The $\bar{p}p \rightarrow \bar{\Xi}^+ \Xi^-$ events were therefore generated with an isotropic angular distribution of the $\bar{\Xi}^+$ particles.

Polarisation and spin correlations were applied using weights, according to eq.(3.58). The polarisation and spin correlations must be zero when the momentum of $\bar{\Xi}^+$ is parallel to the beam axis, *i.e.* when $\cos \Theta_{\bar{\Xi}^+} = \pm 1$. Since no data on spin variables exists for the $\bar{p}p \rightarrow \bar{\Xi}^+ \Xi^-$ reaction, sine functions were used, so that the value 0 was obtained for $\cos \Theta_{\bar{\Xi}^+} = \pm 1$. More specifically, the following functions were used for the different spin variables

$$\begin{aligned} P_{\bar{\Xi}^+,y} &= P_{\Xi^-,y} = \sin 2\Theta_{\bar{\Xi}^+} \\ C_{\bar{x},x} &= C_{\bar{y},y} = C_{\bar{z},z} = C_{\bar{x},z} = \sin \Theta_{\bar{\Xi}^+} \quad . \end{aligned} \quad (6.3)$$

6.2.2 Event Reconstruction

The $\bar{p}p \rightarrow \bar{\Xi}^+ \Xi^-$ reaction has four displaced vertices, see figure 4.8. Therefore the problem with background is not expected to be very severe. No strict requirements on PID probabilities were therefore used. The particles in the final state are protons and pions. For the protons the VeryLoose candidate list was used. The PID for the pions has very low efficiency, since many of them spiral in the magnetic field and therefore do not travel a sufficiently large distance in the STT. To get an acceptable reconstruction efficiency, the ChargedTracks list was used for pions. Using particle candidates from these lists the reconstruction was done according to the following steps:

- Identified pairs of antiprotons (protons) and π^+ (π^-) were fitted to a common vertex under a $\bar{\Lambda}$ (Λ) hypothesis, requiring a χ^2 probability > 0.001 .
- The invariant $\bar{p}\pi^+$ ($p\pi^-$) mass window was set to $1.110 \text{ GeV}/c^2 \leq M_{\Lambda} \leq 1.120 \text{ GeV}/c^2$.
- Pairs of $\bar{\Lambda}$ (Λ) and π^+ (π^-) were fitted to a common vertex under a $\bar{\Xi}^+$ (Ξ^-) hypothesis, requiring a χ^2 probability > 0.001 .
- The invariant $\bar{\Lambda}\pi^+$ ($\Lambda\pi^-$) mass window was set to $1.310 \text{ GeV}/c^2 \leq M_{\Xi} \leq 1.330 \text{ GeV}/c^2$.
- The remaining events were fitted to the $\bar{p}p \rightarrow \bar{\Xi}^+ \Xi^-$ hypothesis in a 4C treefit, requiring a χ^2 probability > 0.001 .

6.2.3 Reconstruction Efficiency and Background

An overall efficiency of 0.18 was obtained to reconstruct $\bar{p}p \rightarrow \bar{\Xi}^+ \Xi^-$ events by using the criteria outlined in section 6.2.2. To get an estimate of how many reconstructed events one may expect in PANDA, the experimental cross section of approximately $2 \mu\text{b}$ and the expected luminosity of $2 \cdot 10^{32} \text{ cm}^2\text{s}^{-1}$ were used. Also needed are the branching ratios for the decays of interest. The branching ratio for $\Xi \rightarrow \Lambda\pi$ is practically 100%, while the branching ratio for $\Lambda \rightarrow p\pi$ is 64% [95]. This branching ratio comes in squared, since both the Λ and the $\bar{\Lambda}$ must decay to $p\pi$. Thus, the number of reconstructed events per second becomes

$$0.18 \cdot \mathcal{L} \sigma \text{BR}(\Lambda \rightarrow p\pi)^2 \approx 30 \text{ events/s} \quad (6.4)$$

A large amount of data will consequently be collected in a short time. As a comparison, the only existing data points in figure 4.1 for this reaction are from bubble chamber experiments with only a handful of events.

The four displaced decay vertices of the $\bar{p}p \rightarrow \bar{\Xi}^+ \Xi^-$ reaction, see figure 4.8, put very severe constraints on the background. We therefore expect that a main background channel is $\bar{p}p \rightarrow \bar{\Sigma}^+(1385)\Sigma^-(1385)$, since it has the same final state ($\bar{\Lambda}\Lambda\pi^+\pi^-$) as the $\bar{\Xi}^+ \Xi^-$ channel, and a similar cross section [133]. 10^6 events of this channel were generated and none passed the selection criteria, described in the section 6.2.2. Consequently the signal to noise ratio is at least 5000 for this background channel. The direct $\bar{p}p \rightarrow \bar{\Lambda}\Lambda\pi^+\pi^-$ reaction should also be studied as background.

6.2.4 Reconstruction Efficiency as a Function of the $\bar{\Xi}^+$ Production Angle

The reconstruction efficiency as a function of the CM production angle of $\bar{\Xi}^+$ is shown in figure 6.2. It can be seen that the efficiency goes down in the forward and backward direction. This is a consequence of particles being lost in the beam pipe. There is an significant asymmetry in efficiency around $\cos \theta_{\bar{\Xi}^+} = 0$. No such asymmetry would be present if particles and antiparticles were treated the same way, since the direction of Ξ^- is exclusively determined to be the opposite of $\bar{\Xi}^+$. The asymmetry disappears if the Charged-Tracks list was used for the protons. The reason must therefore be that the PID has different efficiency for protons and antiprotons. For measurements where it is important to have symmetric reconstruction efficiency, *i.e.* CP violation measurements, it is therefore important to ignore particle identification and consider all charged tracks. It should be noted that the efficiency is non-zero for all CM angles, which means that the differential cross section and the spin variables can be reconstructed for all values of $\cos \Theta_{\bar{\Xi}^+}$.

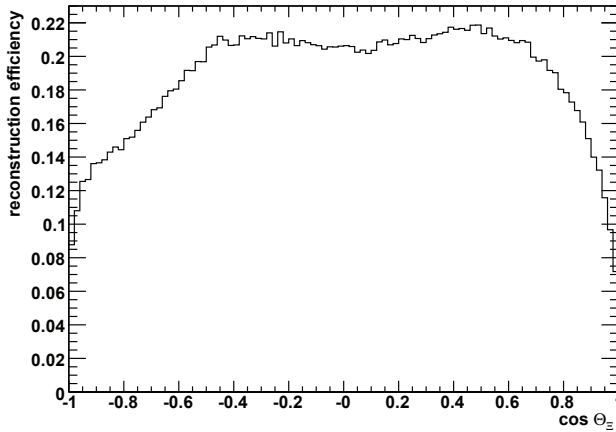


Figure 6.2: The reconstruction efficiency as a function of the CM production angle of Ξ^+ in the $\bar{p}p \rightarrow \Xi^+\Xi^-$ reaction at a beam momentum of 4 GeV/c.

6.2.5 Reconstruction of Decay Vertices

The position of the decay vertices of the Ξ^+ and the subsequent $\bar{\Lambda}$ particles are shown in figure 6.3. The relatively long lifetimes of these hyperons mean that they can go a long way in the detector before they decay. As seen in the figure, the decay vertices can be over a meter away from the interaction point in forward direction and up to half a meter in the radial direction. Also notable is that the reconstruction efficiency depends on the position of the decay vertices. The reconstruction efficiency decreases for small angles, where particles may be lost in the beam pipe, and for large angles, where particles may go in directions where the distance traveled in the STT and the GEMs is short.

6.2.6 Ξ^- Lifetime Reconstruction

The number of Ξ^- decays as a function of time is proportional to the number of Ξ^- hyperons left, which follows the ordinary decay law

$$N(t) = N_0 e^{-\lambda t} \quad (6.5)$$

where λ is the decay constant and the lifetime is defined as $\tau = \frac{1}{\lambda}$. Since the Ξ^- hyperons move with relativistic velocities, one must use the proper time of the hyperons. If the velocity and the distance, x , traveled by the hyperon is known, the proper time can be calculated through $t = \frac{x}{c\beta\gamma}$. Furthermore, the reconstruction efficiency becomes worse for events where the hyperons decay after a long time, since the hyperon vertices are far away from the interaction point and many subdetectors may have no signals. This must also be taken

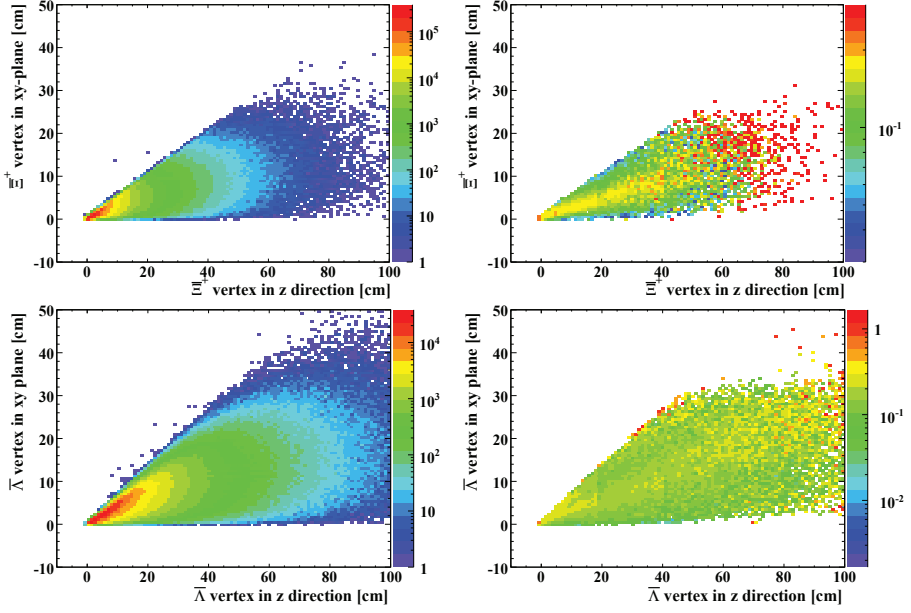


Figure 6.3: Decay vertex distributions of the Ξ^+ (upper figures) and Ξ^- (lower figures) hyperon in the $\bar{p}p \rightarrow \Xi^+\Xi^-$ reaction at a beam momentum of 4 GeV/c. The Monte Carlo truth distributions are shown in the left figures and the reconstruction efficiency dependencies on the decay vertex position are shown in the right figures.

into account. The reconstruction efficiency dependency on the Ξ^- proper time before decay is shown in figure 6.4. The time distribution corrected for the reconstruction efficiency is also shown. Fitting an exponential function in the interval between $t = 0.1$ and $t = 0.4$ ns, a Ξ^- lifetime of 0.1640 ± 0.0001 ns is obtained. The agreement with the established tabulated value of 0.1639 ± 0.0015 ns [95] is very good.

The distance that the hyperon travels in the detector is determined by its momentum and lifetime. The relation between distance traveled and lifetime is shown in figure 6.5, where the distance from interaction point to the Ξ^- vertex is plotted against the proper time of Ξ^- before decay.

6.2.7 Invariant Mass

The reconstructed invariant masses of Ξ^+ and Ξ^- are shown in figure 6.6. Fitting the two histograms with Gaussians gives a σ of 2.1 MeV/c² and 1.7 MeV/c², respectively. The σ of the Ξ^- mass is comparable to those obtained in previous simulations of $\bar{p}p \rightarrow \Xi^+\Xi^-$ [94], where the RMS of the reconstructed mass varied between 1 and 2 MeV/c² for beam momenta between 1.64 GeV/c and 15 GeV/c.

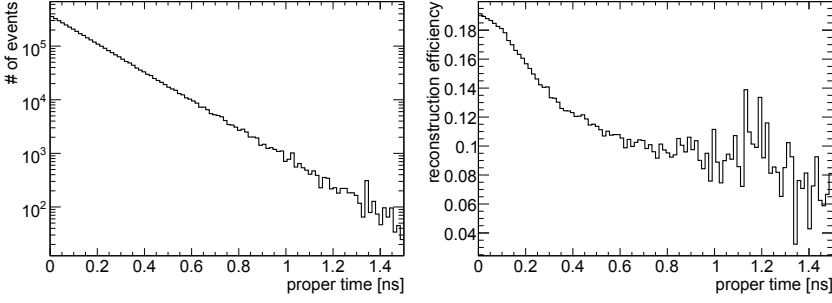


Figure 6.4: Reconstructed proper lifetime of the Ξ^- hyperon corrected for acceptance (left) and the reconstruction efficiency dependence on lifetime (right).

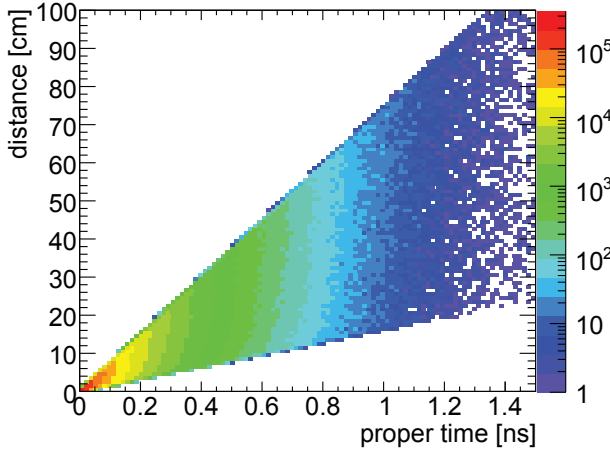


Figure 6.5: Proper time of the Ξ^- hyperon before decay versus its distance traveled in the detector.

6.2.8 Correction for the Bending of the Ξ^+ and Ξ^- Trajectories in the Magnetic Field

Since Ξ^+ and Ξ^- are charged particles, their trajectories are bent by the magnetic field. This influences their momentum vectors, so that the direction of the momentum vectors at their decay are not the same as at their production. The reconstructed momentum is the momentum at the time of the decay. However, the polarisation and the spin correlations relate to the momentum of the Ξ hyperons at the production. Consequently, the momentum at the production has to be calculated from the momentum at the decay. The magnetic field in the PANDA detector is in the direction of the beam axis, which means that only the part of the momentum which is perpendicular to the beam axis is affected.

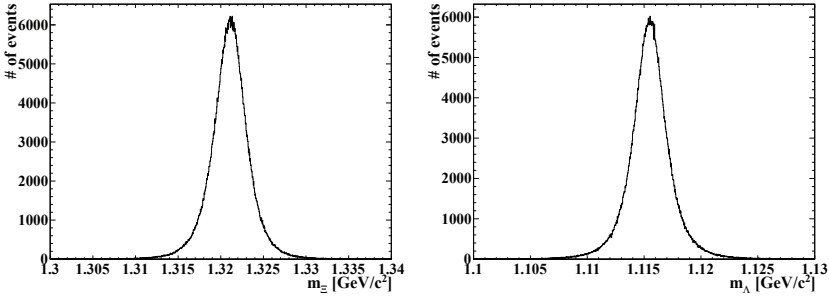


Figure 6.6: Reconstructed invariant mass of Ξ^+ (left) and $\bar{\Lambda}$ (right).

The perpendicular part of the momentum is bent in a circular pattern with a radius given by

$$R = \frac{p_{\perp}}{0.3B} \quad (6.6)$$

where p_{\perp} is the hyperon momentum transverse to the beam axis and B the magnetic field [15]. The momentum at the production can therefore be calculated, when the production and decay vertices are known. The reconstructed momentum versus the Monte Carlo truth at production before and after the correction for the bending in the magnetic field is shown in figure 6.7. There are two solutions to the calculation of momentum at production, corresponding to two trajectories between production and decay with the same bending radius but with opposite bending direction. Depending on the sign of the x -component of the hyperon momentum, different solutions should be chosen. A band of points perpendicular to the main diagonal close to zero momentum is clearly seen in the figure showing corrected momentum in y direction. These are events where the wrong solution was chosen, due to the small momentum. These are very few events and pose no real problem. The difference between the reconstructed momentum and the Monte Carlo truth at production is shown in figure 6.8. It can be seen that the σ goes from 5.3 MeV/c to 1.9 MeV/c in the x and y direction, when the correction for the bending in the magnetic field is applied.

6.2.9 Reconstruction Efficiency as a Function of the $\bar{\Lambda}$ Decay Angle in the Ξ^+ rest frame

The calculation of spin variables uses the decay angles of the Λ hyperon in the Ξ rest system, as defined in section 3.1.5. It is therefore important to investigate how the reconstruction efficiency depends on these decay angles. It can be seen in figure 6.9 that the reconstruction efficiency is non-isotropic. The

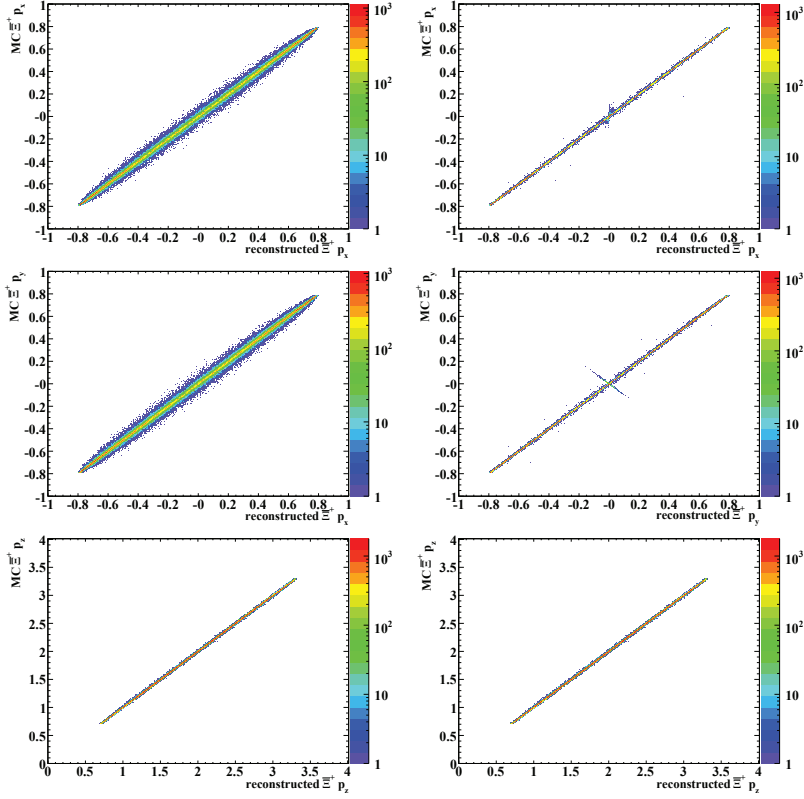


Figure 6.7: Reconstructed Ξ^+ momentum versus Monte Carlo truth in x , y and z direction, before (left) and after (right) the correction for the bending in the magnetic field, for the $\bar{p}p \rightarrow \Xi^+ \Xi^-$ reaction.

main reason, except for particles lost in the beam pipes, is that pions with momentum under 50 MeV/c spiral in the detector without reaching the STT, with the result that these events are not reconstructable. The effect is apparent in figure 6.10, where the momentum distributions of pions from the Monte Carlo truth are compared to those of the reconstructed events, for pions originating both from the Ξ and Λ decays. It is clearly seen that low momentum pions are not reconstructed. The non-isotropic reconstruction efficiencies are therefore explained by the fact that certain decay angles in the Ξ rest systems give rise a larger fraction of slow pions.

6.2.10 Comparison Between the Methods for Calculation of Spin Variables

As described in chapter 5, there are two different ways of dealing with the non-isotropic reconstruction efficiency: with and without the use of Monte Carlo

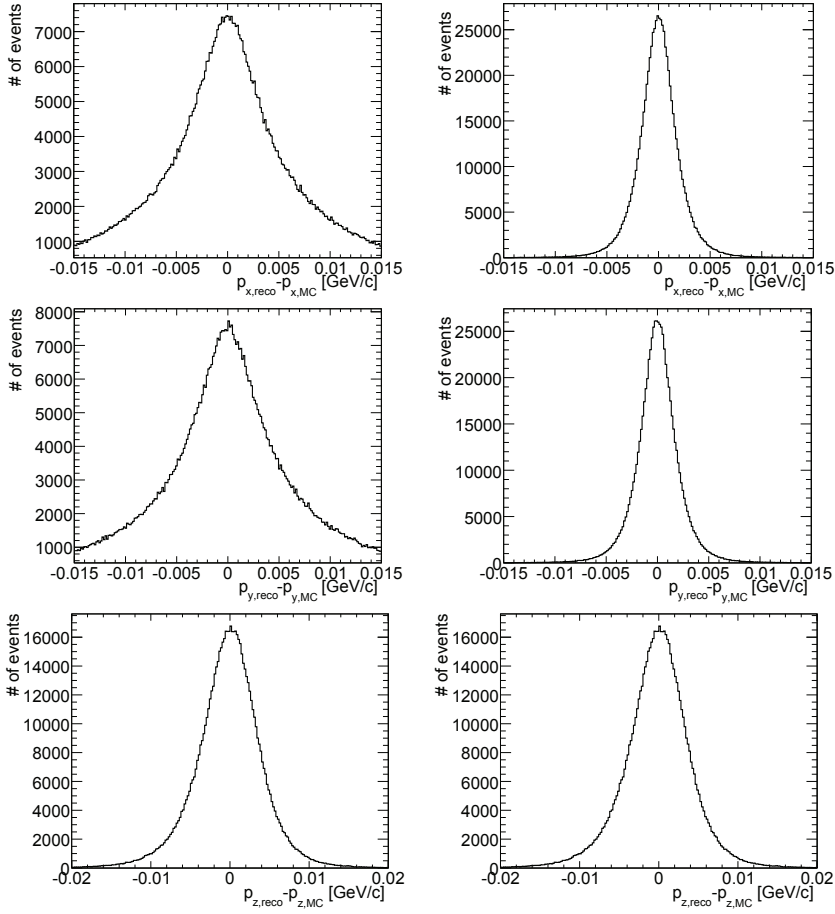


Figure 6.8: The difference between reconstructed Ξ^+ momentum and Monte Carlo truth in x, y and z direction, before (left) and after (right figures) the correction for the bending in the magnetic field, for the $\bar{p}p \rightarrow \Xi^+ \Xi^-$ reaction.

based acceptance functions. At a first glance, the reconstruction efficiency in the y direction of figure 6.9 looks promising. It is almost symmetric around $k_y = 0$. It should therefore be possible to calculate the spin variables without the use of the acceptance functions.

Using the method with Monte Carlo based acceptance functions the sum in eq.(5.18) was taken over the directional cosine vectors, \hat{k} , of the approximately $7.3 \cdot 10^5$ reconstructed events. The spin variables were reconstructed separately in ten intervals of $\cos \theta_{\Xi, CM}$. The corresponding acceptance functions were also generated using Monte Carlo data. In each angle interval both one dimensional, with 10 bins used for the reconstruction of polarisation, and two dimensional acceptance functions, with 5x5 bins used for reconstruction of spin variables, were generated. The obtained spin variables are shown in

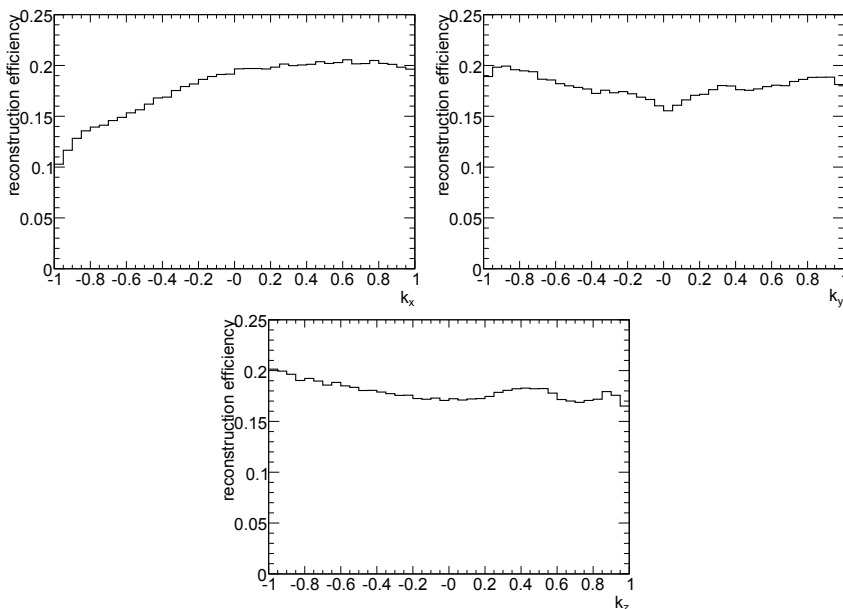


Figure 6.9: Reconstruction efficiency of the $\bar{p}p \rightarrow \bar{\Xi}^+ \Xi^-$ reaction as a function of the Λ decay angle in x , y and z direction of the Ξ^- rest system.

figure 6.11 (polarisation) and figure 6.12 (spin correlations) with the functions used as input for the simulations indicated with a solid line. The errors in the spin variables are the statistical errors calculated from eq.(5.6). The errors in the acceptance functions are not included. To propagate these errors to the spin variables, the effect of the error in each bin of the acceptance function on the spin variables would be needed. This effect is not possible to obtain for the calculation, since different terms in the sums of eq.(5.18) includes different bins of the acceptance function. It can be seen that the agreement between input and reconstructed values in figure 6.11 and figure 6.12 is very good.

For the simulations it is not completely satisfactory, having to correct the spin variables using acceptance functions which were also generated from Monte Carlo data. Once PANDA is running, experimental data can be used to test the acceptance functions. Fortunately, there is a way to test the method for reconstructing spin variables based on acceptance functions already in the simulations. As shown in section 5.4, the spin variables can be calculated from eq.(5.26), taking averages over combinations of the different components of the \hat{k} vectors from the reconstructed events. The result is shown in figure 6.13 (polarisation) and figure 6.14 (spin correlations). The statistical errors of the spin variables were in this case calculated from the errors in expectation values obtained from eq.(5.27). Since no acceptance functions were used in the reconstruction of these spin variables, there is no problem with the inclusion of

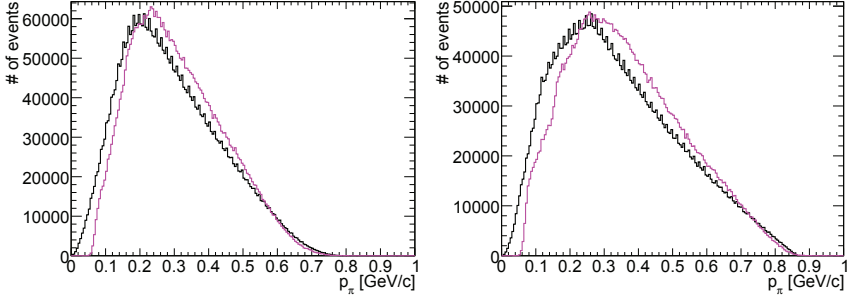


Figure 6.10: The Monte Carlo truth distribution of pion momenta (purple line) and reconstructed events (black line) for the $\bar{p}p \rightarrow \Xi^+\Xi^-$ reaction normalised to the same area. The left figure shows the distributions for pions that come from the Λ decay and the right figure shows the distributions for pions that come from the Ξ decay.

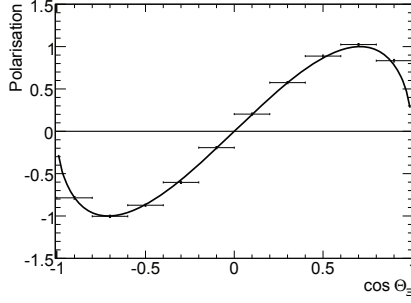


Figure 6.11: Ξ polarisation as a function of CM production angle of Ξ^+ in the y direction, reconstructed with the use of acceptance functions. The Ξ polarisation is taken to be the average of the polarisation of Ξ^+ and Ξ^- . The black line shows the input polarisation function for the simulations.

their errors. However, it must be remembered that approximations were made in the derivation of eq.(5.26) and that it only holds if the reconstruction efficiency in the y direction is symmetric around $k_y = 0$. Comparing figure 6.13 and figure 6.14 with figure 6.11 and figure 6.12, it is seen that the two methods give similar results. This is clear indication that it should be safe to use either method.

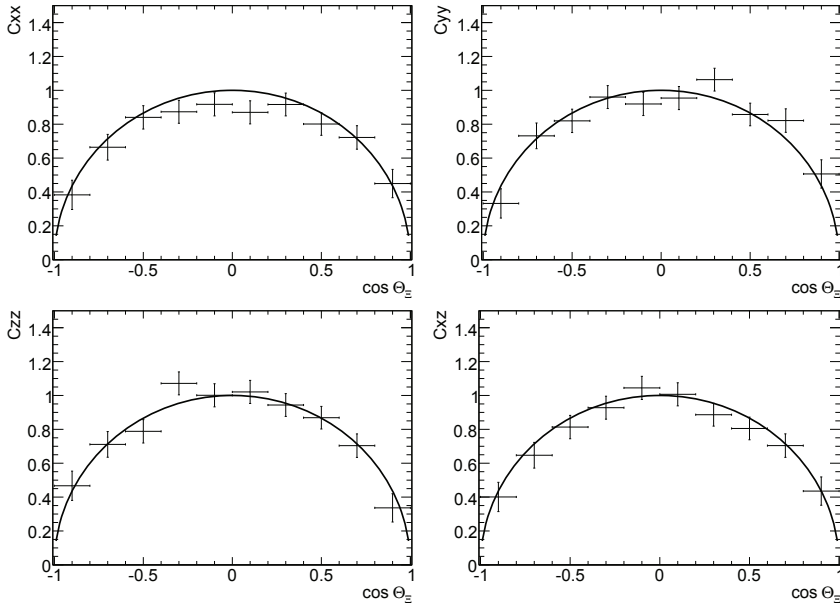


Figure 6.12: Spin correlations as a function of CM production angle of Ξ^+ , reconstructed with the use of acceptance functions. The correlation between the x and z direction is taken to be the average of C_{xz} and C_{zx} . The black lines show the input spin correlation functions for the simulations.

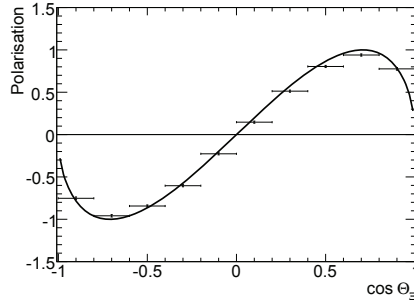


Figure 6.13: Ξ polarisation as a function of CM production angle of Ξ^+ in the y direction, reconstructed without the use of acceptance functions. The Ξ polarisation is taken to be the average of the polarisation of Ξ^+ and Ξ^- . The black line shows the input polarisation function for the simulations.

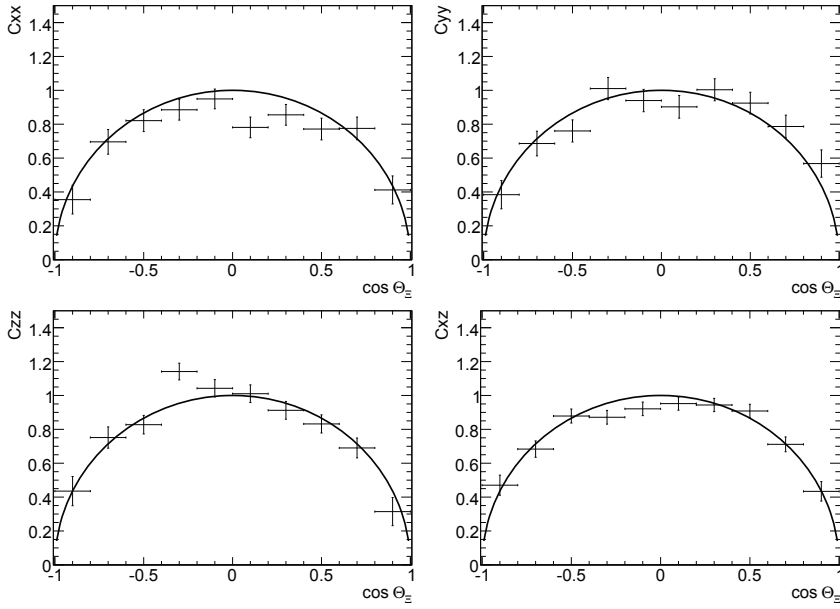


Figure 6.14: Spin correlations as a function of CM production angle of Ξ^+ , reconstructed without the use of acceptance functions. The correlation between the x and z direction is taken to be the average of C_{xz} and C_{zx} . The black lines show the input spin correlation functions for the simulations.

6.3 The $\bar{p}p \rightarrow \bar{\Omega}^+\Omega^-$ Reaction

6.3.1 Data Generation

The cross section for the $\bar{p}p \rightarrow \bar{\Omega}^+\Omega^-$ reaction is assumed to be very small, see section 4.2.2. Therefore only $1 \cdot 10^5$ events were generated, to see what can be reconstructed from a comparatively small amount of data. The beam momentum was 12 GeV/c. The hyperons were set to decay according to $\Omega^- \rightarrow \Lambda K^-$ and $\Lambda \rightarrow p\pi^-$. There is no experimental information for this reaction. Since all quarks are annihilated in this reaction, the differential cross section can be expected to be close to isotropic. The events were therefore generated with an isotropic cross section.

The polarisation and asymmetry parameters were applied using weights, according to eq.(3.36) and eq.(3.44). The polarisation parameters r_0^2 , r_1^2 and r_2^2 have $\frac{1}{\sqrt{3}}$ as their maximum value. The function $\frac{1}{\sqrt{3}} \sin \Theta_{\bar{\Omega}^+}$ was therefore used as input for these parameters. The same function was used for the linear combination $L = \sqrt{\frac{3}{5}}r_{-1}^1 + \frac{3}{2\sqrt{10}}r_{-1}^3$. Two options were used for the angle ϕ which determines the relation between β and γ . Either this angle was assumed to be zero in accordance with T invariance or no such initial assumption was made and the angle was set to 45° to see if this could be reconstructed.

6.3.2 Event Reconstruction

As for $\bar{p}p \rightarrow \bar{\Xi}^+\Xi^-$ reaction, also the $\bar{p}p \rightarrow \bar{\Omega}^+\Omega^-$ has four displaced vertices, which puts strict constraints on background. Thus, neither for this reaction strict requirements on PID probabilities were used. The particles in the final state are in this case protons and kaons. For the protons the VeryLoose candidate list was used and the ChargedTracks list was used for kaons. Using particle candidates from these lists the reconstruction was done according to the following steps:

- Identified pairs of antiprotons (protons) and π^+ (π^-) were fitted to a common vertex under a $\bar{\Lambda}$ (Λ) hypothesis, requiring a χ^2 probability > 0.001 .
- The invariant $\bar{p}\pi^+$ ($p\pi^-$) mass window was set to $1.110 \text{ GeV}/c^2 \leq M_\Lambda \leq 1.120 \text{ GeV}/c^2$.
- Pairs of $\bar{\Lambda}$ (Λ) and k^+ (k^-) were fitted to a common vertex under a $\bar{\Omega}^+$ (Ω^-) hypothesis, requiring a χ^2 probability > 0.001 .
- The invariant $\bar{\Lambda}k^+$ (Λk^-) mass window was set to $1.66 \text{ GeV}/c^2 \leq M_\Omega \leq 1.68 \text{ GeV}/c^2$.
- The remaining events were fitted to the $\bar{p}p \rightarrow \bar{\Omega}^+\Omega^-$ hypothesis, requiring a χ^2 probability > 0.001 .

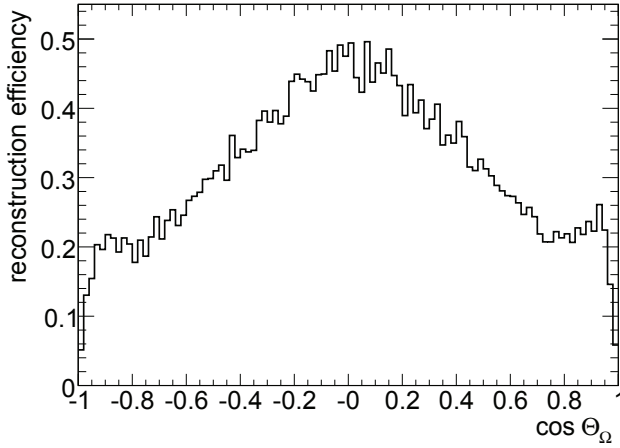


Figure 6.15: The reconstruction efficiency dependence on the CM production angle of $\bar{\Omega}^+$ in the $\bar{p}p \rightarrow \bar{\Omega}^+\Omega^-$ reaction at a beam momentum of 12 GeV/c.

6.3.3 Reconstruction Efficiency and Background

An overall efficiency of 0.30 was obtained, using the conditions above. The expected number of reconstructed events can be calculated in a similar way to eq.(6.4). The Ω hyperon does not always decay into ΛK , but has a branching ratio for $\Omega \rightarrow \Lambda K$ of 0.68 [95], which must also be included. The cross section of the reaction has never been measured, but there is a theoretical estimate of 2 nb. Using this value the expected number of reconstructed events becomes

$$0.30 \cdot \mathcal{L} \sigma \text{BR}(\Omega \rightarrow \Lambda K)^2 \text{BR}(\Lambda \rightarrow p\pi)^2 \approx 80 \text{ events/hour} \quad (6.7)$$

As expected the event rate is much smaller than for $\bar{p}p \rightarrow \bar{\Xi}^+\Xi^-$, but it is still possible to get reasonable amount of data.

The four displaced vertices should make the problem with background small. Since no particle identification was used for the kaons, the final state of the $\bar{p}p \rightarrow \bar{\Omega}^+\Omega^-$ reaction can not be separated from the final state of the $\bar{p}p \rightarrow \bar{\Xi}^+\Xi^-$ reaction. If the pions are taken as kaons in the $\bar{p}p \rightarrow \bar{\Xi}^+\Xi^-$ reaction the reconstructed mass of the Ξ hyperons would be higher. This mass can be calculated to be 1.56 GeV/c², which is still far away from the Ω mass, considering that the typical resolution of the invariant masses is a few MeV/c². However, there are some Σ resonances which are close in mass and have large widths which can decay to $\Lambda\pi$, *e.g.* $\Sigma(1670)$ and $\Sigma(1775)$ with branching ratios to $\Lambda\pi$ in the order of 10-20% [95]. The cross sections for producing the Σ resonances are not known, which makes it difficult to estimate their contribution to the background.

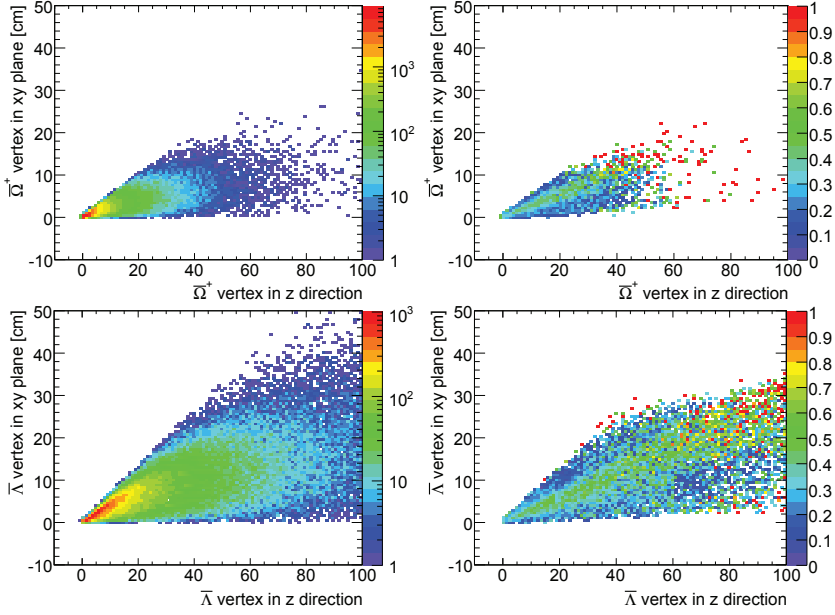


Figure 6.16: Decay vertex distributions of the $\bar{\Omega}^+$ (upper figures) and $\bar{\Lambda}$ (lower figures) hyperon for the $\bar{p}p \rightarrow \bar{\Omega}^+\Omega^-$ reaction at a beam momentum of 12 GeV/c. The Monte Carlo truth distributions are shown in the left figures and the reconstruction efficiency dependencies on decay vertex are shown in the right figures.

6.3.4 Reconstruction Efficiency as a Function of the $\bar{\Omega}^+$ Production Angle

Figure 6.15 shows the reconstruction efficiency as a function of the $\bar{\Omega}^+$ CM production angle. It is seen that the reconstruction efficiency is larger in the region of $\cos\Theta_{\Omega} \approx 0$, *i.e.* when the Ω hyperon is emitted perpendicularly to the beam axis in the CM frame. This effect was not seen for the $\bar{p}p \rightarrow \bar{\Xi}^+\Xi^-$ reaction. The reason for its appearance for the $\bar{p}p \rightarrow \bar{\Omega}^+\Omega^-$ reaction is the higher beam momentum. In order not to have too small emittance angles due to the large forward boost and loose particles in the beam pipe, there should be a large momentum transverse to the beam pipe. The problem with asymmetry from PID is not present at this high beam momentum. The efficiency is non-zero for all angles also for this process, so that differential cross section and polarisation parameters can be reconstructed over the full angular range.

6.3.5 Reconstruction of Decay Vertices

The position of the decay vertices of the $\bar{\Omega}^+$ and the daughter Λ particles are shown in figure 6.16. The Ω^- hyperon has a shorter lifetime than the Ξ^- hyperon, which means that it decays closer to the interaction point. Even with

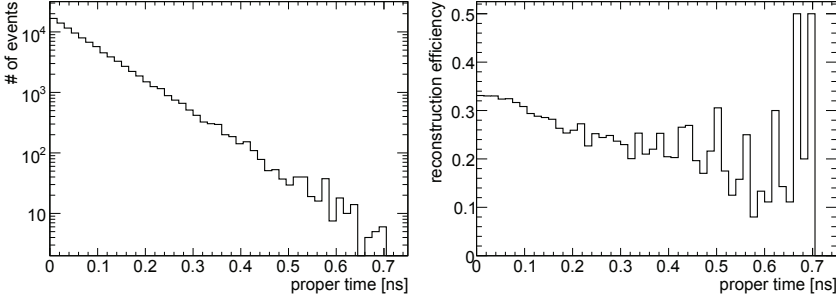


Figure 6.17: Reconstructed proper lifetime of Ω^- corrected for acceptance (left) and the reconstruction efficiency dependence on lifetime (right).

the higher beam momentum for this case, figure 6.16 shows that the daughter Λ hyperons go considerably shorter before they decay than for the $\bar{p}p \rightarrow \bar{\Xi}^+ \Xi^-$ case. The reconstruction efficiency dependence on position of decay vertices is shown in the same figure, and the same behaviour as for $\bar{p}p \rightarrow \bar{\Xi}^+ \Xi^-$ is noticed, *i.e.* the reconstruction efficiency decreases for small and large angles.

6.3.6 Ω^- Lifetime Reconstruction

As for the Ξ^- hyperon, the lifetime $\tau = \frac{1}{\lambda}$ of the Ω^- hyperon can be deduced from the decay law

$$N(t) = N_0 e^{-\lambda t} \quad (6.8)$$

with the time taken to be the proper time of the hyperons. As for the Ξ^- hyperon, the difference in reconstruction efficiency for different decay times has to be corrected. Figure 6.17 shows how the reconstruction efficiency depends on the Ω^- proper time before decay and the time distribution corrected for the difference in reconstruction efficiency. Fitting an exponential function in the interval between $t = 0.1$ and $t = 0.4$ ns, an Ω^- lifetime of 0.0826 ± 0.0004 ns is obtained. The agreement with the established tabulated value of 0.0821 ± 0.0011 ns [95] is very good.

6.3.7 Invariant Mass

The reconstructed invariant masses of $\bar{\Omega}^+$ and $\bar{\Lambda}$ are shown in figure 6.18. Fitting the two histograms with Gaussians gives a σ of $2.2 \text{ MeV}/c^2$ and $1.7 \text{ MeV}/c^2$, respectively. The σ for the $\bar{\Lambda}$ mass is comparable to the $\bar{p}p \rightarrow \bar{\Xi}^+ \Xi^-$ case.

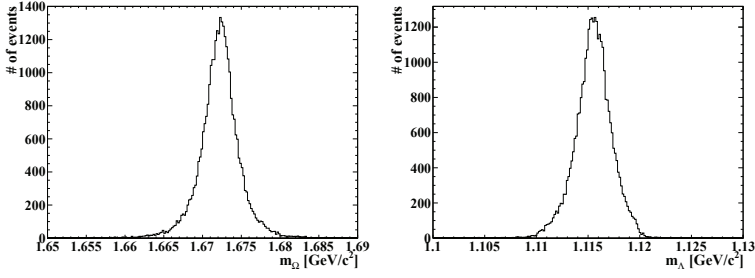


Figure 6.18: Reconstructed invariant mass of $\bar{\Omega}^+$ (left) and $\bar{\Lambda}$ (right).

6.3.8 Reconstruction of Polarisation and Asymmetry Parameters

Since the Ω^- hyperon is charged, it is bent by the magnetic field. Before the polarisation parameters can be reconstructed this must therefore be corrected for. The same method to correct for the magnetic field that was used for the $\bar{p}p \rightarrow \bar{\Xi}^+\Xi^-$ reaction was used for this reaction, even though the effect is smaller here due to the shorter lifetime of Ω^- .

In sections 3.1.3.2 and 5.2 it was shown how three of the non-zero Ω polarisation parameters, r_{20} , r_{22} and r_{21} , can be deduced from the angles of its decay Λ hyperons. Eq.(5.8) was used to calculate these parameters, in ten angular intervals of $\cos \theta_{\Omega,CM}$. One-dimensional acceptance functions with ten bins, generated using Monte Carlo data, in each angle interval were used for corrections. The obtained polarisation parameters are shown in figure 6.19. The errors in the spin variables are the statistical errors calculated from eq.(5.10). It can be seen that the agreement between input and reconstructed values in figure 6.19 is very good.

Additional information can be extracted from the subsequent decay of the daughter Λ hyperon, see section 3.1.3.4. The expression for the angular distribution in this decay, given in eq.(3.44), involves the linear combination of polarisation parameters $L = \sqrt{\frac{3}{5}}r_{-1}^1 + \frac{3}{2\sqrt{10}}r_{-1}^3$, as well as the asymmetry parameters β and γ . These asymmetry parameters have not been measured for the Ω hyperon. However, from T invariance and no final state interactions it can be concluded that $\beta \approx 0$. Two different strategies for the reconstruction of variables from this decay were therefore considered. The expressions for reconstructing the parameters in for these two cases were deduced in section 5.2.

As a first option β was assumed to be zero. In this case, the angular distribution is only non-isotropic in the y direction of the Ω rest system, where the slope is given by $\alpha_\Lambda \gamma L$. The slope is only given up to a sign, since $\gamma^2 = 1$. For the investigation of the ability to reconstruct L , $\gamma = 1$ was used as input and then assumed in the reconstruction. The linear combination L was calcu-

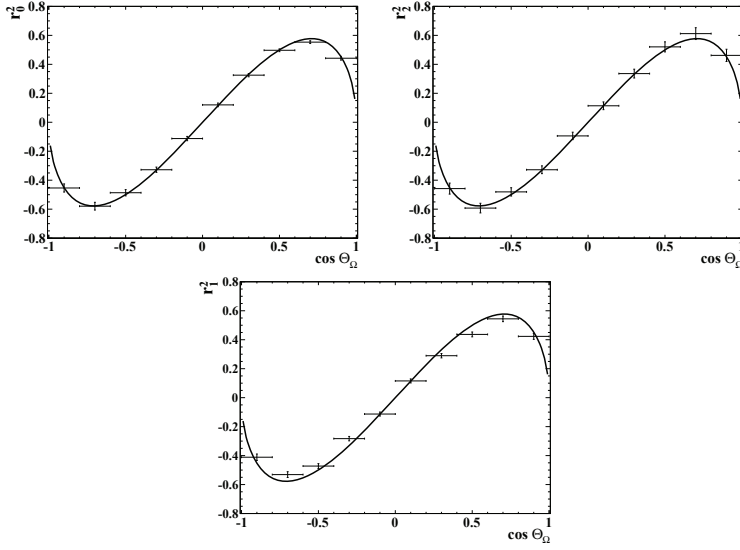


Figure 6.19: Ω polarisation parameters r_{20} , r_{22} and r_{21} as a function of CM production angle of $\bar{\Omega}^+$, reconstructed with the use of acceptance functions. The Ω polarisation parameters are taken to be the average of the parameters for $\bar{\Omega}^+$ and Ω^- . The black lines show the input polarisation parameter functions for the simulations.

lated from eq.(5.16) in ten angular intervals of $\cos \theta_{\Omega,CM}$. One-dimensional acceptance functions with ten bins, generated using Monte Carlo data, in each angle interval were used for corrections. The result is shown in figure 6.20. The value of L is reconstructed reasonably well in this case, but it should be remember that the sign of L can not be given from the measurement.

The second option is to make no initial assumption for the value of the angle ϕ , which relates α and β through $\tan \phi = \frac{\beta}{\gamma}$. In this case, both the value of $\tan \phi$ and the linear combination squared L^2 can be reconstructed, using eq.(5.12) and eq.(5.13). To see if a non-zero value of ϕ could be reconstructed, it was set to 45° as input. The values were reconstructed with the same acceptance functions as for the previous case. The reconstructed values of L^2 are shown in figure 6.21, were the agreement with the input function is again reasonably good. Since only L^2 is reconstructed, also in this case the value of L is only measured up to a sign. The reconstructed value of $\tan \phi$ was 0.949 ± 0.035 , close to the input value of 1.

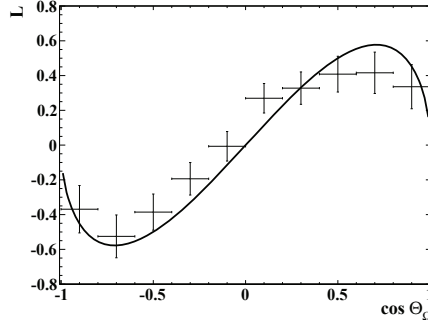


Figure 6.20: The linear combination L as a function of CM production angle of $\bar{\Omega}^+$, reconstructed with the use of acceptance functions. The ϕ is set to be 0° for this reconstruction. The value of L for Ω is taken to be the average of the value for $\bar{\Omega}^+$ and Ω^- . The black line shows the input function for the simulations.

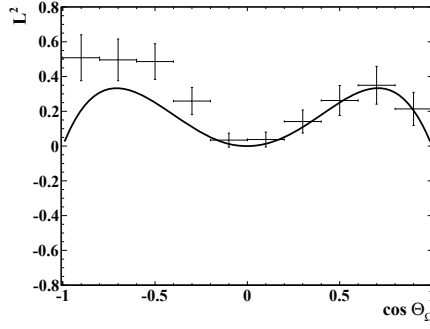


Figure 6.21: The linear combination squared L^2 as a function of CM production angle of $\bar{\Omega}^+$, reconstructed with the use of acceptance functions. The ϕ is set to be 45° for this reconstruction. The value of L^2 for Ω is taken to be the average of the value for $\bar{\Omega}^+$ and Ω^- . The black line shows the input function for the simulations.

6.4 The $\bar{p}p \rightarrow \bar{\Lambda}_c^- \Lambda_c^+$ Reaction

6.4.1 Data Generation

Theoretical calculations of the cross section for the $\bar{p}p \rightarrow \bar{\Lambda}_c^- \Lambda_c^+$ reaction predict it to be up to 50 times higher than for the $\bar{p}p \rightarrow \bar{\Omega}^+ \Omega^-$ reaction [104, 105, 106, 108]. The problem with the Λ_c^+ hyperon is that it can decay to very many different final states, none of which has a branching ratio of more than a few percent. The branching ratio for the decay of interest for measuring spin variables, $\Lambda_c^+ \rightarrow \Lambda \pi^+$, is only 1% [95]. Since a low number of events with the right decay is expected, $1 \cdot 10^5$ events were generated for this reaction as well, at a beam momentum of 12 GeV/c. The hyperons were set to decay according to $\Lambda_c^+ \rightarrow \Lambda \pi^+$ and $\Lambda \rightarrow p \pi^-$.

The spin variables were set to the same functions as for $\bar{p}p \rightarrow \bar{\Xi}^+ \Xi^-$

$$\begin{aligned} P_{\bar{\Lambda}_c^-, y} &= P_{\Lambda_c^+, y} = \sin 2\Theta_{\bar{\Lambda}_c^-} \\ C_{\bar{x}, x} &= C_{\bar{y}, y} = C_{\bar{z}, z} = C_{x, z} = \sin \Theta_{\bar{\Lambda}_c^-} \end{aligned} \quad (6.9)$$

6.4.2 Reconstruction

The reconstruction of the $\bar{p}p \rightarrow \bar{\Lambda}_c^- \Lambda_c^+$ events was done in a similar way as for the previous reactions. The particles in the final state are in this case protons and pions. For the protons the VeryLoose candidate list was used and the ChargedTracks list was used for pions. Using particle candidates from these lists the reconstruction was done according to the following steps:

- Identified pairs of antiprotons (protons) and π^+ (π^-) were fitted to a common vertex under a $\bar{\Lambda}$ (Λ) hypothesis, requiring a χ^2 probability > 0.001 .
- The invariant $\bar{p}\pi^+$ ($p\pi^-$) mass window was set to $1.110 \text{ GeV}/c^2 \leq M_{\Lambda} \leq 1.120 \text{ GeV}/c^2$.
- Pairs of $\bar{\Lambda}$ (Λ) and π^- (π^+) were fitted to a common vertex under a $\bar{\Lambda}_c^-$ (Λ_c^+) hypothesis, requiring a χ^2 probability > 0.001 .
- The invariant $\bar{\Lambda}\pi^-$ ($\Lambda\pi^+$) mass window was set to $2.27 \text{ GeV}/c^2 \leq M_{\Lambda_c} \leq 2.30 \text{ GeV}/c^2$.
- The remaining events were fitted to the $\bar{p}p \rightarrow \bar{\Lambda}_c^- \Lambda_c^+$ hypothesis, requiring a χ^2 probability > 0.001 .

6.4.3 Reconstruction Efficiency and Background

Using the conditions outlined above an overall reconstruction efficiency of 0.35 was obtained. This is slightly higher than for $\bar{p}p \rightarrow \bar{\Omega}^+ \Omega^-$. With a 50 times higher cross section one could think that this would mean a higher rate of reconstructable events. However, the branching ratio for $\Lambda_c^+ \rightarrow \Lambda \pi^+$ of only 1% comes in squared when calculating the expected event rate, since both Λ_c hyperons have to have the right decay. Combining these numbers gives

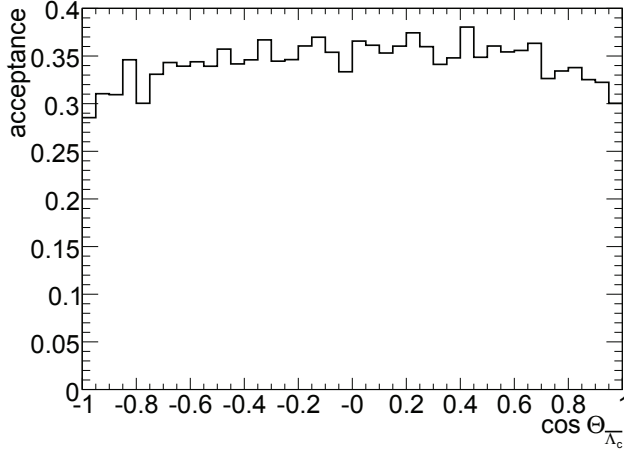


Figure 6.22: The reconstruction efficiency dependence on the CM production angle of $\bar{\Lambda}_c^-$ in the $\bar{p}p \rightarrow \bar{\Lambda}_c^- \Lambda_c^+$ reaction at a beam momentum of 12 GeV/c.

$$0.35 \cdot \mathcal{L} \sigma \text{BR}(\Lambda_c \rightarrow \Lambda \pi)^2 \text{BR}(\Lambda \rightarrow p \pi)^2 \approx 25 \text{ events/day} \quad (6.10)$$

Thus, even though the cross section is larger, the very small branching ratio for $\Lambda_c^+ \rightarrow \Lambda \pi^+$ means that the event rate for $\bar{p}p \rightarrow \bar{\Lambda}_c^- \Lambda_c^+$ will be much smaller than for $\bar{p}p \rightarrow \bar{\Omega}^+ \Omega^-$.

The background situation is a bit different from the $\bar{p}p \rightarrow \bar{\Omega}^+ \Omega^-$ reaction, in the sense that the Λ_c^+ hyperons decay very close to the interaction point. Therefore only the decay vertices of the daughter Λ hyperons can be considered to be displaced. In this case the resonances $\Sigma(2030)$ and $\Sigma(2250)$ can give rise to background, when they decay into $\Lambda \pi$, but their cross sections are not known. More work to clarify the background situation is needed.

6.4.4 Acceptance as a Function of the $\bar{\Lambda}_c^-$ Production Angle

The reconstruction efficiency as a function of the CM production angle of $\bar{\Lambda}_c^-$, is shown in figure 6.22. Since the Λ_c^+ hyperon decays almost directly after it is produced, its production angle is not expected to have much influence the reconstruction efficiency. This is also what is seen in figure 6.22, where the efficiency distribution is almost isotropic. Spin variables can be reconstructed over the full angle interval since the reconstruction efficiency is non-zero for all values of $\cos \Theta_{\bar{\Lambda}_c^-}$.

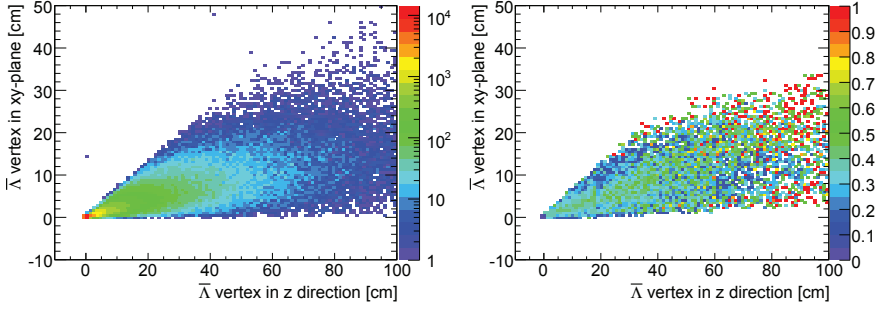


Figure 6.23: Decay vertex distributions of the daughter $\bar{\Lambda}$ hyperon in the $\bar{p}p \rightarrow \bar{\Lambda}_c^- \Lambda_c^+$ reaction at a beam momentum of 12 GeV/c. The Monte Carlo truth distribution is shown in the left figure and the reconstruction efficiency dependence on decay vertex is shown in the right figure.

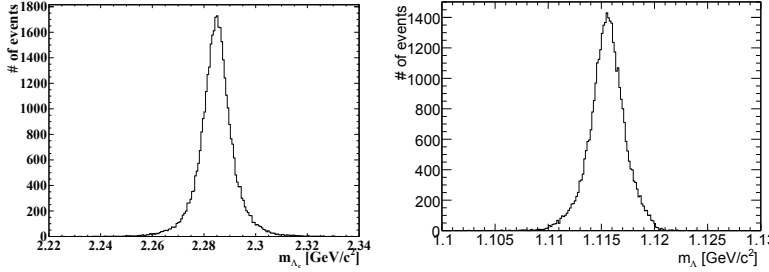


Figure 6.24: Reconstructed invariant mass of $\bar{\Lambda}_c^-$ (left) and $\bar{\Lambda}$ (right).

6.4.5 Reconstruction of Decay Vertices

The Λ_c^+ hyperon has a very short lifetime, $c\tau = 6.0 \cdot 10^{-5}$ m [95], and decays very close to the interaction point. Therefore the vertices of the daughter Λ hyperons, shown in figure 6.23, are much closer to the interaction point than for the $\bar{p}p \rightarrow \bar{\Omega}^+ \Omega^-$ reaction at the same beam momentum. The reconstruction efficiency dependence on position of the daughter $\bar{\Lambda}$ decay vertices is shown in the same figure, and the same behavior as for the other reactions is observed, *i.e.* the reconstruction efficiency decreases for small and large angles.

6.4.6 Invariant Mass

The reconstructed invariant masses of $\bar{\Lambda}_c^-$ and $\bar{\Lambda}$ are shown in figure 6.24. Fitting the two histograms with Gaussians gives a σ of 5.9 MeV/c² and 1.6 MeV/c², respectively. The σ for the $\bar{\Lambda}$ mass is comparable to the other two reactions.

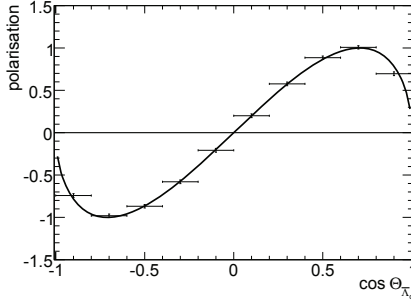


Figure 6.25: Λ_c polarisation as a function of CM production angle of $\bar{\Lambda}_c^-$ in the y direction, reconstructed with the use of acceptance functions. The Λ_c polarisation is taken to be the average of the polarisation of $\bar{\Lambda}_c^-$ and Λ_c^+ . The black lines show the input polarisation function for the simulations.

6.4.7 Reconstruction of Spin Variables

The very low expected event rate will make it difficult to reconstruct spin variables. A positive thing though, is that the asymmetry parameter for Λ_c^+ is large, $\alpha = -0.91$ [95]. The number of events needed to reconstruct the polarisation and spin correlations reasonably well is therefore not very large. Polarisation and spin correlations were reconstructed, using the method with acceptance function for corrections. Both one dimensional, with 10 bins used for the reconstruction of polarisation, and two dimensional acceptance functions, with 5×5 bins used for reconstruction of spin variables, were generated for the ten angle intervals. The spin variables were then calculated using eq.(5.18). The results are shown in figure 6.25 (polarisation) and figure 6.26 (spin correlations) with the functions used as input for the simulations indicated with a solid line. The errors in the spin variables are the statistical errors calculated from eq.(5.6). As seen the values are very well reconstructed from the approximately $3.5 \cdot 10^4$ reconstructed events.

6.4.8 Other Charmed Hyperons

Can PANDA provide data for $\bar{p}p \rightarrow \bar{Y}Y$ reactions with heavier charmed hyperons? The threshold beam momenta for the $\bar{p}p \rightarrow \bar{\Xi}_c \Xi_c$ and $\bar{p}p \rightarrow \bar{\Omega}_c \Omega_c$ reactions are 12.0 GeV/c and 14.6 GeV/c, respectively, so they are energetically accessible at PANDA. There are no theoretical predictions for the cross sections of these reactions. In a naive assumption, the cross sections would be suppressed by a factor of α_s^2 for the first reaction and α_s^4 for the second, with respect to the cross section for the $\bar{p}p \rightarrow \bar{\Lambda}_c^- \Lambda_c^+$. At the relevant energy scale, the value of the strong coupling constant is about 1/5, which means

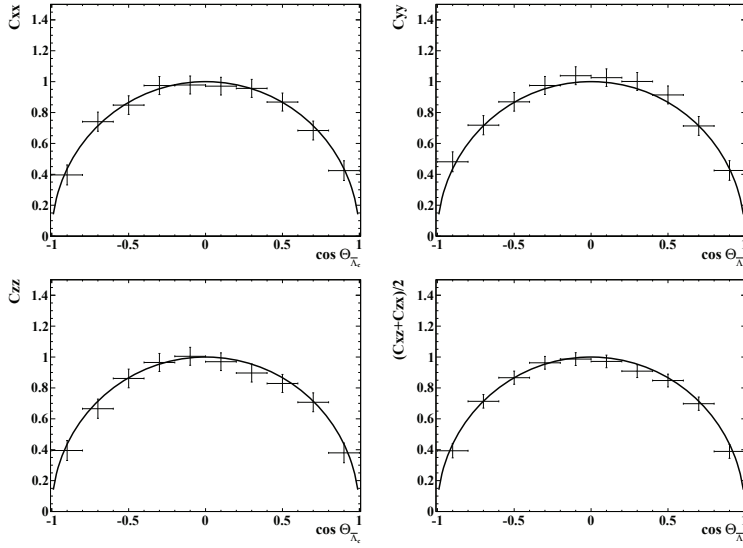


Figure 6.26: Spin correlations as a function of CM production angle of $\bar{\Lambda}_c^-$, reconstructed with the use of acceptance functions. The correlation between the x and z direction is taken to be the average of C_{xz} and C_{zx} . The black lines show the input spin correlation functions for the simulations.

suppression factors of $1/25$ and $1/625$ for the two reactions². Branching ratios for the decays of Ξ_c and Ω_c are not known. Considering the expected rate of reconstructed events of 25 per day for $\bar{p}p \rightarrow \bar{\Lambda}_c^- \Lambda_c^+$, maybe a few events for $\bar{p}p \rightarrow \bar{\Xi}_c \Xi_c$ can be collected, whereas the prospects for $\bar{p}p \rightarrow \bar{\Omega}_c \Omega_c$ are not very promising.

²There is one theoretical calculation [134] which predicts the cross section for $\bar{p}p \rightarrow \bar{\Xi}_c \Xi_c$ to be considerably closer to the cross section for $\bar{p}p \rightarrow \bar{\Lambda}_c^- \Lambda_c^+$

6.5 CP Violation in Hyperon Decay

6.5.1 General Experimental Considerations

In $\bar{p}p \rightarrow \bar{Y}Y$ reactions it is possible to probe CP violation in hyperon decays. The hyperon CP violation parameters were defined in section 3.2 and related to up-down counting asymmetries in section 5.4. The statistical error in the CP violation parameter A is given by [72]

$$\sigma_A = \frac{1}{\alpha|P|} \sqrt{\frac{3}{2N}} \quad (6.11)$$

where N is the number of events. The PS185 experiment at LEAR performed CP violation tests for the $\bar{p}p \rightarrow \bar{\Lambda}\Lambda$ reaction at beam momenta in the range 1.5-1.7 GeV/c [75, 111], with an average value of the polarisation over the full production angle interval of 0.27. Using this value, a statistical error of 10^{-4} , which is in the vicinity of the theoretical predictions, would be reached for approximately $5 \cdot 10^9$ events. For PANDA the expected number of reconstructed $\bar{p}p \rightarrow \bar{\Lambda}\Lambda$ events at this beam momentum is about 700 per second [94]. A beam time of approximately 80 days, would then be sufficient to reach a statistical uncertainty of this order.

As seen in eq.(6.11), the error is inversely proportional to $\alpha|P|$. It is therefore not certain that it is advantageous to use all events. Rather, events in an interval of the hyperon production angle where the quantity $|P|\frac{d\sigma}{d\Omega}$ is maximized should be used.

It is very important to control the systematic errors in a measurement of the CP violation parameter A . The most important aspect of the detector is that its efficiency must be azimuthally symmetric. An inefficiency which is the same for all azimuthal angles can not fake a CP violation signal, since the important information is whether the final particles go up or down with respect to the production plane. The long decay lengths of the hyperons mean that the hyperon decays can occur far away from the beam axis. This, in turn, means that efficiency holes, which are not azimuthally symmetric, may not cancel from the fact that the production plane is arbitrarily oriented from event to event [72]. Another systematic error comes from the fact that particles and antiparticles interact differently with matter. This may cause problems if the result is that the reconstruction efficiency of the decay of the hyperon and the antihyperon differ. Also depolarising scattering may be different for hyperons and antihyperons.

6.5.2 Reconstruction of the CP Violation Parameter A for the $\bar{p}p \rightarrow \bar{\Lambda}\Lambda$ Reaction

To investigate the possibility to measure CP violation in the $\bar{p}p \rightarrow \bar{\Lambda}\Lambda$ reaction, $1 \cdot 10^6$ events were generated for a beam momentum of 1.64 GeV/c. The events

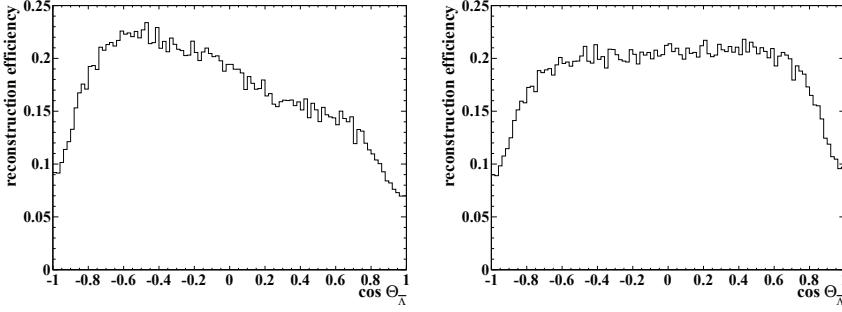


Figure 6.27: The reconstruction efficiency dependence on the CM angle of $\bar{\Lambda}$. In the left figure the VeryLoose list has been used for protons in the reconstruction. In the right figure the ChargedTracks list has been used for protons. For both figures the ChargedTracks list has been used for pions.

were generated with an isotropic differential cross section and the decay of Λ was set to be $\Lambda \rightarrow p\pi^-$. No CP violation and 100% polarisation was used as input. $1.72 \cdot 10^5$ out of the generated events were reconstructed. It was seen in section 6.2.4 that for the $\bar{p}p \rightarrow \bar{\Xi}^+\Xi^-$ reaction the reconstruction efficiency as a function of the $\bar{\Xi}^+$ production angle is not symmetric around $\cos \theta_{\Xi^+} = 0$. The same asymmetry is present for the $\bar{p}p \rightarrow \bar{\Lambda}\Lambda$ reaction, as seen in the left part of figure 6.27. This would not be the case if the hyperon and antihyperon are treated in the same way, since $\cos \theta_{\bar{\Lambda}} = -\cos \theta_{\Lambda}$. In section 6.2.4 it was also noted that this asymmetry disappeared if no PID criterium is used. This is also true for the $\bar{p}p \rightarrow \bar{\Lambda}\Lambda$ reaction, as shown in the right part of figure 6.27 for the $\bar{p}p \rightarrow \bar{\Lambda}\Lambda$ reaction. Since it is important for CP violation measurements that the detector response is the same for particles and antiparticles, it could be a good idea not to use any PID criterium for these measurements. If no PID is used for the reconstruction the number of reconstructed events increases slightly to $1.85 \cdot 10^5$.

The description of how one relates CP violation parameters to asymmetries of the number of emitted final state particles with respect to the opposite sides of the production plane of the hyperon was given in section 5.4. The parameter A can be related to the difference in the number of events between having positive or negative values of u , with u defined as

$$u = \frac{1}{2}(k_y + \bar{k}_y) \quad (6.12)$$

where k_y and \bar{k}_y are the projections of the decay direction on the y axis of the hyperon rest system which is perpendicular to the production plane. The reconstruction efficiency dependence in the k_y, \bar{k}_y plane is shown in figure 6.28. The important aspect is that the efficiency is symmetric around the $u = 0$ di-

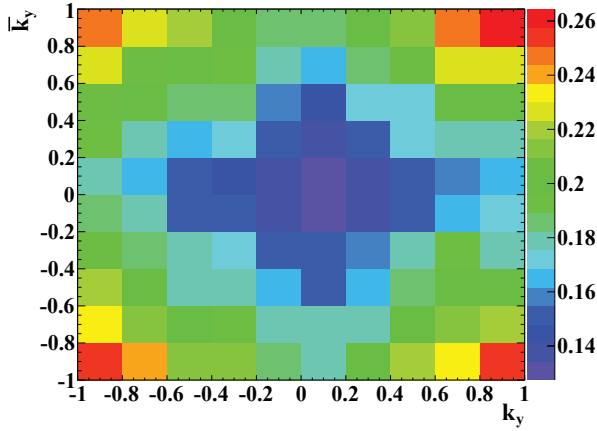


Figure 6.28: The reconstruction efficiency dependence in the $\hat{k}_y \hat{\bar{k}}_y$ plane for the $\bar{p}p \rightarrow \bar{\Lambda}\Lambda$ reaction.

agonal, which goes from the upper left to the lower right in figure 6.28. As seen in figure 6.28, this symmetry seems to be present.

The \dot{A} parameter was calculated from the reconstructed events with the result -0.0333 ± 0.0012 . This indicates that systematic errors gives rise to a false CP violation signal which is much larger than the statistical errors. A strategy to decrease systematic errors, both from detector asymmetries and depolarisation of the hyperons as they interact in the detector, is to only consider events where the hyperons decay close to the beam axis. Figure 6.29 shows the value of the \dot{A} parameter, calculated from reconstructed events where different limits on the maximum distance of the hyperon decays from the beam axis have been used. It can be seen that the values slowly approach zero with more stricter limits. If only events where the hyperons decays closer than 2 cm from the beam axis were considered, the extracted \dot{A} value became -0.0211 ± 0.0016 . 55% of the reconstructed events fulfills this requirement.

Still, a false CP violation signal much larger than the statistical errors is present. As already mentioned, another way to reduce systematic errors is to use no PID in the reconstruction, since this reconstructs particles and antiparticles differently. Figure 6.30 shows the \dot{A} parameter value calculated in the same way as in figure 6.29, but for events reconstructed using the ChargedTracks list for both protons and pions. In this case the value became -0.0147 ± 0.0012 if all events were used. The value approaches zero as a function of the strictness of the allowed maximum radial distance from the beam axis of the decays, as shown in figure 6.30. The false signal disappeared if only events where the hyperons decay closer than 2 cm from the beam axis were considered. In that case the value of \dot{A} was 0.0008 ± 0.0016 . Consequently, to reduce systematic errors in the measurement of this CP violation

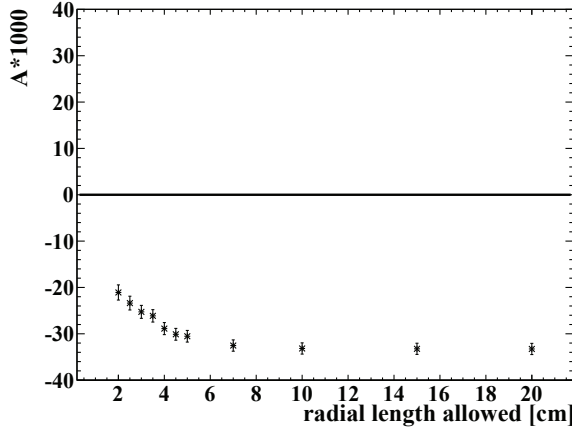


Figure 6.29: The calculated value of the \dot{A} parameter for the $\bar{p}p \rightarrow \bar{\Lambda}\Lambda$ reaction, as a function of the maximum radial length allowed from the beam axis to the hyperon decays. The VeryLoose list has been used for protons in the reconstruction.

parameter no PID should be used and only events where the hyperons decay closer than 2 cm from the beam axis should be considered. Another advantage of only considering events where the hyperons decay close to the beam axis is that a larger fraction of the hyperons will decay inside the vacuum of the beam pipe, which has a radius of 10 mm in the vicinity of the interaction point. This will decrease the risk for depolarising scattering of the hyperons before the decay.

6.5.3 Reconstruction of CP Violation Parameters for the $\bar{p}p \rightarrow \bar{\Xi}^+\Xi^-$ Reaction

For the $\bar{p}p \rightarrow \bar{\Xi}^+\Xi^-$ reaction, the two CP violation parameters A and B can be measured. $1 \cdot 10^6$ events were generated for a beam momentum of 4 GeV/c to study this. The events were generated with an isotropic differential cross section and the decay of the daughter Λ hyperon was set to be $\Lambda \rightarrow p\pi^-$. No CP violation and 100% polarisation was used as input. $1.96 \cdot 10^5$ events were reconstructed, if no PID was used in the reconstruction.

The A parameter is measured in the $k_y \bar{k}_y$ plane for the $\Xi \rightarrow \Lambda\pi$ decays, using the same method as for the $\bar{p}p \rightarrow \bar{\Lambda}\Lambda$ case. The reconstruction efficiency dependence in this $k_y \bar{k}_y$ plane is shown in figure 6.31. The reconstruction efficiency seems to be reasonably symmetric around the $u = 0$ diagonal.

The parameter B is measured in the $k_y \bar{k}_y$ plane for the subsequent $\Lambda \rightarrow p\pi$ decays. It was shown in section 5.4 that this parameter is related to the difference in the number of events between having positive or negative values of ν , with ν defined as

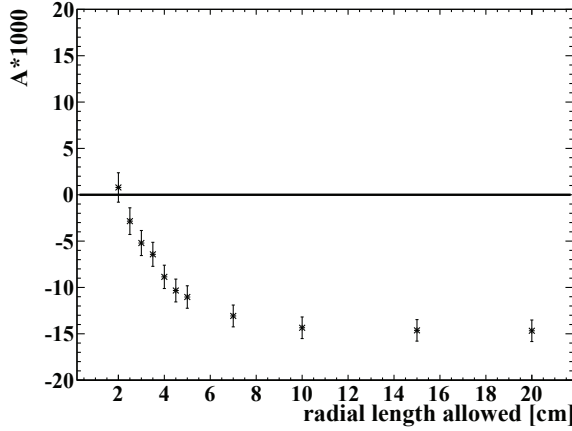


Figure 6.30: The calculated value of the \dot{A} parameter for the $\bar{p}p \rightarrow \bar{\Lambda}\Lambda$ reaction, as a function of the maximum radial length allowed from the beam axis to the hyperon decays. The ChargedTracks list has been used for protons in the reconstruction.

$$v = \frac{1}{2}(k_y - \bar{k}_y) \quad . \quad (6.13)$$

The reconstruction efficiency dependence in the $k_y - \bar{k}_y$ plane for the $\Lambda \rightarrow p\pi$ decays is shown in figure 6.32. The important aspect here is the symmetry around the $v = 0$ diagonal, which goes from the upper right to the lower left. As seen in figure 6.32, there is no such symmetry at all. This is not too surprising since the y axes in these reference systems are parallel to the beam axis. This means that the method of only considering events close to the beam axis has no effect. This asymmetry in reconstruction efficiency must therefore be compensated for by using acceptance functions, which will introduce more systematic errors. The measurement is, however, worth doing since there is no previous measurement of B_{Ξ^-} . The investigation in this thesis has been restricted to the A parameter, for which the required detector symmetry is almost present.

The \dot{A} parameter was calculated from the reconstructed events and the result was -0.0522 ± 0.0011 , when no PID was used in the reconstruction. This is a larger false CP violation signal than for the $\bar{p}p \rightarrow \bar{\Lambda}\Lambda$ reaction. The same method for making this false signal disappear that was used for the $\bar{p}p \rightarrow \bar{\Lambda}\Lambda$ reaction can also be used here. Figure 6.33 shows the value of the \dot{A} parameter, calculated from reconstructed events where different limits on the maximum distance of the hyperon decays from the beam axis have been used. As seen in this figure, the method works for this reaction as well. The false signal disappears if the limit is put to about 1-2 cm.

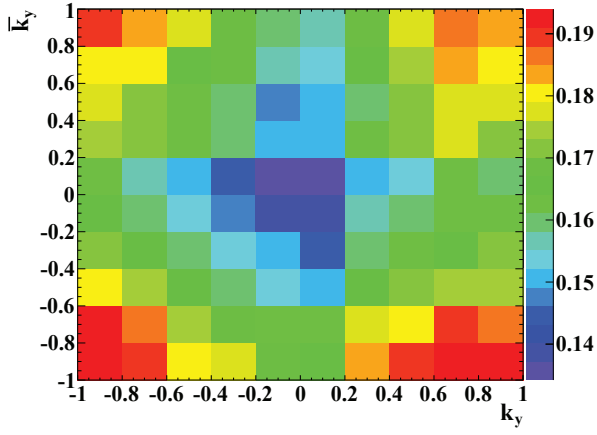


Figure 6.31: The efficiency dependence in the k_y \bar{k}_y plane of the $\Xi \rightarrow \Lambda \pi$ decays for $\bar{p}p \rightarrow \bar{\Xi}^+ \Xi^-$ reaction.

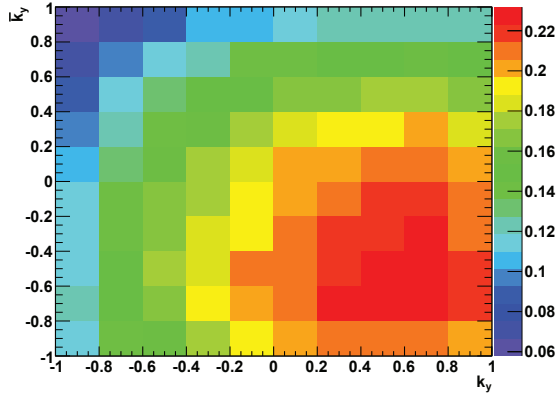


Figure 6.32: The reconstruction efficiency dependence in the k_y \bar{k}_y plane of the $\Lambda \rightarrow p \pi$ decays for $\bar{p}p \rightarrow \bar{\Xi}^+ \Xi^-$ reaction.

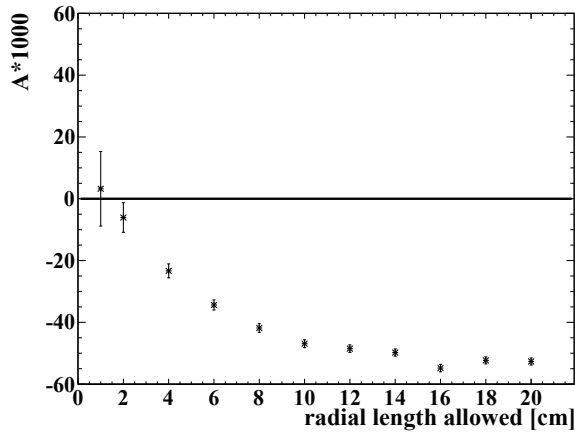


Figure 6.33: The calculated value of the \dot{A} parameter for the $\bar{p}p \rightarrow \bar{\Xi}^+\Xi^-$ reaction, as a function of the maximum radial length allowed from the beam axis to the hyperon decays. The ChargedTracks list has been used for protons in the reconstruction.

7. Precession of the Hyperon Polarisation Vector in the Magnetic Field of the PANDA Detector

As seen in previous sections, the polarisations and spin correlations of the hyperons are extracted from the angular asymmetry in their decay. However, due to their weak decay hyperons have a typical decay length of several cm. As they travel this distance through the detector, their polarisation vector is affected by the magnetic field. The measured spin variables can consequently differ from the spin variables in the production of the hyperons. The effect was noted in the report on measurements of CP-violation in hyperon decays at the once planned, but never realised SUPER-LEAR facility at CERN and was assumed to be “calculable or negligible” [72]. However, the magnetic field at SUPER-LEAR was planned to be 0.5 T, while it is foreseen to be 2 T in PANDA. It is therefore important to investigate if this effect is sufficiently large to be taken into consideration. This chapter presents of the expressions for how the polarisation vector is affected by magnetic fields. The results from a Monte Carlo simulation of this effect for the $\bar{p}p \rightarrow \bar{\Lambda}\Lambda$ reaction in the PANDA experiment are then given.

7.1 Precession of Polarisation Vectors in a Magnetic Field

The time evolution of a polarisation vector, $\bar{\Sigma}$, in a magnetic field is given by [135, 136]

$$\frac{d\bar{\Sigma}}{d\tau} = - \left[\frac{1}{\gamma+1} \left(\bar{u} \times \frac{d\bar{u}}{d\tau} \right) + \frac{ge}{2m} \bar{B}_{(0)} \right] \times \bar{\Sigma} \quad (7.1)$$

where $\bar{u} = \frac{\bar{p}}{m}$, g is the gyromagnetic ratio and $\bar{B}_{(0)}$ is the magnetic field in the particle rest frame

$$\bar{B}_{(0)} = \gamma \left(\bar{B} - \frac{\gamma}{\gamma+1} (\bar{\beta} \cdot \bar{B}) \bar{\beta} \right) . \quad (7.2)$$

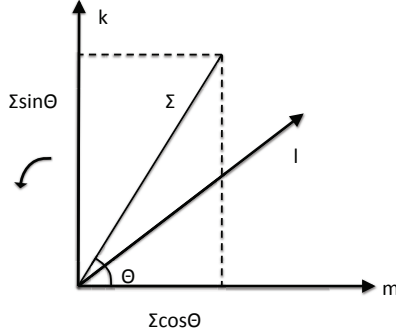


Figure 7.1: Reference system defined by the magnetic field in the hyperon rest frame and the polarisation vector at production. The part of the spin vector which is parallel to the magnetic field is constant, while the perpendicular part rotates as the hyperon travels through the magnetic field.

An uncharged hyperon is not accelerated by the magnetic field, which means that the first term in eq. (7.1) is zero and we get

$$\frac{d\bar{\Sigma}}{d\tau} = -\frac{ge}{2m}\bar{B}_{(0)} \times \bar{\Sigma} \quad (7.3)$$

This is a rotation of the perpendicular part of $\bar{\Sigma}$ around the, in this case constant, vector \bar{B}_0 with the angular velocity $\omega = \frac{ge}{2m}|\bar{B}_{(0)}|$. It is therefore convenient to define a reference system with the unit vectors

$$\begin{aligned} \hat{m} &= \hat{B}_0 \\ \hat{l} &= \hat{B}_0 \times \hat{\Sigma}(0) \\ \hat{k} &= (\hat{B}_0 \times \hat{\Sigma}(0)) \times \hat{B}_0 \end{aligned} \quad (7.4)$$

A graph of this coordinate system is shown in figure 7.1. The polarisation vector can be expressed in terms of these unit vectors as a function of the proper time τ

$$\begin{aligned} \bar{\Sigma}(\tau) &= |\bar{\Sigma}| \cos \Theta \cdot \hat{m} - |\bar{\Sigma}| \sin \Theta \sin \omega \tau \cdot \hat{l} + \\ &+ |\bar{\Sigma}| \sin \Theta \cos(\omega \tau) \cdot \hat{k} \end{aligned} \quad (7.5)$$

where Θ is the angle between $\vec{\Sigma}(0)$ and $\vec{B}_{(0)}$. This angle becomes $\frac{\pi}{2}$ which in the case of antihyperon-hyperon production in the PANDA detector, since the polarisation vector is perpendicular to the production plane and the magnetic field is parallel to the beam axis. As seen in eq.(7.5), the part of the polarisation vector which is parallel to the magnetic field, $|\vec{\Sigma}| \cos \Theta$, is constant, while the transverse part, $|\vec{\Sigma}| \sin \Theta$, rotates in the $\hat{k} \hat{l}$ plane.

Hyperon	Mass [MeV/c ²]	$c\tau$ [cm]	μ [μ_N]
Λ	1116	8.0	-0.613
Σ^+	1189	2.4	2.46
Σ^0	1193	$2.2 \cdot 10^{-9}$	1.61
Σ^-	1197	2.4	-1.16
Ξ^0	1315	8.7	-1.25
Ξ^-	1321	4.9	-0.651
Ω^-	1672	2.5	-2.02

Table 7.1: *Properties of the hyperons which are used in the calculation of their precession in the magnetic field [95].*

7.2 Effect on the measurement of Λ Polarisation

The Λ hyperon has a relatively long decay length. This means that its polarisation vector will be affected by the magnetic field in the PANDA detector. It is uncharged which makes the method described in the previous section applicable. Monte Carlo simulations of the $\bar{p}p \rightarrow \bar{\Lambda}\Lambda$ reaction were therefore made both for a low beam momentum, 1.64 GeV/c, and the highest possible beam momentum of PANDA, 15 GeV/c, to see how the effect depends on beam momentum. 500000 events were generated at each beam momenta.

The properties of the different hyperons which are needed in the calculation for their precession in the magnetic field are given in table 7.1. Once the angular velocity is calculated, only the lifetime of the Λ hyperon is needed to get the angle that the polarisation vector has rotated between the time of production and decay. Figure 7.2 shows the rotation angle for the two beam momenta. The mean value of the rotation angle is 2.9° for 1.64 GeV/c beam momentum and 5.38° for 15 GeV/c. As expected, the polarisation vector rotates more at the higher beam momentum of 15 GeV/c, since the value of $|\vec{B}_{(0)}|$ becomes higher.

Chapter 5 contains a description how to get the polarisation of the hyperons from the decay angles in their rest system. As a consequence of the parity invariance of the strong interaction, the hyperon is only polarised in the y di-

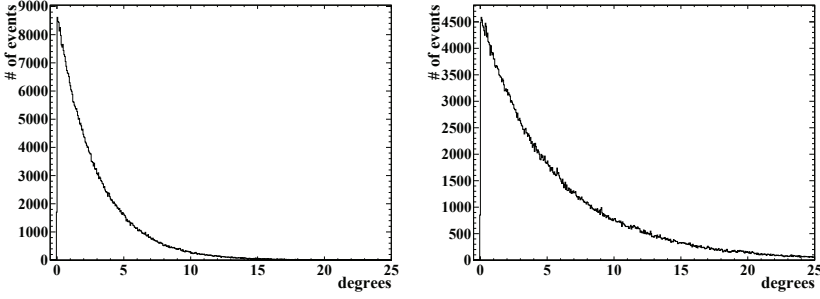


Figure 7.2: The angular difference between the polarisation vector of Λ at production and decay in PANDA, for a beam momentum of 1.64 GeV/c (left figure) and 15 GeV/c (right figure).

rection. Due to the precession in the magnetic field this is no longer the case at the time of the decay, if the angles of the Λ rest system at production are used. The polarisation vector is, however, not given for each generated event. It is reconstructed from the angular distribution in the hyperon decay using the full data sample. However, if the polarisation is reconstructed using hyperon decay angles from rest systems which have been rotated in the opposite direction as the polarisation vectors¹, the effect of the rotation on the polarisation measurement can be quantified.

The data was generated with an initial polarisation of 100% in the y direction, to see how much of this polarisation is rotated into the other directions. The generated Monte Carlo data were used to reconstruct the polarisation, using initial and rotated rest systems, respectively. Figure 7.3 shows the difference in the polarisation between the two different reconstruction procedures, for different values of the $\bar{\Lambda}$ production angle. The errors in polarisation are the statistical errors of the two reconstructed values added in quadrature, the errors in $\cos\Theta_{\bar{\Lambda}}$ are the bin widths. The upper figure shows the result for the data with a beam momentum of 1.64 GeV/c. The expected effect, that polarisation in the y direction is transferred to the other directions, is clearly seen. The amount of decrease in the y direction is not substantial, while the increase in the x and z direction is significant. By simple geometrical considerations the average decrease in the y direction should be $1 - \cos 2.9^\circ \approx 0.001$ and the increase in the other directions $\sin 2.9^\circ \approx 0.05$, which is consistent with the result in figure 7.3. The lower figure shows the result for the data at 15 GeV/c beam momentum. In this case the geometrical considerations give $1 - \cos 5.4^\circ \approx 0.004$ and $\sin 5.4^\circ \approx 0.09$ respectively, which is also roughly consistent with figure 7.3 for the x and z directions. A noticeable difference

¹The method to compensate for the effect when experimental data is used to reconstruct the polarisation is to rotate the rest systems in the same way as the polarisation vector.

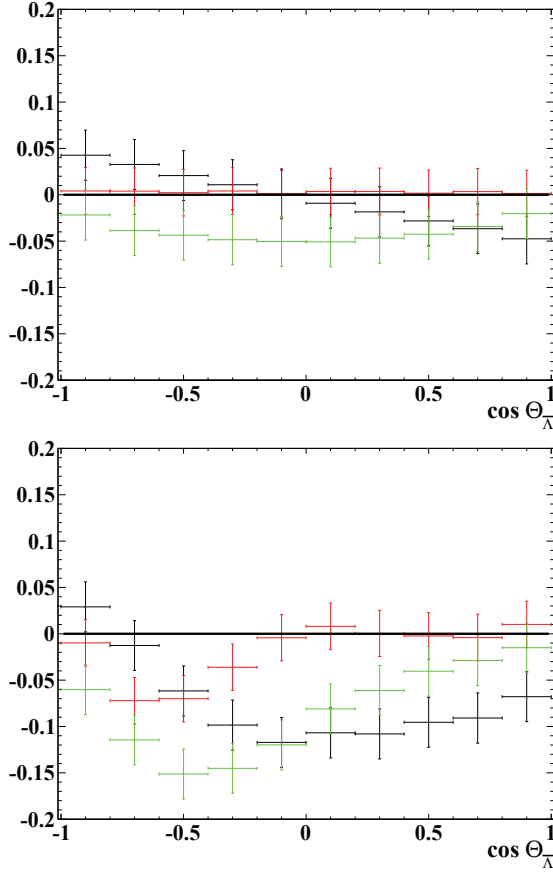


Figure 7.3: The difference in reconstructed polarisation using a Λ rest system which has been rotated in the opposite way as the polarisation vector as compared to using the rest system at production, in the x (black), y (red) and z (green) directions. In the upper figure the beam momentum is 1.64 GeV/c and in the lower 15 GeV/c.

from the lower beam momentum is that the polarisation in the y direction is affected for negative values of $\cos \Theta_{\bar{\Lambda}}$.

7.3 Effect on the measurement of $\bar{\Lambda}\Lambda$ Spin Correlations

Intuitively, it seems that the rotation of the polarisation vectors should also affect the measured values of spin correlations between the $\bar{\Lambda}$ and Λ hyperon. At production the polarisation vectors of the $\bar{\Lambda}$ and Λ hyperon are in the y direction of their respective rest system, which means that they are parallel. The two polarisation vectors are then rotated in opposite directions, which means that they are no longer parallel at their decay. Figure 7.4 shows the

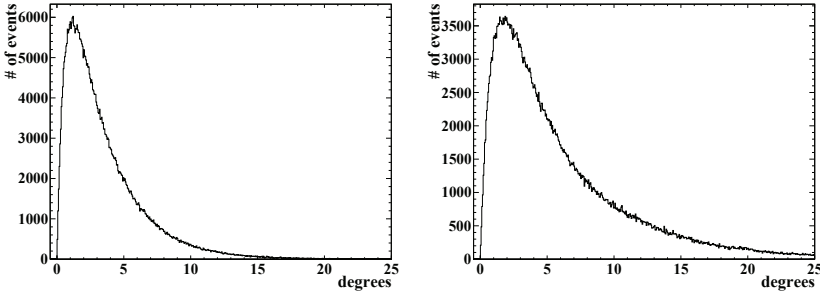


Figure 7.4: The angle between the polarisation vectors of Λ and $\bar{\Lambda}$ at the decay which are parallel at production, at a beam momentum of 1.64 GeV/c (left figure) and 15 GeV/c (right figure).

angle between the Λ polarisation vector and the $\bar{\Lambda}$ at the decay for the two beam momenta. The mean value of the angle is 3.5° for 1.64 GeV/c beam momentum and 5.8° for 15 GeV/c beam momentum.

As for the polarisation, the effect of the rotation can be investigated by comparing spin correlations calculated using rotated and initial rest systems respectively. As described in section 3.1.5, the spin correlations, which according to parity conservation, can be non-zero are C_{xx} , C_{yy} , C_{zz} and $C_{xz} = C_{zx}$. The data was generated with $C_{yy} = 1$ and the others equal to zero. The results are shown in figure 7.5 for 1.64 GeV/c beam momentum and in figure 7.6 for 15 GeV/c beam momentum. The errors in spin correlations are the statistical of the two reconstructed values added in quadrature. The spin correlations appear to be completely unaffected by the rotation of the rest system at 1.64 GeV/c and marginally affected at 15 GeV/c. One way to understand this is that rotating the two rest systems in opposite directions do not always make the hyperon spins defined in them less correlated. Depending on the original relation between the two spin directions they might as well become more correlated.

A more strict explanation can be given by calculating the expectation value $\langle \cos \Theta_{\bar{p},i} \cos \Theta_{p,j} \rangle$ used for the reconstruction of the spin variable C_{ij} . Let the two angles change by ϕ_1 and ϕ_2 , respectively, due to the rotation of the rest systems. The new expectation value then becomes

$$\begin{aligned}
 & \langle \cos (\Theta_{\bar{p},i} + \phi_1) \cos (\Theta_{p,j} + \phi_2) \rangle = \\
 & = \frac{1}{4} \int_{-1}^1 \int_{-1}^1 \cos (\Theta_{\bar{p},i} + \phi_1) \cos (\Theta_{p,j} + \phi_2) \\
 & \times (1 + \alpha \bar{\alpha} C_{1,j} \cos \Theta_{\bar{p},i} \cos \Theta_{p,j}) d\cos \Theta_{\bar{p},i} d\cos \Theta_{p,j}
 \end{aligned} \tag{7.6}$$

If only linear terms in the rotation angles are kept, this expression becomes

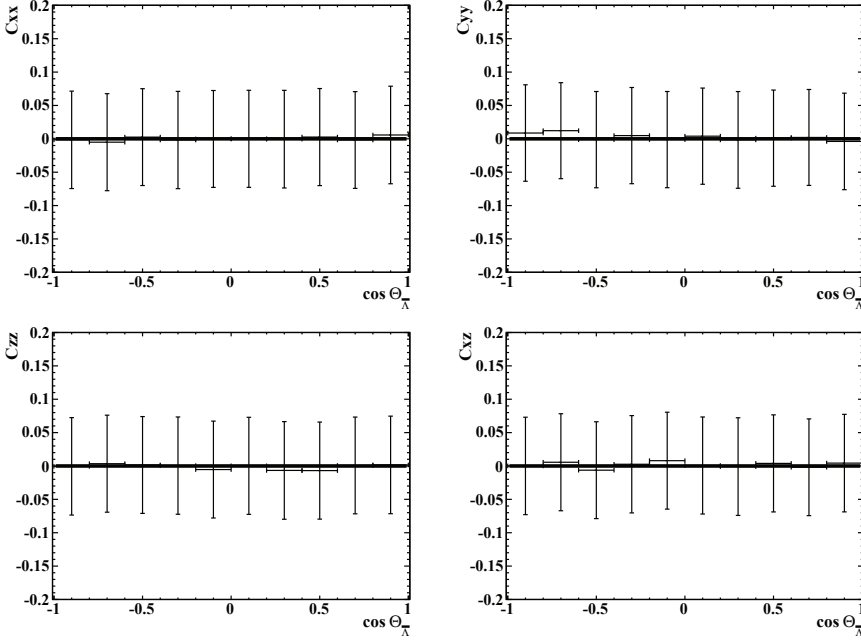


Figure 7.5: The difference in reconstructed spin correlations (C_{xx} , C_{yy} , C_{zz} and C_{xz}) using Λ rest systems which has been rotated in the opposite way as the polarisation vector as compared to using the rest systems at production. The beam momentum is 1.64 GeV/c.

$$\begin{aligned}
 & \frac{1}{4} \int_{-1}^1 \int_{-1}^1 (\cos \Theta_{\bar{p},i} \cos \Theta_{p,j} - \phi_1 \sin \Theta_{\bar{p},i} \cos \Theta_{p,j} - \phi_2 \cos \Theta_{\bar{p},i} \sin \Theta_{p,j}) \\
 & \times (1 + \alpha \bar{\alpha} C_{1,j} \cos \Theta_{\bar{p},i} \cos \Theta_{p,j}) d \cos \Theta_{\bar{p},i} d \cos \Theta_{p,j} = \\
 & = \frac{1}{4} \int_{-1}^1 \int_{-1}^1 \cos \Theta_{\bar{p},i} \cos \Theta_{p,j} (1 + \alpha \bar{\alpha} C_{1,j} \cos \Theta_{\bar{p},i} \cos \Theta_{p,j}) d \cos \Theta_{\bar{p},i} d \cos \Theta_{p,j} = \\
 & = \langle \cos \Theta_{\bar{p},i} \cos \Theta_{p,j} \rangle
 \end{aligned} \tag{7.7}$$

where the fact that only terms with even power of both cosines are non-zero since the integration interval is between -1 and 1 has been used. The result is that to the precision of first order terms in the rotation angles, the spin correlations are unaffected.

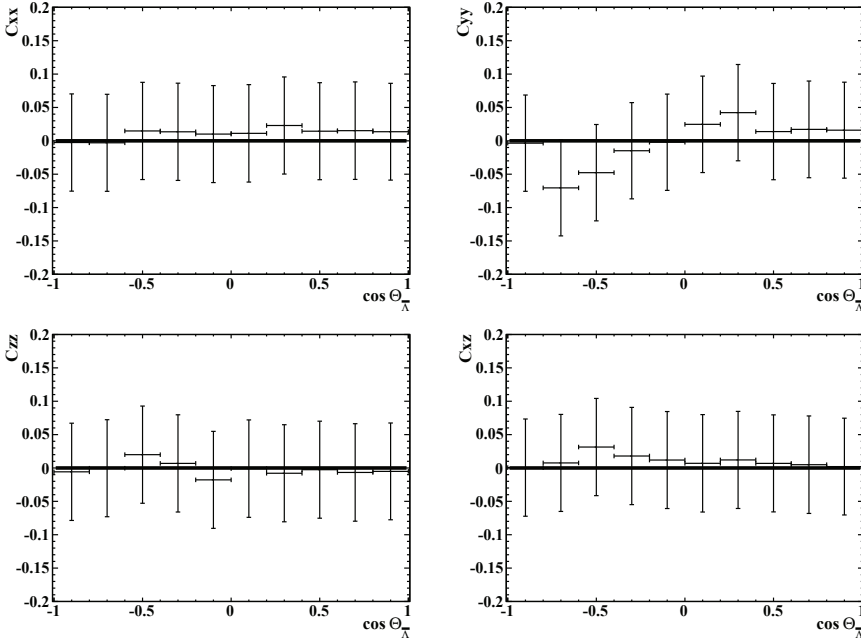


Figure 7.6: The difference in reconstructed spin correlations (C_{xx} , C_{yy} , C_{zz} and C_{xz}) using a Λ the rest systems at production as compared to systems which has been rotated in the opposite way as the polarisation vector. The beam momentum is 15 GeV/c.

7.4 Other Hyperons

The investigation in this chapter has been focused on Λ hyperons, since the fact that it is uncharged considerably simplifies the calculations. Of the other uncharged hyperons, the Σ^0 hyperon decays electromagnetically and consequently the decay length is far too short for the polarisation vector to have time to be affected by the magnetic field. The Ξ^0 hyperon, on the other hand, has a long decay length and a large magnetic moment, see table 7.1. However, due to the π^0 in the final state Ξ^0 will be difficult to reconstruct in the PANDA data.

The equations become much more complicated for charged hyperons, since they are accelerated by the magnetic field. Looking at their properties relevant for the equations in table 7.1 one may think about the qualitative difference from the case of Λ hyperons. The charged Σ , Ξ and Ω hyperons all have shorter decay lengths, higher masses and magnetic moments which are equal or higher compared to the Λ hyperon. The rotation angles of their polarisation vectors are therefore expected to be smaller than for the Λ hyperon, perhaps with the exception of the Σ^+ hyperon, which has a large magnetic moment

of $\mu = 2.458\mu_N$. All charmed hyperons have too short decay lengths for the polarisation vector to be affected by the magnetic field.

8. Conclusions and Outlook

The conclusions focus on the work I have done and are divided into three parts. The first part concerns the derivation of the decay angular distributions for the spin $3/2$ Ω hyperon and its daughter Λ hyperon, to see which Ω polarisation parameters can be reconstructed from an unpolarised initial state. The second part deals with the simulations of multi-strange and charmed $\bar{p}p \rightarrow \bar{Y}Y$ reactions with emphasis on the extraction of spin variables, as well as simulations for CP violation in hyperon decays. The last part concerns the investigation of the effect of the magnetic field on the measurement of hyperon spin variables in the PANDA detector. An outlook for future studies is also given.

8.1 Calculations of Decay Angular Distributions for the Spin $3/2$ Ω Hyperon

The density matrix formalism was used to calculate the decay angular distributions of hyperons. Both spin $1/2$ and $3/2$ hyperons were considered. The new results for this thesis are for the spin $3/2$ Ω hyperon. An explicit expression for the density matrix of a spin $3/2$ particle, containing polarisation parameters, was derived. A spin $3/2$ particle has 15 polarisation parameters, instead of three for spin $1/2$ particles. Eight of these parameters are zero, since the Ω hyperons are created with the parity conserving strong interaction in the $\bar{p}p \rightarrow \bar{\Omega}\Omega$ reaction. The angular distribution for the $\Omega^- \rightarrow \Lambda K^-$ decay was calculated, using the density matrix for spin $3/2$ particles. This calculation is simplified by the fact that the asymmetry parameter α is close to zero for this decay and the result is given in eq.(3.36). This angular distribution is only given without explicit expressions for the density matrix elements previously in the literature. Three of the seven non-zero polarisation parameters show up in the angular distribution. The daughter Λ hyperon also decays weakly and the angular distribution of this $\Lambda \rightarrow p\pi^-$ decay was also calculated. The result is given in eq.(3.44). This angular distribution, with all polarisation parameters considered, is not previously reported. A linear combination of two of the other non-zero polarisation parameters contributes to the angular distribution of this subsequent decay. The Ω asymmetry parameters β and γ , which have not been measured, are also involved.

There are constraints from quantum mechanics that the density matrix has to fulfill. Having the explicit form of the spin $3/2$ density matrix, these con-

straints can be used to put constraints on the possible values of Ω hyperon polarisation parameter. Four inequalities that the parameters have to fulfill were deduced. These are given in eq.(3.60).

In chapter 5, expressions were deduced for the reconstruction of the Ω hyperon polarisation and asymmetry parameters from the experimental data. By calculating expectation values, it was shown how these parameters can be reconstructed by taking averages of the decay angles. For the linear combination of polarisation parameter in the $\Lambda \rightarrow p\pi^-$ decay distribution, the value can be reconstructed up to a sign. The expressions are given in eq.(5.8), eq.(5.12) and eq.(5.13). Expressions for the errors of the parameters are given in eq.(5.10) and eq.(5.15).

8.2 Simulations of Multi-Strange and Charmed $\bar{p}p \rightarrow \bar{Y}Y$ Reactions

Simulations were performed for the reactions $\bar{p}p \rightarrow \bar{\Xi}^+\Xi^-$, $\bar{p}p \rightarrow \bar{\Omega}^+\Omega^-$ and $\bar{p}p \rightarrow \bar{\Lambda}_c^-\Lambda_c^+$. The reconstruction efficiency and the expected number of reconstructed events for the three reactions are given in the table below. The beam momenta and the cross sections used for the calculation of expected number of events are given in the same table. As seen, high statistics will be collected in a short time for the $\bar{p}p \rightarrow \bar{\Xi}^+\Xi^-$ reaction, where the existing data consists of only a handful of events. For the $\bar{p}p \rightarrow \bar{\Omega}^+\Omega^-$ and the $\bar{p}p \rightarrow \bar{\Lambda}_c^-\Lambda_c^+$ reactions, the PANDA data will be the first.

	$\bar{p}p \rightarrow \bar{\Xi}^+\Xi^-$	$\bar{p}p \rightarrow \bar{\Omega}^+\Omega^-$	$\bar{p}p \rightarrow \bar{\Lambda}_c^-\Lambda_c^+$
beam momentum [GeV/c]	4	12	12
reconstruction efficiency [%]	17	30	35
σ	$\sim 2 \mu\text{b}$	$\sim 2 \text{ nb}$	$\sim 0.1 \mu\text{b}$
expected # of events	$\sim 30/\text{s}$	$\sim 80/\text{hour}$	$\sim 25/\text{day}$

Table 8.1: *Reconstruction efficiency and expected number of reconstructed events obtained from the simulations for the $\bar{p}p \rightarrow \bar{\Xi}^+\Xi^-$, $\bar{p}p \rightarrow \bar{\Omega}^+\Omega^-$ and $\bar{p}p \rightarrow \bar{\Lambda}_c^-\Lambda_c^+$ reactions. The beam momenta and the cross sections used for the calculation are also given.*

The reconstruction efficiency for all three reactions were found to be non-zero for all values of the hyperon CM production angles. This means that spin variables can be reconstructed over the full angular interval. Two different methods to compensate for asymmetry in detector efficiency were tested in the reconstruction of spin variables for the $\bar{p}p \rightarrow \bar{\Xi}^+\Xi^-$ reaction. Both methods, one using acceptance functions generated from Monte Carlo and the other based on a symmetry of the detector efficiency, worked well. In this way both

polarisation and spin correlations were well reconstructed for this reaction. For the $\bar{p}p \rightarrow \bar{\Omega}^+\Omega^-$ and the $\bar{p}p \rightarrow \bar{\Lambda}_c^-\Lambda_c^+$ reactions polarisation parameters, polarisation and spin correlations were well reconstructed using the method with acceptance functions.

Simulations were also performed to investigate the possibility of measuring CP violation parameters for hyperon decays. Both the $\bar{p}p \rightarrow \bar{\Lambda}\Lambda$ and the $\bar{p}p \rightarrow \bar{\Xi}^+\Xi^-$ reactions were considered. It was found that it is important to not use PID in these measurements, since it will introduce asymmetry between particles and antiparticles. For the A parameter, which quantifies the difference in the value of the asymmetry parameter α between the hyperon and antihyperon, it was shown that the measurement is feasible only if events with hyperon decays close to the beam axis are considered. In the $\bar{p}p \rightarrow \bar{\Xi}^+\Xi^-$ reaction, also the B parameter, which quantifies the difference in the value of the asymmetry parameter β between the hyperon and antihyperon, can be measured. This parameter is measured in the decay of the daughter Λ hyperon. For this measurement the required symmetry of the detector is along a direction of the Λ rest system which is not perpendicular to the beam axis. Since no such symmetry exists, acceptance functions have to be used for this measurement.

8.3 Effect of Magnetic Field on Measurement of Hyperon Spin Variables

Monte Carlo simulations were made for the $\bar{p}p \rightarrow \bar{\Lambda}\Lambda$ reaction to investigate the effect of the magnetic field in the PANDA detector on the measurement of spin variables. The simulations were made at two different beam momenta, 1.64 GeV/c and 15 GeV/c, to study the beam momentum dependence.

The average value of the angle that the polarisation vector rotates between production and decay of the Λ hyperon was found to be 2.9° at 1.64 GeV/c and 5.4° at 15 GeV/c. Neglecting this in the measurement of the Λ polarisation will affect the measured values slightly. No effect was found at 1.64 GeV/c in the direction which perpendicular to the production plane of the Λ hyperon. In the directions which are in the production plane, however, the effect was found to be a fake polarisation of about 5%. At 15 GeV/c, a small decrease in the direction perpendicular to the production plane of up to 5%, was found for negative values of $\cos\Theta_{\bar{\Lambda}}$. The fake polarisation in the directions in the production plane was found to be about 10-20% in this case.

The polarisation vectors of the $\bar{\Lambda}$ and Λ hyperons are parallel at production. Due to their precession in the magnetic field this will no longer be the case at the decay of the hyperons. In the simulations the average value of the angle between the two polarisation vectors at decay was found to be 3.5° at 1.64 GeV/c and 5.8° at 15 GeV/c. It was found that this does not affect measurements of spin correlations, since the effect averages to zero over all events.

8.4 Outlook

The development of the new framework for PANDA, called PANDArOOT, was not at the stage where antihyperon hyperon physics could be studied at the time of this thesis. Since the framework used in this thesis has an idealised version of reconstruction and pattern recognition, the results should in this sense be viewed as a best case scenario. In the future, these $\bar{p}p \rightarrow \bar{\Sigma}\Sigma$ reactions should also be studied in PANDArOOT, which will have a full reconstruction and pattern recognition chain, for comparison.

Other questions for future studies are to find a suitable trigger for $\bar{p}p \rightarrow \bar{\Sigma}\Sigma$ reactions and more extensive background studies for the multi-strange and charmed reactions..

Concerning the calculations of the Ω hyperon decay, it would be interesting to investigate whether more polarisation parameters can be extracted from the decays if angular distributions depending on angles from both decays are studied. This will give a slightly more complex analysis and worse statistics since fewer angles are integrated out. Still, it might be worth it if more information can be extracted.

9. Svensk sammanfattning

Titeln på avhandlingen är Multi-strange and Charmed Antihyperon-Hyperon Physics for PANDA. Arbetet tillhör ett område av fysiken som omnämns hadronfysik.

Vad är en hadron?

Dagens teori om hur materien är uppbyggd kallas standardmodellen. Enligt standardmodellen, som är väldigt väl testad experimentellt, finns det tolv elementära partiklar som bygger upp materien. Dessa växelverkar via tre krafter: elektromagnetism, den svaga kraften och den starka kraften. Den fjärde kraften som finns i naturen, gravitationen, är inte inkluderad i standardmodellen, men den är försumbar för beräkningar påelementarpartikelnivå. De tolv partiklarna är indelade i två grupper: kvarkar och leptoner. Skillnaden mellan dem är att kvarkar växelverkar via den starka kraften, medan leptoner inte gör det. För varje partikel finns även en antipartikel med samma massa men motsatt laddning.

De tre krafterna beskrivs i standardmodellen som utbyte av en sorts partiklar kallade gaugebosoner. För elektromagnetism är denna utbytespartikel fotonen. Motsvarande partiklar för den starka kraften kallas gluoner, vilka finns av åtta olika sorter. En stor skillnad mellan gluonerna och fotonerna är att gluonerna själva växelverkar via den starka kraften, medan fotonerna är opåverkade av elektromagnetismen. Denna växelverkan mellan gluonerna leder till ett mycket speciellt beteende hos den starka kraften. Vid tillräckligt långa avstånd avtar inte kraften med avståndet. Om två starkt växelverkande partiklar förs allt längre ifrån varandra växer den potentiella energin mellan dem mot oändligheten. Vid ett visst avstånd blir det därför energetiskt fördelaktigt att bilda nya partiklar och antipartiklar för att skärma kraften. Resultatet blir att det inte går att isolera en partikel som har laddning med avseende på den starka kraften. Den starka kraften har tre sorters laddning, kallade röd, blå och grön. De har inget med de vanliga vardagliga färgerna att göra. Deras namn beror på att kombinationen av de tre laddningarna ger en neutralt färgladdad partikel, precis som färgerna blandas till vitt. Eftersom ingen partikel med färgladdning kan isoleras, dyker de starkt växelverkande elementarpartiklarna upp i naturen i form av kombinationer som tillsammans ger en neutral laddning. Det är de partiklar som utgörs av en sådan neutral kombination av elementarpartiklar

som kallas hadroner. Eftersom kvarkar har laddning utav en färg och antikvarkar laddning av en antifärg, finns det två enkla sätt att skapa en färgneutral partikel: tre kvarkar av var sin färg, i vilket fall partikeln kallas för baryon och en kvark tillsammans med en antikvark, i vilket fall partikeln kallas för meson. Även antibaryoner med tre antikvarkar av var sin antifärg ger en neutral kombination. Alla kända hadroner är utav något av dessa slag.

Standardmodellens teori för att ge massa åt elementarpartiklarna kallas Higgs-mekanismen. Den går ut på att ett Higgs-fält introduceras, vars växelverkan med elementarpartiklarna ger dem massa. Higgsfältet ger också upphov till en Higgs-partikel, vilken nyligen med största sannolikhet har observerats experimentellt på LHC. Elementarpartiklarnas massa utgör dock bara en mycket liten del av hadronernas, och därmed världens, massa. Över 98% av hadronernas massa genereras istället av den starka kraften när den binder kvarkarna till en sammansatt partikel. En förståelse av hur det går till när den starka kraften binder kvarkarna till hadroner är därför viktig. Det är denna fråga hadronfysik handlar om. Det är ett teoretiskt sett svårt område, eftersom energiskalan där kvarkar binds till hadroner ligger mellan två olika sätt att göra beräkningar på partikelreaktioner. För höga energier används en störningsmetod, där den starka kraften beskrivs som utbyte av gluoner. För lägre energier finns effektiva teorier, där den starka kraften istället beskrivs som utbyte av mesoner. Däremellan är det oklart vilken teoretisk beskrivning som bör användas. Mer experimentell data för reaktioner vid denna energiskala kommer därför bli av stor betydelse för att klargöra situationen.

Vad är en hyperon?

Det finns sex olika sorters kvarkar kallade up (u), down (d), charm (c), strange (s), top (t), bottom (b). De två första lättaste kvarkarna är de stabila kvarkarna, vilka de tyngre kvarkarna sönderfaller till. Tillsammans bygger de upp protonen (uud) och neutronen (udd). Protonen och neutronen bygger i sin tur upp atomkärnan och alltså i stort sett all världens synbara materia.

Det finns dock icke-stabila baryoner där en eller flera u- och d-kvarkar är utbytta mot tyngre kvarkar. Det är dessa baryoner som kallas för hyperoner. För de vanligaste hyperonerna är de tyngre kvarkarna s-kvarkar, vilket är den tredje lättaste kvarksorten, men de kan också vara c-kvarkar, i vilket fall partikeln kallas för charmerad hyperon.

När hyperonerna sönderfaller till lättare baryoner omvandlas de tyngre kvarkarna till lättare sorter. Detta kan bara ske via den svaga kraften. Den svaga kraften har en speciell egenskap. Den är inte symmetrisk under en paritetstransformation¹. Detta innebär att vinkelfördelningen hos hyperonens

¹Om fysikreaktionen beskrivs i ett koordinatsystem, innebär paritetstransformationen en 180° rotation följt av en spegling av koordinatsystemets axlar.

dotterpartiklar i sönderfallet inte behöver vara isotrop i rummet. Istället fördelar de sig på ett speciellt sätt i förhållande till riktningen av hyperonens spinn. Spinn är ett inre rörelsemängdsmoment, som partiklar har utöver banrörelsemängdsmoment. Det är en kvantmekanisk egenskap som inte har någon motsvarighet inom klassisk fysik. Det är ofta svårt att få information om partiklars spinn i experiment. För hyperoner kan dock olika spinnvariabler extraheras genom att mäta vinkelfördelningarna i deras sönderfall.

En annan aspekt av hyperoner som är intressant att studera är om det finns brott mot CP-symmetrin i deras sönderfall. CP-transformationen innebär paritetstransformation kombinerat med att partiklarnas laddning byter tecken. Praktiskt taget alla fysikens lagar är symmetriska under denna transformation. Dock har små brott mot CP-symmetrin observerats i system av mesoner. Eftersom den kombinerade CPT symmetrin, där T står för tidsinversion, tros gälla för all fysik, innebär ett brott mot CP-symmetrin även ett brott mot tidssymmetrin, d.v.s. att fysikens lagar inte är de samma om tiden ändrar riktning. För baryoner har CP-brott aldrig observerats och ett observerat CP-brott hos hyperoner skulle därför vara en stor upptäckt. CP-brott krävs för att förklara överskottet av materia jämfört med antimateria i universum. De observerade brotten hos meson-system är alldeles för småför att kunna ge upphov till detta överskott, och mycket möda läggs därför på att hitta CP-brott hos andra partiklar. Vidare är de teoretiska förutsägelserna från standardmodellen små för värdena på de parametrar som testar CP-brott hos hyperoner. Om större värden uppmäts är det en indikation om fysik bortom standardmodellen.

Vad är PANDA?

PANDA är en kollaboration som planerar att bygga en detektor för att utföra hadronfysikexperiment vid forskningscentret FAIR, vilket håller på att byggas utanför Darmstadt i Tyskland. Över 500 forskare från 17 olika länder arbetar inom kollaborationen. PANDA står för anti-Proton ANnihilation at DArmstadt. Vad som används i experimentet är alltså en accelererad stråle av antiprotoner, vilka sedan kan annihileras mot protoner i vila. PANDA har ett mycket brett forskningsprogram inom hadronfysik. Ett av områdena som kan studeras är antihyperon-hyperonfysik. Antiprotonerna accelereras till hög rörelseenergi, vilken i kollisionen kan omvandlas till massa så att partiklar som är tyngre än det ursprungliga antiproton-protonparet kan bildas. Om rörelseenergin är tillräckligt hög kan antihyperon-hyperonpar bildas. Dessa reaktioner sker vid den problematiska energiskalan beskriven ovan, där det är oklart vilket teoretiskt angreppssätt som är lämpligt. Det är därför intressant att testa teoretiska modeller baserade på de två angreppssätten mot experimentell data. Något som dessa modeller måste beskriva är de olika spinnvariablerna som kan mätas genom sönderfallsfördelningar. Om både antiproton-

erna och protonerna innan kollisionen är opolariserade, är spinnvariablerna som kan mätas polarisation² hos de enskilda hyperonerna samt korrelationer mellan spinnen hos antihyperonen och hyperonen i vissa riktningar.

Vad har jag gjort?

Jag har studerat reaktioner där ett antihyperon-hyperonpar bildas i antiproton-proton kollisioner. Mitt fokus har legat på reaktioner av den typen där hyperonerna innehåller mer än en s-kvark (därav multi-strange i titeln) eller en c-kvark (därav charmed i titeln). Nästan all nu existerande data är för reaktioner där hyperonerna innehåller en enda s-kvark, och avseendet med mitt arbete är därför att undersöka vad det kommande PANDA-experimentet kan ge för data i det här outforskade området av antihyperon-hyperonfysik.

Avhandlingens innehåll består av tre delar. Den första delen innehåller beräkningar, för att relatera spinnvariabler till vinkelfördelningar i hyperonsönderfallen. De flesta hyperoner har spinn 1/2. Sönderfallsfördelningarna för dessa ges av standardberäkningar. Ω^- -hyperonen har dock spinn 3/2 vilket gör beräkningar ganska komplicerade. Genom att använda en formalism med densitetsmatriser har jag genomfört dessa beräkningar. Även uttryck för hur spinnvariabler beräknas från uppmätta vinklar har härletts. Andra delen består av simuleringar för att undersöka hur väl mätningar för dessa reaktioner som kan utföras med PANDA-detektorn. PANDA-detektorn består av många subdetektorer för detektion av olika partiklar. Vad som har hänt i en fysikreaktion måste rekonstrueras utifrån deras respons. Hur väl det går att göra måste undersökas genom simuleringar. För dessa simuleringar finns ett ramverk där hela detektorn har modellerats. Simuleringarna går ut på att fysikhändelser (exempelvis att antihyperon-hyperonpar bildas) först genereras, vilket ger partiklar som går åt olika håll genom detektorn. Sedan modelleras vilken respons de olika subdetektorerna hade gett på dessa partiklar. Utifrån denna respons ska sedan de ursprungliga fysikhändelserna rekonstrueras. Jag har gjort simuleringar för de tre fysikreaktionerna $\bar{p}p \rightarrow \bar{\Xi}^+\Xi^-$, $\bar{p}p \rightarrow \bar{\Omega}^+\Omega^-$ och $\bar{p}p \rightarrow \bar{\Lambda}_c^-\Lambda_c^+$. De inblandade hyperonerna har kvarkinnehållen dss (Ξ^-), sss (Ω^-) respektive udc (Λ_c^+). Simuleringarna visar att statistiken kommer att bli mycket bättre för $\bar{p}p \rightarrow \bar{\Xi}^+\Xi^-$ reaktionen, än i tidigare mätningar vilka bara hade en handfull händelser. Även för $\bar{p}p \rightarrow \bar{\Omega}^+\Omega^-$ och $\bar{p}p \rightarrow \bar{\Lambda}_c^-\Lambda_c^+$, vilka aldrig tidigare mätts, kommer statistiken att bli ganska bra. För alla fallen kan spinnvariabler rekonstrueras väl från vinkelfördelningarna i hyperonernas sönderfall. Jag har även gjort simuleringar som berör sökandet efter CP-brott i hyperonsönderfall. De visar att man i sådana mätningar bör begränsa sig till händelser där hyperonerna sönderfaller nära stråxelns. Detta för att minimera systematiska fel från

²Om partiklar är polariserade är inte spinnets riktning slumpmässig, utan pekar företrädesvis i en speciell riktning.

asymmetrier i detektorrespons. Den tredje delen behandlar ett möjligt problem som kan uppstå vid studerandet av antihyperon-hyperonfysik med PANDA-detektorn. Ett starkt magnetfält på 2T kommer att ligga över detektorn, för att möjliggöra rörelsemängdsmätningar. Detta magnetfält påverkar dock spinnet på hyperonerna. Jag har genom simuleringar undersökt vad detta innebär för studierna av spinnvariabler. Effekten visar sig vara ganska liten och kan kompenseras för.

10. Acknowledgements

Firstly, I would like to thank my supervisor Tord Johansson. You have always taken your time to discuss questions which have come up during my work. A lot of interesting physics has been discussed, in addition to the regular updates on the current state of MFF and Brynäs. I also appreciated our many travels together, with the occasional late night drinking red wine. Your many suggestions for the thesis were of great value. Thanks also to my other supervisor Andrzej Kupsc for having trust in me and checking the thesis.

Secondly, I would like to thank my three office mates during my PhD studies. When I first arrived at the department, Sophie Grape, who I then shared the office with, made me feel acquainted with the place in a short time. We had much fun during the two and a half years we shared the office. You always kept me alert with your many question on everything from physics to clowns. Our discussions about almost anything often became very interesting. Thanks for being my companion in the exploration of PANDA simulations and hyperons. Thanks also for the proof-reading of the thesis. I then shared the office with Lena Heijkenskjöld for a short but very nice period. Thanks for a lot of interesting discussions and for giving me good literary tips, without knowing it yourself. Then followed my current office mate Li Caldeira-Balkeståhl, who I would also like to thank for keeping up the good atmosphere of the office, even though I feel I have been a bit distant during this period, being on parental leave and writing the thesis.

My gratitude also goes to Stefan Leupold for all the time you have spent answering my theory questions and discussing hyperon decays, Göran Fäldt for help concerning spin vectors in magnetic fields, Magnus Wolke for discussions on CP violation and comments on the thesis, Kjell Fransson for help on my work concerning PWO crystals which did not end up in the thesis and Karin Schönning for a lot of valuable input when writing the thesis.

For help concerning the simulation framework, I am grateful to the Bochum group: Matthias Steinke, Bertram Kopf, Marc Päzelius and Jan Zhong. I would also like to thank the PANDA people in Stockholm, Per-Erik and Klas Marcks von Würtemberg, for very nice company during MAX-lab weeks and PANDA meetings.

Thanks to Inger Ericsson and Annica Elm for help on various problems and to Teresa Kupsc for fixing my computer.

During my years at department I have gotten to know many interesting people. I enjoyed going to art exhibitions and baking cakes with P-A. Thanks to Henrik J. and Oscar for taking me to football games. Thanks to Patrik for being a good friend and helping me in the thesis process, when you were always three weeks ahead of me. Among the other nice people I have gotten to know are Carla, Henrik P., Camille, Olle, Carl-Oscar, Agnes, David, Anna, Elias, Aila, Glenn, Dominik, Christoph, Jan, Jörn, Marek, Pawel, Maja, Kristofer, Mikael, Peder.

Thanks to my old physics friends (and Calle) in the book club for keeping up our very interesting meetings some times a year.

To my family in Lund and Malmö: Bibbi, Göran, Elin, Ronny, Kajsa, Lisa, Hanna, Sanna, Katrin and Clara. I feel very close to you even though I am far away geographically. I think that we get strength from each other during the hardest of times that we are going through. I hope to move closer to you in the future.

To my wife Lovisa, who I love very much: Sharing life with you makes everything better. I am very happy to have spent these five years in Uppsala (as well as the previous ten years) with you.

And, above all, to Alva: it has been wonderful spending so much time with you during the last two and a half years. Thank you for waking me up early in the morning and always making me happy whenever I think of you.

11. Bibliography

- [1] S. L. Glashow, Nucl. Phys. **22** (1961) 579.
- [2] S. Weinberg, Phys. Rev. Lett. **19** (1967) 1264.
- [3] A. Salam, 8th Nobel Symposium, 19-25 May 1968, Lerum, Sweden, Conf. Proc. C **680519** (1968) 367.
- [4] E. D. Bloom *et al.*, Phys. Rev. Lett. **23** (1969) 930.
- [5] M. Breidenbach *et al.*, Phys. Rev. Lett. **23** (1969) 935.
- [6] J. I. Friedman and H. W. Kendall, Ann. Rev. Nucl. Part. Sci. **22** (1972) 203.
- [7] M. Gell-Mann, Phys. Lett. **8** (1964) 214.
- [8] G. Zweig, in 'Developments In The Quark Theory Of Hadrons', Vol. 1 ed. by D. B. Lichtenberg and S. P. Rosen, Hadronic Pres Nonantum, MA (1980) ISBN 0-911767-02-9, p. 22-101 and preprint CERN-TH-401
- [9] N. Cabibbo, Phys. Rev. Lett. **10** (1963) 531.
- [10] M. Kobayashi and T. Maskawa, Prog. Theor. Phys. **49** (1973) 652.
- [11] F. Abe *et al.* [CDF Collaboration], Phys. Rev. Lett. **74** (1995) 2626 [hep-ex/9503002].
- [12] F. Englert and R. Brout, Phys. Rev. Lett. **13** (1964) 321.
- [13] P. W. Higgs, Phys. Lett. **12** (1964) 132.
- [14] P. W. Higgs, Phys. Rev. Lett. **13** (1964) 508.
- [15] J. Beringer *et al.* [Particle Data Group Collaboration], Phys. Rev. D **86** (2012) 010001.
- [16] T. D. Lee and C. -N. Yang, Phys. Rev. **104** (1956) 254.
- [17] C. S. Wu *et al.*, Phys. Rev. **105** (1957) 1413.
- [18] J. H. Christenson, J. W. Cronin, V. L. Fitch and R. Turlay, Phys. Rev. Lett. **13** (1964) 138.
- [19] A. Alavi-Harati *et al.* [KTeV Collaboration], Phys. Rev. Lett. **83** (1999) 22 [hep-ex/9905060].

- [20] V. Fanti *et al.* [NA48 Collaboration], Phys. Lett. B **465** (1999) 335 [hep-ex/9909022].
- [21] B. Aubert *et al.* [BABAR Collaboration], Phys. Rev. Lett. **87** (2001) 091801 [hep-ex/0107013].
- [22] Y. Chao *et al.* [Belle Collaboration], Phys. Rev. Lett. **93** (2004) 191802 [hep-ex/0408100].
- [23] A. Angelopoulos *et al.* [CPLEAR Collaboration], Phys. Lett. B **444** (1998) 43.
- [24] A.d. Sakharov, Pis'ma Zh. Eksp. Teor. Fiz **5**, (1967) 32; JETP Lett. **5** (1976) 24 [hep-ex/0408100].
- [25] G. 't Hooft, Phys. Rev. Lett. **37** (1976) 8.
- [26] X. -G. He, H. Murayama, S. Pakvasa and G. Valencia, Phys. Rev. D **61** (2000) 071701 [hep-ph/9909562].
- [27] C. -H. Chen, Phys. Lett. B **521** (2001) 315 [hep-ph/0110098].
- [28] J. F. Donoghue and S. Pakvasa, Phys. Rev. Lett. **55** (1985) 162.
- [29] J. F. Donoghue, X. -G. He and S. Pakvasa, Phys. Rev. D **34** (1986) 833.
- [30] D. Chang, X. -G. He and S. Pakvasa, Phys. Rev. Lett. **74** (1995) 3927 [hep-ph/9412254].
- [31] S. Weinberg, Phys. Rev. Lett. **37** (1976) 657.
- [32] H. H. Gutbrod, K. D. Gross, W. F. Henning and V. Metag (eds.), "An international accelerator facility for beams of ions and anti-protons. Conceptual design report" (FAIR CDR), GSI Darmstadt (2001), <http://www-alt.gsi.de/documents2/FOLDER-1080636714.html>
- [33] W. Barth, "The Injector Systems of the FAIR Project", Presented at LINAC08, XXIV Linear Accelerator Conference, Victoria, BC, Canada, Sept 29-Oct 03, 2008, <http://accelconf.web.cern.ch/AccelConf/LINAC08/papers/mo204.pdf>
- [34] The PANDA Collaboration. "Technical Design Report, FAIR Antiproton Target and Separator", FAIR/GSI (2008) <http://www-win.gsi.de/FAIR-EOI/information.htm>
- [35] H. Stockhorst *et al.*, COOL2007-MOA1C02.
- [36] The PANDA Collaboration. "FAIR Baseline Technical Design Report", FAIR/GSI (2006) <http://www.gsi.de/documents/DOC-2006-Jul-40-1.pdf>
- [37] M. F. M. Lutz *et al.* [PANDA Collaboration], "Physics Performance Report for PANDA: Strong Interaction Studies with Antiprotons," arXiv:0903.3905 [hep-ex].

- [38] W. Erni *et al.* [PANDA Collaboration], “Technical Design Report for the PANDA Solenoid and Dipole Spectrometer Magnets,” arXiv:0907.0169 [physics.ins-det].
- [39] C. Ekstrom *et al.* [WASA Collaboration], Nucl. Instrum. Meth. A **371** (1996) 572.
- [40] Chr. Bergholz *et al.* [CELSIUS/WASA Collaboration], Nucl. Instrum. Meth. A **594** (2008) 339.
- [41] H. -H. Adam *et al.* [WASA-at-COSY Collaboration], nucl-ex/0411038.
- [42] Ö. Nordhage, PhD-Thesis, Uppsala Universitet, Sweden (2006)
- [43] A. V. Boukharov *et al.*, Phys. Rev. Lett. **100** (2008) 174505 [arXiv:0804.1782 [physics.flu-dyn]].
- [44] A. Khoukaz, PoS STORI **11** (2011) 036.
- [45] The PANDA Collaboration. “Technical Design Report for the: PANDA Micro Vertex Detector,” arXiv:1207.6581 [physics.ins-det].
- [46] The PANDA Collaboration. “Technical Design Report for the: PANDA Straw Tube Tracker,” arXiv:1205.5441 [physics.ins-det].
- [47] H. Staengle *et al.*, Nucl. Instrum. Meth. A **397** (1997) 261.
- [48] Technical Proposal, CERN/LHC 9.71.
- [49] Technical Proposal, 1994 CERN/LHCC 94-38, LHCC/P1
- [50] K. Mengel *et al.*, IEEE Trans. Nucl. Sci. **45** (1998) 681.
- [51] R. Novotny *et al.*, IEEE Trans. Nucl. Sci. **47** (2000) 1499 [Radiat. Meas. **33** (2001) 615].
- [52] M. Hoek *et al.*, Nucl. Instrum. Meth. A **486** (2002) 136.
- [53] The PANDA Collaboration. “Technical Design Report for PANDA Electromagnetic Calorimeter (EMC),” arXiv:0810.1216 [physics.ins-det].
- [54] N. Akopov *et al.*, Nucl. Instrum. Meth. A **479** (2002) 511 [physics/0104033].
- [55] G. S. Atoian *et al.*, Nucl. Instrum. Meth. A **531** (2004) 467 [physics/0310047].
- [56] J. J. Sakurai, “Modern quantum mechanics”, (Addison-Wesley Publishing Company, USA, 1994)
- [57] H. Pilkuhn, “The interaction of hadrons”, (North-Holland Publishing Company, Amsterdam, 1967)
- [58] M. G. Doncel *et al.*, Phys. Rev. D **7** (1973) 815.

- [59] M. G. Doncel, L. Michel and P. Minnaert, Nucl. Phys. B **38** (1972) 477.
- [60] W. Koch, in: “Analysis of scattering and decay”, ed. M. Nikolic (Gordon and Breach, New York-London-Paris, 1968), p. 231
- [61] K. -B. Luk, FERMILAB-THESIS-1983-16.
- [62] K. Paschke, PhD-Thesis, Carnegie Mellon University, USA (2001)
- [63] X. Artru, M. Elchikh, J. -M. Richard, J. Soffer and O. V. Teryaev, Phys. Rept. **470** (2009) 1 [arXiv:0802.0164 [hep-ph]].
- [64] B. Holzenkamp, K. Holinde and J. Speth, Nucl. Phys. A **500** (1989) 485.
- [65] J. Haidenbauer, K. Holinde and J. Speth, Nucl. Phys. A **562** (1993) 317.
- [66] K. Paschke and B. Quinn, Phys. Lett. B **495** (2000) 49 [hep-ex/0008008].
- [67] J. -M. Richard, Phys. Lett. B **369** (1996) 358 [nucl-th/9601015].
- [68] M. Elchikh and J. -M. Richard, Phys. Rev. C **61** (2000) 035205 [hep-ph/9905400].
- [69] J. -M. Richard and X. Artru, Nucl. Instrum. Meth. B **214** (2004) 171 [nucl-th/0304015].
- [70] X. Artru and J. -M. Richard, Phys. Part. Nucl. **35** (2004) S126 [hep-ph/0401234].
- [71] C. Cohen-Tannoudji, B. Diu and F. Laloë, “Quantum mechanics volume 1”, (Wiley and sons, New York, 1977)
- [72] N. Hamann *et al.* [CP-Hyperon Study Group Collaboration], CERN Geneva - CERN-SPSLC-92-19 (92/03,rec.Apr.) 48 p.
- [73] J. F. Donoghue, B. R. Holstein and G. Valencia, Phys. Lett. B **178** (1986) 319.
- [74] L. -L. Chau and H. -Y. Cheng, Phys. Lett. B **131** (1983) 202.
- [75] P. D. Barnes *et al.*, Phys. Rev. C **54** (1996) 1877.
- [76] H. Becker *et al.* [CERN-Munich Collaboration], Nucl. Phys. B **141** (1978) 48.
- [77] V. Flaminio, W. G. Moorhead, D. R. O. Morrison and N. Rivoire, CERN-HERA-84-01
- [78] T. Johansson, “Antihyperon-hyperon production in antiproton-proton collisions”, in *AIP Conf. Proc. Eight Int. Conf. on Low Energy Antiproton Physics*, page 95, 2003.
- [79] B. Musgrave and G. Petmezas, Nuovo Cim. **35** (1965) 735.
- [80] C. Baltay *et al.*, Phys. Rev. B **140** (1965) 1027.

- [81] F. Tabakin and R. A. Eisenstein, Phys. Rev. C **31** (1985) 1857.
- [82] M. Kohno and W. Weise, Phys. Lett. B **179** (1986) 15.
- [83] P. La France, B. Loiseau and R. Vinh Mau, Phys. Lett. B **214** (1988) 317.
- [84] R. G. E. Timmermans, T. A. Rijken and J. J. de Swart, Phys. Rev. D **45** (1992) 2288.
- [85] J. Haidenbauer, K. Holinde and J. Speth, Phys. Rev. C **46** (1992) 2516.
- [86] H. R. Rubinstein and H. Snellman, Phys. Lett. B **165** (1985) 187.
- [87] S. Furui and A. Faessler, Nucl. Phys. A **468** (1987) 669.
- [88] M. Burkardt and M. Dillig, Phys. Rev. C **37** (1988) 1362.
- [89] M. A. Alberg, E. M. Henley and L. Wilets, Z. Phys. A **331** (1988) 207.
- [90] E. Klempt, F. Bradamante, A. Martin and J. M. Richard, Phys. Rept. **368** (2002) 119.
- [91] F. Tabakin, R. A. Eisenstein and Y. Lu, Phys. Rev. C **44** (1991) 1749.
- [92] M. A. Alberg, J. R. Ellis and D. Kharzeev, Phys. Lett. B **356** (1995) 113 [hep-ph/9503333].
- [93] B. Bassaleck *et al.*, Pys. Rev. Lett. **89** (2002) 212302
- [94] S. Grape, PhD-Thesis, Uppsala Universitet, Sweden (2009)
- [95] W. M. Yao *et al.* [Particle Data Group Collaboration], J. Phys. G G **33** (2006) 1.
- [96] J. Haidenbauer, K. Holinde and J. Speth, Phys. Rev. C **47** (1993) 2982.
- [97] P. Kroll and W. Schweiger, Nucl. Phys. A **474** (1987) 608.
- [98] P. Kroll, B. Quadder and W. Schweiger, Nucl. Phys. B **316** (1989) 373.
- [99] H. Genz, M. Nowakowski and D. Woitschitzky, Phys. Lett. B **260** (1991) 179.
- [100] S. Okubo, Phys. Lett. **5** (1963) 165.
- [101] G. Zweig, CERN report TH-401.
- [102] J. Iizuka, Prog. Theor. Phys. Suppl. **37** (1966) 21.
- [103] T. Kunihiro and T. Hatsuda, Phys. Lett. B **240** (1990) 209.
- [104] A. B. Kaidalov and P. E. Volkovitsky, Z. Phys. C **63** (1994) 517.
- [105] A. I. Titov and B. Kampfer, Phys. Rev. C **78** (2008) 025201 [arXiv:0807.1822 [hep-ph]].

- [106] A. T. Goritschnig, P. Kroll and W. Schweiger, Eur. Phys. J. A **42** (2009) 43 [arXiv:0905.2561 [hep-ph]].
- [107] J. He, Z. Ouyang, X. Liu and X. -Q. Li, Phys. Rev. D **84** (2011) 114010 [arXiv:1109.5566 [hep-ph]].
- [108] A. Khodjamirian, C. Klein, T. Mannel and Y. M. Wang, Eur. Phys. J. A **48** (2012) 31 [arXiv:1111.3798 [hep-ph]].
- [109] J. Tandean and G. Valencia, Phys. Rev. D **67** (2003) 056001 [hep-ph/0211165].
- [110] S. W. Lin *et al.* [Belle Collaboration], Nature **452** (2008) 332.
- [111] P. D. Barnes *et al.*, Phys. Lett. B **199** (1987) 147.
- [112] K. B. Luk *et al.* [E756 Collaboration], Phys. Rev. Lett. **85** (2000) 4860 [hep-ex/0007030].
- [113] T. Holmstrom *et al.* [HyperCP Collaboration], Phys. Rev. Lett. **93** (2004) 262001 [hep-ex/0412038].
- [114] C. Materniak [HyperCP Collaboration], Nucl. Phys. Proc. Suppl. **187** (2009) 208.
- [115] A. Frodesen, O. Skjeggstad, and H. Tofte, “Probability and statistics in particle physics”, (Universitetsforlaget, Bergen, 1979)
- [116] R. L. Tayloe, PhD-Thesis, University of Illinois, USA (1995)
- [117] D. J. Lange, Nucl. Instrum. Meth. A **462** (2001) 152.
- [118] J. Allison *et al.*, IEEE Trans. Nucl. Sci. **53** (2006) 270.
- [119] S. Agostinelli *et al.* [GEANT4 Collaboration], Nucl. Instrum. Meth. A **506** (2003) 250.
- [120] D. Brown, E. Charles, and D. Roberts, The BaBar track finding algorithm, Proc. Computing in High Energy Physics Conference, Padova, 2000.
- [121] F. James and M. Roos, Comput. Phys. Commun. **10** (1975) 343.
- [122] B. Aubert *et al.* [BABAR Collaboration], Nucl. Instrum. Meth. A **479** (2002) 1 [hep-ex/0105044].
- [123] R. Jacobsen, Beta: A High Level Toolkit for BaBar Physics Analysis, 1997, presented at Conference on Computing in High Energy Physics, Berlin.
- [124] R. Brun and F. Rademakers, Phys. Res. A **389**, 81 (1996 1997).
- [125] FairRoot, Simulation and Analysis Framework, <http://fairroot.gsi.de>.
- [126] Virtual Monte Carlo, <http://root.cern.ch/root/vmc>.

- [127] CERN Program Library W5013 (1991).
- [128] FLUKA, <http://www.fluka.org>.
- [129] P. Yepes, Nucl. Instr. and Meth. **A380**, 582 (1996).
- [130] R. Frühwirth, A. Strandlie, and W. Waltenberger, Nucl. Instr. and Meth. in Phys. Res. **A490**, 366 (2002).
- [131] Rho: A Set of Analysis Tools for ROOT,
<http://savannah.fzk.de/websites/hep/rho>.
- [132] Belle Kinematic Fitter,
<http://hep.phys.s.u-tokyo.ac.jp/jtanaka/BelleSoft/KFitter>.
- [133] B. R. French, J. Moebes and C. Pols, Nucl. Phys. B **119** (1977) 237.
- [134] A. I. Titov and B. Kampfer, arXiv:1105.3847 [hep-ph].
- [135] A. Chakrabarti, Il Nuovo Cimento **43A** (1966) 3.
- [136] V. Bargmann, L. Michel and V. L. Telegdi, Phys. Rev. Lett. **2** (1959) 435.

Acta Universitatis Upsaliensis

Uppsala Dissertations from the Faculty of Science

Editor: The Dean of the Faculty of Science

1–11: 1970–1975

12. *Lars Thofelt*: Studies on leaf temperature recorded by direct measurement and by thermography. 1975.
13. *Monica Henriksson*: Nutritional studies on *Chara globularis* Thuill., *Chara zeylanica* Willd., and *Chara haitensis* Turpin. 1976.
14. *Göran Kloow*: Studies on Regenerated Cellulose by the Fluorescence Depolarization Technique. 1976.
15. *Carl-Magnus Backman*: A High Pressure Study of the Photolytic Decomposition of Azothane and Propionyl Peroxide. 1976.
16. *Lennart Källströmer*: The significance of biotin and certain monosaccharides for the growth of *Aspergillus niger* on rhamnose medium at elevated temperature. 1977.
17. *Staffan Renlund*: Identification of Oxytocin and Vasopressin in the Bovine Adenohypophysis. 1978.
18. *Bengt Finnström*: Effects of pH, Ionic Strength and Light Intensity on the Flash Photolysis of L-tryptophan. 1978.
19. *Thomas C. Amu*: Diffusion in Dilute Solutions: An Experimental Study with Special Reference to the Effect of Size and Shape of Solute and Solvent Molecules. 1978.
20. *Lars Tegnér*: A Flash Photolysis Study of the Thermal Cis-Trans Isomerization of Some Aromatic Schiff Bases in Solution. 1979.
21. *Stig Tormod*: A High-Speed Stopped Flow Laser Light Scattering Apparatus and its Application in a Study of Conformational Changes in Bovine Serum Albumin. 1985.
22. *Björn Varnevig*: Coulomb Excitation of Rotational Nuclei. 1987.
23. *Frans Lettenström*: A study of nuclear effects in deep inelastic muon scattering. 1988.
24. *Göran Ericsson*: Production of Heavy Hypernuclei in Antiproton Annihilation. Study of their decay in the fission channel. 1988.
25. *Fang Peng*: The Geopotential: Modelling Techniques and Physical Implications with Case Studies in the South and East China Sea and Fennoscandia. 1989.
26. *Md. Anwar Hossain*: Seismic Refraction Studies in the Baltic Shield along the Fennolora Profile. 1989.
27. *Lars Erik Svensson*: Coulomb Excitation of Vibrational Nuclei. 1989.
28. *Bengt Carlsson*: Digital differentiating filters and model based fault detection. 1989.
29. *Alexander Edgar Kavka*: Coulomb Excitation. Analytical Methods and Experimental Results on even Selenium Nuclei. 1989.
30. *Christopher Juhlin*: Seismic Attenuation, Shear Wave Anisotropy and Some Aspects of Fracturing in the Crystalline Rock of the Siljan Ring Area, Central Sweden. 1990.
31. *Torbjörn Wigren*: Recursive Identification Based on the Nonlinear Wiener Model. 1990.
32. *Kjell Janson*: Experimental investigations of the proton and deuteron structure functions. 1991.
33. *Suzanne W. Harris*: Positive Muons in Crystalline and Amorphous Solids. 1991.
34. *Jan Blomgren*: Experimental Studies of Giant Resonances in Medium-Weight Spherical Nuclei. 1991.
35. *Jonas Lindgren*: Waveform Inversion of Seismic Reflection Data through Local Optimisation Methods. 1992.
36. *Liqi Fang*: Dynamic Light Scattering from Polymer Gels and Semidilute Solutions. 1992.
37. *Raymond Munier*: Segmentation, Fragmentation and Jostling of the Baltic Shield with Time. 1993.

